Particle-Based Modeling of Ni-YSZ Anodes

Thesis by

Vaughan L. Thomas

In Partial Fulfillment of the Requirements

for the Degree of

Doctor of Philosophy

California Institute of Technology

Pasadena, California

2012

(Defended January 10, 2012)

Contents

List of Figures

List of Tables

Nomenclature

$\dot{s}_k$ Molar production rate per unit area, $\text{mol} \cdot \text{m}^{-2} \cdot \text{s}^{-1}$

l^k_{TPB} TPB length between a cermet particle and the kth neighboring particle of a different conduction type, m

$< R^2 >$ Average of the square of particle displacement, m^2

$\bar{\mathbf{r}}$ Normal vector to a surface

$\dot{\omega}_{\text{e}^-}$ Net rate of production of electrons at the TPB per unit length, $\text{mol} \cdot \text{s}^{-1} \cdot \text{m}^{-1}$

η Overpotential, volts

η_{i} Overpotential, associated with element i of a fuel cell, volts

γ_{TPB} Three-phase boundary length per volume, $\text{m} \cdot \text{m}^{-3}$

κ Conductivity, $\text{siemens} \cdot \text{m}^{-1}$

κ_{i} Bulk conductivity of the particles of type i, $\text{siemens} \cdot \text{m}^{-1}$

κ_{p} Specific electrocatalytic activity, $\text{siemens} \cdot \text{m}^{-1}$

ϵ_{I} Coverage-dependant activation energy for species I, $\text{kJ} \cdot \text{kmol}^{-1}$

E   Electric field

$\mathcal{D}^e_{k,\mathrm{Kn}}$ Effective Knudsen diffusivity of species k, $\mathrm{m}^2 \cdot \mathrm{s}^{-1}$

$\mathcal{D}_{\mathrm{Kn}}$ Knudsen diffusivity, $\mathrm{m}^2 \cdot \mathrm{s}^{-1}$

Kn   Knudsen number

μ Viscosity, $\mathrm{kg} \cdot \mathrm{m}^{-1} \cdot \mathrm{s}^{-1}$

ϕ Porosity

Φ_i Potential distribution in phase i, volts

Φ_k Electrical potential of the kth neighboring particle of same conduction type, volts

ϕ_i Potential in cluster of type i participating in a type I interface, volts

ρ^e Resistivity, ohms $\cdot$ m^{-1}

ρ^e_i Resistivity in phase i, ohms $\cdot$ m^{-1}

σ Conductivity, siemens

τ Tortuosity

θ Surface coverage

ξ Angluar displacement, radians

A Area, m^2

A^s Surface area, m^2

A_i^s Surface area of phase i, mm^2

b Permeability

C_k Concentration of species k, mol $\cdot$ m^{-3}

D Diffusivity, m$^2 \cdot$ s^{-1}

d Distance between particles in a packing particle ensemble, m

D^e Effective diffusivity, m$^2 \cdot$ s^{-1}

D_{kj}^e Effective Binary diffusion coefficient between species k and j

dS Differential length along a one-dimensional curve

ds Differential length along a one-dimensional curve

E Electric potential, volts

E_{A} Activation energy, kJ $\cdot$ kmol^{-1}

F Faraday's constant, coulombs $\cdot$ mol^{-1}

G Gibbs free energy, joules

H Enthalpy, joules

I Current, amperes

i Current, amperes

i_{F_e} Faradaic current across an electronically cermet particle, amperes

$i_{\mathrm{F}i}$ Faradaic current across an ionically conducting cermet particle, amperes

i_{F} Faradaic current across a cermet particle, amperes

i_{R} Resistive current across a cermet particle, amperes

i_{net} Net Current across a cermet particle, amperes

j Charge flux, amperes $\cdot$ m^{-2}

J_j fraction of species j

j_i Flux of the ith charged carrier, amperes $\cdot$ m^{-2}

k_B Boltzmann constant, joules $\cdot$ kelvin^{-1}

L Length of a cubic domain, m

L_i Length in the i dimension of a box domain, m

n_c Number of electrons participating in a chemical reaction

n_i Number of particles of type i in a particle ensemble

N_s Number of intersecting particles of the same conduction type

n_i Number density of the ith charged carrier, $\#\cdot$ m^3

N_{TPB} Number of intersecting particles of a different conduction type

p Pressure

P_c Fraction of percolating particles in a particle ensemble

p_c Critical limit for percolation probability

Pp Percolation probability

Q Charge, coulombs

q Charge density, coulombs $\cdot$ m^3

R Resistance, ohms

r Particle radius, m

R_k Resistance between a particle and the kth neighboring particle of the same conduction type, ohms

R_u Universal Gas Constant

r_{pore} Mean pore radius

S Entropy, joules $\cdot$ kelvin^{-1}

S Length along a one-dimensional curve

s Length along a one-dimensional curve

T Temperature, kelvin

t Time, s

t_d Diffusion time, s

u_i Velocity of the ith charged carrier, m $\cdot$ s^{-1}

V Voltage, volts

W_k Molecular weight of species k

X_j Mole fraction of species j

Z Overall average coordination number

Z_e Average coordination number for electronically conducting particles

Z_i Average coordination number for ionically conducting particles

Z_x Average coordination number for particles of type x

Z_{e-e} Average coordination of electronically conducting particles with other electronically conducting particles

Z_{i-i} Average coordination of ionically conducting particles with other ionically conducting particles

z_i Charge of the ith charged carrier, coloumbs

Z_{x-x} Average coordination of particles of type x with respect to other particles of type x

Abstract

In this work we examine the performance of particle-based models with respect to the
Ni-YSZ composite anode system. The conductivity and triple-phase boundary (tpb)
of particle-based systems is estimated. The systems considered have mono-dispersed
particle size distributions, bi-modal particle size distributions with a YSZ:Ni particle size
ratio of 1:0.781, and particle size distributions based on experimental measurements. All
three types of systems show qualitative behavioral agreement in terms of conductivity,
with clear transition from non-conducting behavior to high conducting behavior over a
small transition regime which varied from a nickel phase fraction of .22-.28 for the mono-
dispersed cases, 0.19-.0.25 for the bimodal cases, and 0.19-0.30 for the experimentally
based cases. Mono-dispersed and simple-polydispersed particle size distribution show
very low variation from case to case, with $\sigma/\mu \leq 0.04$. Cases based on empirical particle
size distribution data demonstrated significantly higher variances which varied over a
very large range, $0.3 \leq \sigma/\mu \leq 1.1$. With respect to the calculations of the TPB length,
we find that the same pattern of variance in the measure of the triple-phase boundary
length. The TPB length for the mono-dispersed and simple poly-dispersed systems was
in the range of 3×10^{12}–4×10^{13} m/m^3. For empirical particle size distribution data the
TPB length density was in the range of 8×10^9–2×10^{11} m/m^3. The variance of the TPB
length density follows the same pattern as the conductivity measurements with very
low variance for the mono-dispersed and simple poly-dispersed systems and much larger
variance for the empirically-based systems. We also examine the association between the
TPB length and the availability of conducting pathways for the participating particles

of individual TPBs. The probability of a TPB having a conducting pathway in the gas phase is essentially 100% in all cases. The probability of an individual tpb section having conducting pathways in either of the solid phases is directly related to percolation condition of that phase.

We also considered a particle-based composite electrode realization based on a three-dimensional reconstruction of an actual Ni-YSZ composite electrode. For this model we used particles which vary in nominal size from 85–465 nm, with size increments of 42.5 nm. We paid particular attention to the coordination numbers between particles and the distribution of particle size interconnections. We found that homogeneous inter-particle connections were far more common than would occur using a random distribution of particles. In particular we found that for a random collection of particles of similar composition the likelihood Ni-Ni particle connections was between 0.18–0.30. For the reconstruction we found the likelihood of Ni-Ni particle connections to be greater than 0.56 in all cases. Similarly, the distribution of connections between particles, with respect to particle size of the participating particles, deviated from what would be expected using a random distribution of particles. Particles in the range of 85–169 nm showed the highest coordination with particles of the same size. Particles in the range of 211–338 nm have the highest coordination with particles of radius 169 nm with very similar distributions. Particles with radius greater than 338 nm represented only 7.2×10^{-3} % of the particles within the reconstruction, and showed the highest coordination with particles of radius of 211 nm, but the distributions vary widely.

In the final chapter, we build a model which can account for mass transfer, heterogeneous chemistry, surface chemistry, and electrochemistry within a porous electrode. The electric potential is calculated on a particle basis using a network model; gas phase concentrations and surface coverages are calculated with a one-dimensional porous media model. Properties of the porous media are calculated via a TPMC method. TPB electrochemistry is calculated at individual triple phase boundaries within the particle

xxiii

model, based on local gas phase concentrations, surface coverages and particle potentials, and then added to the porous media model. Using this tool we are able to calculate the spatial distribution of the Faradaic current within the electrode, and variation in gas phase concentrations within the porous media.

Acknowledgements

I'd like to thank my advisors Professor David G. Goodwin and Professor Joseph E. Shepherd for all their guidance support. Professor Goodwin brought me to Caltech and launched me into my journey at Caltech. Professor Shepherd has given me invaluable guidance, but also tremendous personal support without which this work could not have completed.

Thanks to the Office of Naval Research for funding the greater part of my work at Caltech.

I'd also like to thank Professor Robert Kee, Huayang Zhu, Jay Sandal and Graham Golden for providing illuminating discussions and important suggestions that went into thesis.

I am forever indebted to Professor Gregory Jackson both for starting me on this path and for being instrumental in my coming to Caltech.

I've been lucky to work with a great number of unforgettable group mates including David Boyd, Francesco Ciucci, Moh El-Naggar, Hoa Yong, Jeff Hanna, Eugene Mahmoud, Phillip Boechtter, Rmy Mevel, Stephanie Coronel, Jason Damazo, Nicholas Parziale, and Joe Jewell. All of these people not only gave me support and help, but also laughter and fun.

My dear friends in the Caltech community Dennice Gayme, Roseanna Zia, Richard

Burnes, Mihai Florian, and Daniel Pragel made life at Caltech wonderful, David Lo-effeholz, John Morton-Aslanis, Roy Araki, Brigitte Forrey, and John Mendoza have enriched my life outside of Caltech.

Id like to thank my committee members Professors Joseph Shepherd, Sossina Haile, Melany Hunt and Kaushik Bhattacharya for their comments and encouragement. This work was supported by the Office of Naval Research (ONR).

A very special thank you to Claire Levaillant for your unwavering belief, support, and most of all love, without which I would not have finished.

Finally a special thanks to my family. My father, mother and brothers for all of your spiritual and material support through this journey. Your encouragement and support were invaluable to me. Also to the entire Thomas El family for sharing this moment with me.

Chapter 1

Introduction

1.1 Background

The world is currently at the precipice of major shifts in the way we generate and consume energy. Fossil fuels have dominated the energy infrastructure of the world for the past century. This dominance is due mainly to their low cost and high abundance relative to other forms of energy production. As our scientific knowledge of the environment has burgeoned over the same period, a number of issues have come to the fore relating to the use of fossil fuel energy. The consumption of fossil fuels releases large amounts of CO_2 into the atmosphere each year. Recent scientific advances warn of the deleterious impact of these CO_2 emissions on the environment in the form of global warming. In addition, much of the world's fossil fuel reserves are located in regions of world that are currently experiencing or are particularly vulnerable to social and political instability. The costs of crude oil are increasing rapidly due to the confluence of rapidly increasing demand from the former developing world and the flatlining of oil supplies as predicted by Hubbert's peak theory [27, 26].

Fuel cells are one of the solutions to the energy importation problem that are currently being explored. The fuel cell was first demonstrated by Sir William Robert Grove in

1839 [21]. Over the past 60 years interest in fuel cells has greatly increased. Current interest in fuel cells is largely driven by the fact that fuel cells are able to convert and generate electricity at higher efficiencies than combustion-based processes. Fuel cells are currently used or being tested in many everyday applications, such as stationary power, distributed power at the household level, aircraft APUs and transportation.

1.1.1   Fuel Cell Basics

A fuel cell converts chemical potential energy into useful electrical energy utilizing electrochemical reactions. A detailed explanation of the thermodynamics, chemical kinetics, and operation of fuel cells can be found in the *Fuel Cell Handbook* by Appleby and Foulkes [2]. What follows is a brief description of the basics of fuel cell operation. The reactions which form the basis of a fuel cell's operation typically involve a fuel molecule such as hydrogen, H_2, and an oxidizing agent such as oxygen, O_2. A fuel cell consists of a number of components:

1. The most important part of the fuel cell is the membrane electrode assembly (MEA). The MEA consists of:

   (a) The anode, an electrode which adsorbs fuel molecules, and in the case of more complex fuels allows complex fuels to be catalytically converted in to simpler fuels such as H_2 and CO_2.

   (b) The cathode, an electrode where oxidizing agents, usually O_2 as a component of an air-based flow stream, can be adsorbed and reduced.

   (c) The electrolyte, which transports ions between the anode and the cathode. The type and direction of ion transport is the main distinguishing element of different types of fuel cells.

2. The fuel channel delivers fuel to the anode.

3. The oxidizer channel delivers oxidizer to the cathode.

4. The current collector transports electrons produced by reactions within the MEA.

5. The load extracts useful work from the electrons produced by reactions within the MEA.

The basis for operation of a fuel cell is the same as for all chemically-based energy systems. Chemical reactions between reactant species result in product species. The product species mix has a lower chemical potential than the reactant species mix. That difference is energy, which is released by the reactions. Part of the released energy can then be converted into useful work. A major aspect of chemical reactions is the exchange and/or sharing of electrons. The major difference between fuel cells and combustion systems is that in a fuel cell some of these electron exchanges are mediated by the electrolyte and the load circuit. In a combustion system reactions are initiated by molecular collisions, and all electron exchange occurs directly between interacting molecules. Chemical reactions result in electrons moving from higher energy states to lower energy states and releasing energy to the environment in the process. In combustion, for example, electrons lose energy by exciting molecular motion (translation and vibration) and increasing the gas temperature. The thermal energy is removed by doing mechanical work in the case of an internal combustion engine or a gas turbine, or heat transfer in the case of a stationary power plant. The key difference between combustion and the operation of a fuel cell, is that the energy is extracted by directly utilizing the electrons from the chemical reactions. This is, potentially, a more thermodynamically efficient process than thermal engines.

Fuel cells are denoted by the type of electrolyte used. The commonly referenced types of fuel cells are referenced below:

1. **PEM** uses a polysulfonic polymer. H^+ ions are conducted by the membrane when the membrane has the requisite humidity.

2. **Phosphoric acid fuel cells** use an acidic liquid medium of phosphoric acid as a conduction path for hydrogen ions from the anode to the cathode.

3. **Alkaline fuel cells** use a basic liquid medium of phosphoric acid as a conduction path for hydrogen ions between the anode and the cathode.

4. **Molten carbonate fuel cells** operate at extremely high temperatures using the CO_3^- ions in molten carbonate as a conduction path for oxygen ions from the cathode to the anode.

5. **Solid oxide fuel cells (SOFC)** use an electrolyte consisting of an ion-conducting oxide which, at sufficiently high operating temperatures, allows the transport of oxygen ions from the cathode to the anode.

SOFCs are the highest efficiency type of fuel cells, and can achieve thermodynamic efficiencies which exceed that of other widely used heat engines, such as gas turbines and internal combustion engines. In addition high-efficiency complex thermodynamic cycles can be designed around SOFCs because of the high temperature of the waste heat ejected from the cell. For this reason SOFCs are being tried in a variety of applications, ranging from large-scale stationary power plants down to portable power supplies. The SOFC is the system of interest to this work. There are a variety of oxides which can be used within a SOFC. The ideal electrolyte has very high (oxygen) ion conductivity, which reduces the potential loss due to resistance of the electrolyte. Additionally, the ideal electrolyte has very low electron conductivity. Electrons which transfer from the anode to the cathode directly through the electrolyte do not produce useful work, and thus this "crossover current" represents an irreversibility within the SOFC system, reducing thermodynamic efficiency. One of the most common oxides used as an electrolyte for SOFCs is ZrO_2.

In the case of SOFC using a H_2 as a fuel and O_2 as an oxidizer, the process proceeds as follows (see Figure 1.1):

1. Oxygen, O_2, is adsorbed and reduced at the interface of the cathode and the electrolyte.

$$4 \text{ e}^- + O_2 \Longleftrightarrow 2 \text{ O}^{2-}(\text{s}) \tag{1.1}$$

2. Oxygen ions, O^-, are transported through the electrolyte to the triple-phase boundary (TPB). The TPB is the interface between the anode, the electrolyte, and the fuel stream.

3. At the interface of the fuel stream and the anode, hydrogen molecules, H_2, are adsorbed onto the surface of the Ni.

$$H_2 + 2 \text{ Ni(s)} \Rightarrow 2 \text{ H(s)} \tag{1.2}$$

4. At the TPB, adsorbed species, including hydrogen and oxygen ions, undergo reactions which result in the formation of adsorbed water and electrons. The water molecules can be desorbed into the fuel stream, and the electrons can migrate to the current collector.

$$2H(s) + O^- \Longleftrightarrow H_2O + 2 \text{ e}^- \tag{1.3}$$
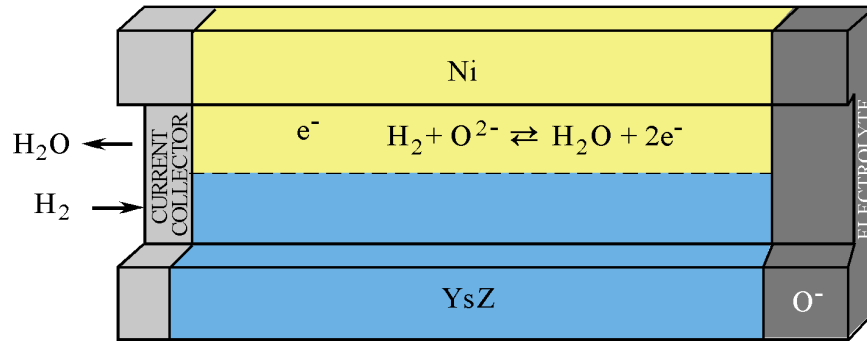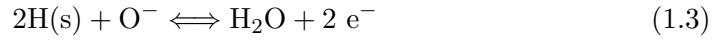
Figure 1.1: Basic operation of a SOFC

1.1.2 Energy Output from a Fuel Cell

In a chemically-based energy system, G, the free energy available from a chemical reaction can be calculated as:

$$\Delta G = G_{\text{out}} - G_{\text{in}} \tag{1.4}$$

$$= \Delta H - T\Delta S \ . \tag{1.5}$$

In the case of a fuel cell, this energy is extracted from the electrons transferred in the reaction process. An alternative way to measure the change in the free energy of the reaction is the electric potential of the reaction:

$$E = \frac{\Delta G}{n_c F} \ . \tag{1.6}$$

Fuel cell systems cannot achieve this ideal value of the electric potential during actual operations. A number of non-ideal or irreversible processes reduce the operating potential of any fuel cell below the theoretical thermodynamic limit. The loss of cell potential associated with these irreversible processes are overpotentials, designated by η. These overpotentials are designated by their origin within the fuel cell assembly. The following overpotentials are associated with the MEA:

1. η_{anode}

   Within the anode, the following phenomena contribute to η_{anode} and reduce cell potential:

   (a) The electrical contact resistance between the anode and the current collector.

   (b) The electrical resistance of the anode material to electrons traveling through the anode thickness.

   (c) Mass transport limitations of fuel moving through the anode to the TPB

interface.

(d) The kinetic limitations of electrochemical reactions at the TPB.

2. $\eta_{\text{electrolyte}}$

The main contributers to $\eta_{\text{electrolyte}}$ are:

(a) The resistance of the electrolyte material to ionic conduction.

(b) The electrical conductivity of the electrolyte material, which allows the direct transfer of electrons from the anode to the cathode in the form of a crossover current.

3. η_{cathode}

The following contribute to η_{cathode} and reduce cell potential:

(a) The electrical contact resistance between the anode and the fuel cell circuit.

(b) The ionic and electronic resistances of the cathode material to ions and electrons traveling through the cathode thickness.

(c) The kinetic limitations on reduction of the oxidizer within the cathode.

In actual fuel cell operation the electric potential is more accurately represented as:

$$E = \frac{\Delta G}{nF} - \eta_{\text{anode}} - \eta_{\text{electrolyte}} - \eta_{\text{cathode}} - \eta_{\text{other}} \ , \qquad (1.7)$$

where η_{other} represents overpotentials associated with other parts of the fuel cell besides the MEA, such as the contact resistances associated with the interconnect between the MEA and the current collectors.

A key to increasing the commercial viability and success of SOFCs is further improving their performance. The focus of this work is understanding the structure and operation of the anode of a SOFC, in particular Ni-YSZ composite anodes.

The anode of a SOFC is a complicated structure. The particular type of composite anodes considered in this work are combinations of ceramics and metals known as cermets. Various gas transport and chemical processes, as well as the flow of ionic and electronic current, all occur simultaneously in a complex three-dimensional structure. Taken individually, these processes are all known to some degree, but the interaction between them within the cermet and the design tradeoffs inherent in a given configuration are less well understood. An important avenue for reducing the cost of research into SOFC is the development of models which allow for a less expensive way to explore design optimization relative to experimental methods. To this end there have been a number of efforts to model the behavior of fuel cells. Of particular interest here are those models based on the random packing of particles within the cermet [1, 42, 43, 47]. These models have shown good agreement with experimental results in terms of cermet conductivity and polarization resistance [48]. Using these models it is possible to explore the overpotential associated with the porous anodes' resistance to both electronic and ionic current. These models, however, do not account for the overpotential due to resistance to mass transfer within the porous electrode. Models accounting for these effects have been published by Kee et al. [53] and Yong [24]. These models consider the mass transport through an "averaged" porous medium. In these models it is assumed that all charge transfer reactions occur at the electrode–electrolyte boundary, neglecting any overpotential due to current.

In this work we will examine the fundamental assumptions underlying these composite anode models. In doing so we will discover that the the existing models understate the complexity of the composite electrodes in ways that strongly impact the ability of such models to produce useful results across a wide range of geometrical configurations. In particular, we will show that a more realistic and necessarily more complex approach to the physical arrangement of phases within the composite electrodes is required in order to capture key information relating the electronic and ionic conductivity of various

phases.

1.2 Organization

In Chapter 2, a model for the calculating current and potential within a composite anodes will be presented. First, previous work by researchers on SOFC anode modeling will be reviewed. Particular attention will be paid to the Ni-YSZ system and to models which assume that the composite electrode can be represented by a discrete resistor network. These networks are used as a representation of ensembles containing either monodispersed or simple polydispersed particle distributions with two particle sizes, one for each material type. The basic principles and mathematics of these models will be explained, and the fundamental assumptions of these models will be clearly laid out. Then a new model will be presented considering non-uniform ensembles, including ensembles created with non-analytic distribution functions.

In Chapter 3 computational results from the model presented in Chapter 2 will be presented, and the relationship between the those results and the physical nature of composite anodes will be discussed relative to the underlying assumptions used to build the model.

In Chapter 4 the composition and structure of actual composite electrodes within SOFCs will be examined and compared to the structure of the particle ensembles used to model them. A method for generating particle ensembles based on the deconstruction of an actual SOFC composite anode will be presented in order to improve predictions of fuel cell performance.

In Chapter 5 the gas phase transport properties and the electrochemistry of anodes near the electrolyte boundary will be considered. The model presented in Chapter 1 will be combined with the transport and detailed chemistry model first presented by Yong and

Goodwin [24]. Gas transport properties will be calculated following the method put forward by Hanna [23]. This model will be used to demonstrate and calculate the impact of transport and kinetic limitations on the performance of composite anodes.

Chapter 2

Conductivity Modeling in Composite Anodes

In this chapter we will develop the numerical models that will be used in this work to evaluate the physical, electrical and, chemical properties of composite electrodes. The first section of this chapter will review previous research efforts using packed spheres to model percolation and electrical resistance in porous media. Particular emphasis will be paid to the use of these models in the study of SOFC anode performance. The second section of the chapter will present a summary of the relevant theory on percolation and solving resistor networks. In the third and final section of this chapter the resistor network model that will be used in subsequent chapters of this thesis will be presented, including the methodologies for creating arbitrary discrete distributions of particle sizes.

2.1 Background

Resistor networks have become a important method of investigating the properties of Ni-YSZ composite anodes. Whether regular arrays of resistor elements or random particle collections, resistor network models exhibit a percolation threshold: a concentration

level at which the network goes from essentially zero conductivity to high conductivity. The first research indicating that resistor networks could be useful in studying composite anodes was provided by Dees et al. [14] in 1987, nine years before the first resistor network model was applied to the problem of composite electrodes in SOFCs. In their experiments on Ni-YSZ composite electrodes there was a distinct threshold in terms of Ni concentration at which the conductivity of the Ni phase changed by several orders of magnitude. This threshold is clearly observable in Figure 2.1. This type of threshold
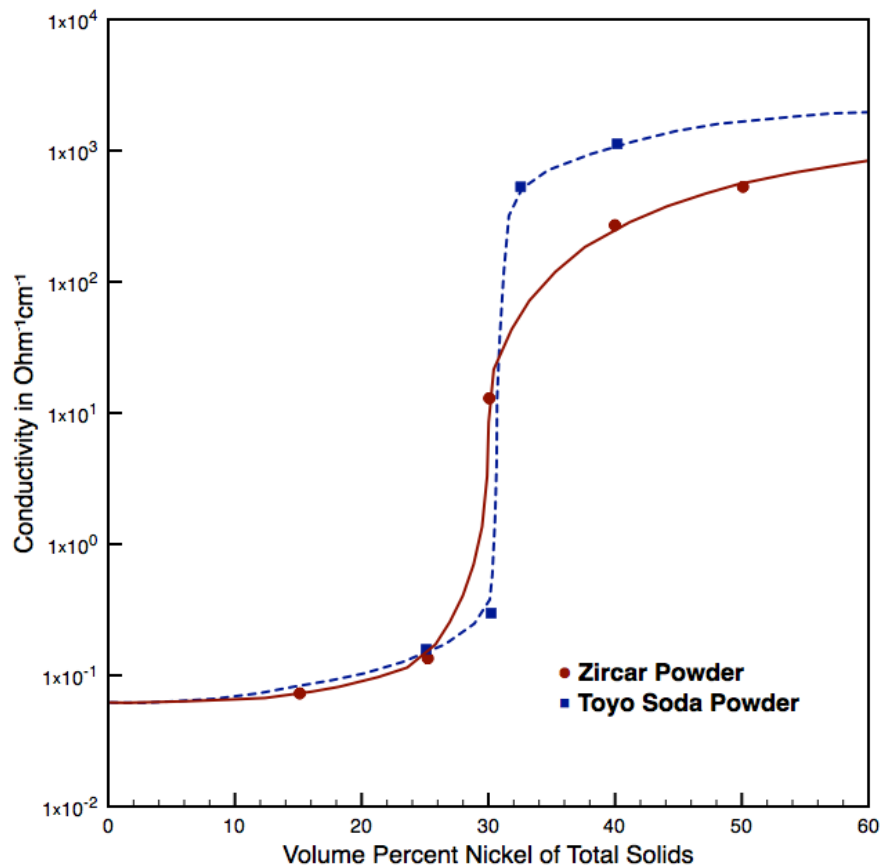
Figure 2.1: Percolation threshold of a Ni-YSZ composite anode as measured by Dees [14]

is a feature of the mathematical description of graphs [20]. A graph is defined as a set of connected objects, usually referred to as vertices. The connections between vertices

are referred to as edges.

In a graph the percolation threshold is determined by pattern of connections between vertices. In particular, the average number of connections between vertices correlates directly to the percolation threshold. In the field of powder metallurgy, interest in understanding the percolation of deforming metal matrix powders led to a number of efforts to simulate percolation in clusters of packed particles. Suzuki and Oshima developed methods for estimating the coordination numbers of sphere ensembles, including systems with up three different size particles [49, 50]. Bouvard and Oger independently developed relations between percolation and particle coordination in binary powder mixtures [8, 37].

The use of sphere-based resistor network models to construct a model of the anode of a SOFC was first pioneered by Svein Sunde in a series of papers published in 1995 and 1996 [45, 46, 47]. In these papers Sunde proposed a method of modeling composite electrodes as both a cubic lattice with nodes representing two distinct phases and as a collection of conducting spheres of two different phases, as illustrated in Figure 2.2. In the paper entitled, "Monte Carlo Simulations of Conductivity of Composite Electrodes for Solid Oxide Fuel Cells" [47], two approaches were used with very similar results. The cermet was modeled as a cubic lattice in which each point within the lattice corresponded to a either an electrode or electrolyte particle with the composition at each lattice point being determined randomly, with a weighting corresponding to the desired cermet composition. The second method was disordered packing of mono-sized particles of either type, using the packing algorithm of Bennett [6]. Using these two methods, Sunde calculated the conductivity of the electrode phase within the cermet to show agreement between the two methods for bimodal distributions of particles [48]. The simulation results gave good agreement with existing experimental values for the polarization resistance of composite anodes.

A number of researchers followed up the use of resistor network models to predict

14
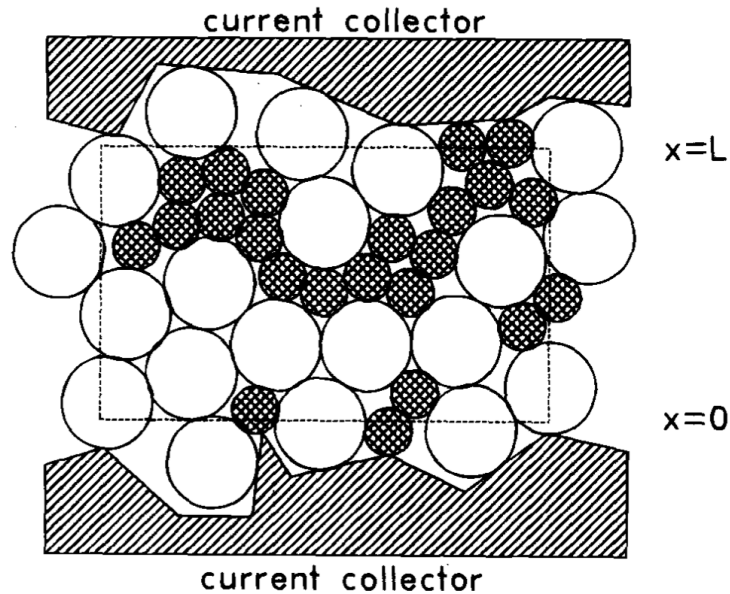
Figure 2.2: Illustration of composite particle structure from Sunde [46]. Reprinted by permission of the The Electrochemical Society.

the properties and performance of Ni-YSZ composite anodes. Costamanga et al. [13] demonstrated that for relatively thick composite anodes, the optimum performance was obtained when the phase concentration of the electronic conductor was slightly above the percolation threshold. Kwashima used models based on cubic lattices with randomized site placement, as shown in Figure 2.3. Using these methods he confirmed that the percolation threshold for Ni conduction in Ni-YSZ composites occurred at the expected solid volume fraction of 0.324. Dotelli and Mari published a series of papers exploring the use of randomized resistor networks to simulate electrical conductivity in crystalline structures including SOFC composite electrodes [32, 31, 16]. The methods used by Dotelli and Mari focused on generating a polycrystalline microstructure via Voronoi tessellation and creating a second insulating phase via a Monte-Carlo method. Using these methods, they were able to correlate conductivity performance in composite structure with grain size and structure. More recently, Schneider used the discrete element method, a computational sintering technique developed in the context
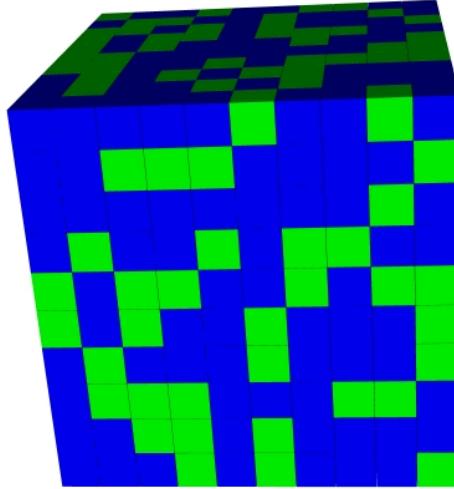
Figure 2.3: $10 \times 10 \times 10$ cubic lattice of the type used by Kawashima to model the percolation and conductivity performance of Ni-YSZ composites [30]

of powder metallurgy with Martin [34, 33], to explore composite anode performance. In the initial paper, the effect of functionally graded composite anodes was compared to composite anodes of uniform construction [43]. The next paper focused on optimizing electrode performance, returning results consistent with the earlier experimental work of Dees [14] and the computational work of Kawashima [30]: The optimium electrode electrochemical performance occurs when the volume fraction of electronically conducting particles just exceeds the percolation threshold [42]. In addition to the interest in SOFC anodes, Chan et al. investigated resistor network models to simulate SOFC cathode performance using a model which incorporated gas transport via diffusion and electrochemistry [10].

2.2   Theory

2.2.1   Percolation Theory

The conduction properties of heterogeneous collections of particles can be estimated analytically. The basis for this analysis is percolation theory. Percolation theory is based based largely on graph theory, and was first presented by Broadbent and Hammersley in 1957 [22]. Percolation theory describes the connectivity of clusters in a random graph. The percolation probability, p, is the fundamental property of interest, and represents the probability that a path exists from one edge vertex to an edge vertex on the opposite edge of a graph. A canonical problem addressed within percolation theory is calculation of the the critical limit or percolation threshold of lattices, p_c [20]. As an example a finite, two-dimensional graph with $P_p = .51$ is shown in Figure 2.4.

The application of this work to the conductivity of fuel cell electrodes has been accomplished by using Monte Carlo simulations in place of analytical results and considering modeling the electrode structure as a collection of overlapping spheres, which can then be further represented as a lattice [50]. The sphere centers can be considered vertices, and the conduction paths between particles can be represented as edges. When applied to the problem of particle-based fuel cell electrode models, this analysis can predict compositions under which electronic or ionic conduction can occur within the electrode structure. Understanding of the percolation threshold and calculation of the percolation probability allows for the calculation of the conductance of the lattice, whether that be the conductance of water flow through a series of pores, or the electrical conductance of an electrical circuit [20].
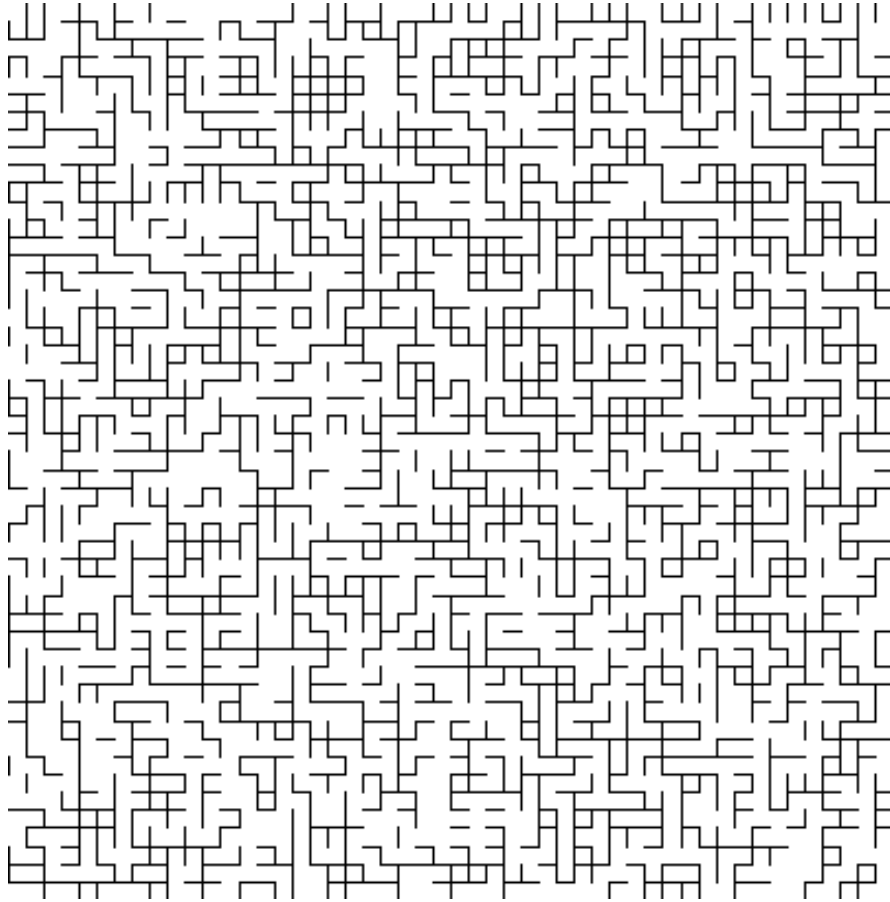
Figure 2.4: Finite two-dimensional graph with percolation probability = .51 from "Percolation". (With kind permission from [20])

2.2.2 Conductivity

2.2.2.1 Motivation

We can construct a simplified view of the operation of a SOFC composite anode by viewing the two phases of the composite anode as a resistive elements, with the Ni phase conducting only electrons and the YSZ phase conducting only positively charged oxygen ions. Both phases are in contact with the electrolyte boundary, the current collector and the gas phase. In this case the gas stream consists only of H_2 and H_2O. This simplified setup is illustrated in Figure 2.5. The governing equations of this anode
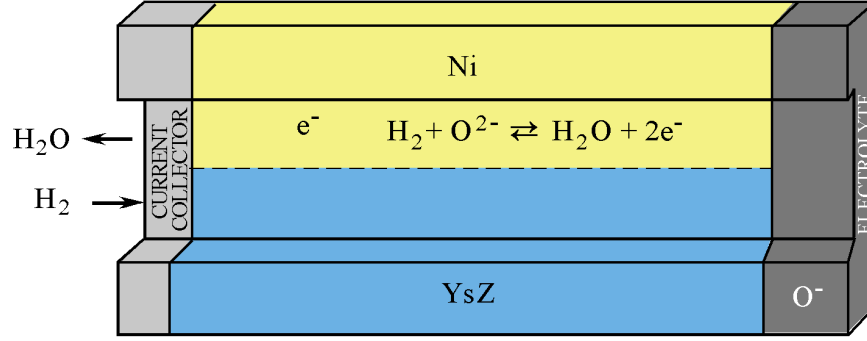
Figure 2.5: Basic operation of a SOFC

can be expressed as a one-dimensional system of PDEs. Sunde explored this particular system and developed the governing equations and appropriate boundary conditions with the assumption of linear kinetics on a finite one-dimensional domain on the interval $0 \leq x \leq L$ [47]:

$$i_{\mathrm{Ni}} = -\kappa_{\mathrm{Ni}} \frac{d\phi_{\mathrm{Ni}}}{dx} \tag{2.1}$$

$$i_{\mathrm{YSZ}} = -\kappa_{\mathrm{YSZ}} \frac{d\phi_{\mathrm{YSZ}}}{dx} \tag{2.2}$$

$$\frac{d\phi_{\mathrm{Ni}}}{dx} = \frac{d\phi_{\mathrm{YSZ}}}{dx} \tag{2.3}$$

$$\frac{di_{\mathrm{YSZ}}}{dx} = \gamma_{\mathrm{TPB}}\kappa_{\mathrm{p}}(\phi_{\mathrm{Ni}} - \phi_{\mathrm{YSZ}}) \tag{2.4}$$

$$i_{\mathrm{Ni}}(x = 0) = 0 \tag{2.5}$$

$$i_{\mathrm{YSZ}}(x = 0) = -I \tag{2.6}$$

$$\phi_{\mathrm{YSZ}}(x = 0) = 0 \tag{2.7}$$

$$i_{\mathrm{Ni}}(x = L) = 0 . \tag{2.8}$$

κ is proportional to the resistance, R, of the phase in these equations. The maximum current is generated when κ_{Ni} and κ_{YSZ} are minimized. As indicated in Section 2.1, the resistance of the anode phases plays an important role in the performance of the composite anode, and consequently the performance of the entire fuel cell system. For this reason, understanding the resistances of the phases in composite electrodes is an

important part of improving performance.

2.2.2.2   Calculating Potential

Percolation theory gives a useful description of the connectivity of an arbitrary network. However, in order to evaluate the overpotentials due to ohmic losses within a composite anode via simulation, we must calculate the actual potential and current throughout a network. Current resistance is described by Ohm's law: The voltage across a resistance is directly proportional to the current flowing through it. This can be expressed as an equation,

$$V = IR \ . \tag{2.9}$$

With respect to the electronic current, the simplest view of the anode is as a pair of resistors in parallel between the electrolyte boundary and the current collector. The resistance of each phase within the anode can then be described by the inherent resistivity of the anode material, ρ^e, and the length between the electrolyte boundary and the current collector. Unfortunately, this simple picture does not capture complexity of typical SOFC anode structure. As shown in Figure 2.7, the anode of a SOFC is a three-phase composite of electronically conducting material, ionically conducting material, and void space which can be penetrated by the fuel.

A simple sketch of the derivations will be presented here to introduce the topic of resistance computation. The basis for determining the equations governing potential distribution are based on two principles:

1. **Ohm's Law**

$$V = IR \tag{2.10}$$

   The voltage, V, can be restated as the difference in potential between the source

and the sink of the current:

$$V = \Phi_{\text{source}} - \Phi_{\text{sink}} , \tag{2.11}$$

where I, the current, is the flux of charge across a boundary per unit time.

$$I = \int_A \vec{j} \cdot dS , \tag{2.12}$$

where the flux of the ith type of charge carrier is defined,

$$\vec{j_i} = n_i z_i \vec{u_i} , \tag{2.13}$$

where n_i is the number density of the charge carriers, z_i is the charge of the charge carriers, and u_i is the velocity. The total flux, $\vec{j}$, is the sum of the fluxes of all charge carriers,

$$\vec{j} = \sum_{i=0}^{N} \vec{j_i} . \tag{2.14}$$

R, the resistance, can be defined in terms of the resistivity, ρ^e,

$$R = \rho^e \frac{\Delta x}{A} . \tag{2.15}$$

2. **Conservation of Charge**

The conservation of charge precludes the generation or destruction of isolated charge, whether positive or negative. Positive and negative charges can only be generated or destroyed in balanced sets. For a single uniform region, or a single point,

$$\frac{\Delta Q}{\Delta t} = I_{\text{in}} - I_{\text{out}} = I_{\text{net}} . \tag{2.16}$$

In considering cases within a non-uniform region, it is more useful to consider a distribution of charge represented by a continuous charge density function,

$$Q(t) = \int_{\Omega} q\left(\bar{x}, t\right) \ d\Omega \ , \tag{2.17}$$

where Ω is a compact subset of an n-space with a piecewise smooth boundary.

Because there can be no sources or sinks of charge within the region, change in total charge is the net flux of current into the region, Ω. In this case the total change in the charge within the region is the sum of the charge flux, or the net current across the boundary of the region,

$$\frac{dQ}{dt} = \frac{\partial}{\partial t} \int_{\Omega} q \ d\Omega = I_{\text{net}} = \oint_{\partial \Omega} j \cdot dS \ , \tag{2.18}$$

where j is the charge flux.

We can use the following generalization of Ohm's law,

$$j = \sigma \mathbf{E} \ , \tag{2.19}$$

where σ is the conductivity, and $\mathbf{E}$ is the electric field. In the simplest application we will assume σ to be constant throughout Ω. Incorporating equation 2.19 into equation 2.18,

$$\frac{\partial}{\partial t} \int_{\Omega} q \ d\Omega = \oint_{\partial \Omega} \sigma \mathbf{E} \cdot dS \ . \tag{2.20}$$

The integral with respect to $\cdot \, dS$ represents the integration of the integrand with respect to normal $\hat{r}$ at the surface $\partial \Omega$, as shown in Figure 2.6.

$$\int_{\partial \Omega} a \cdot dS = \int_{\partial \Omega} a \cdot \hat{r} dA_{\Omega} \tag{2.21}$$

$\mathbf{E}$ is a conservative field; and consequently admits a potential function. The electric

Φ_{out}

$\rho(x,y)$

$\Phi(x,y)$

$\hat{r}$

dS

Ω

$\partial\Omega$
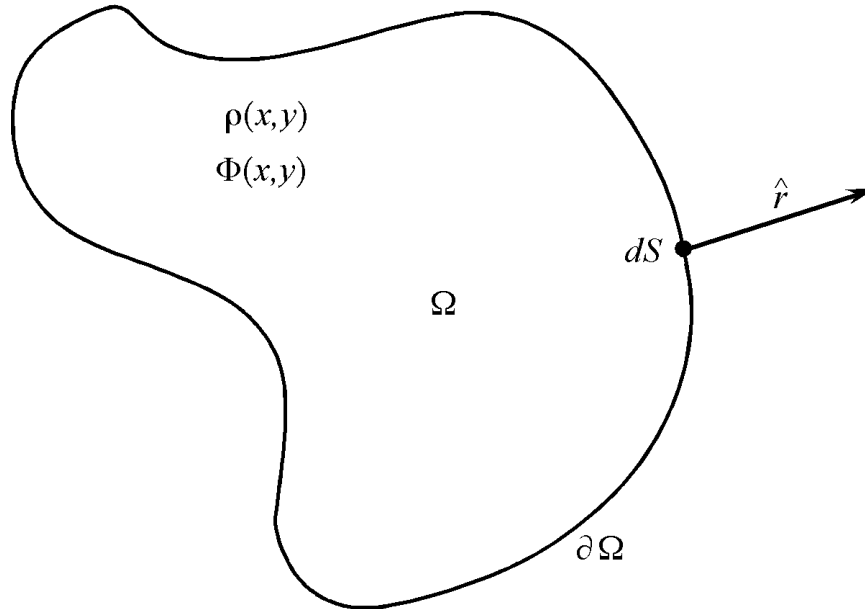
Figure 2.6: Normal vector to boundary $\partial\Omega$ on region Ω

potential, Φ, is the potential associated with $\mathbf{E}$, and is related to $\mathbf{E}$ by

$$\mathbf{E} = \nabla\Phi \ . \tag{2.22}$$

Equation 2.22 allows equation 2.20 to be expressed in terms of the charge density, q, and the electric potential, Φ,

$$\frac{\partial}{\partial t} \int_{\Omega} q \ d\Omega = \oint_{\partial\Omega} \sigma\nabla\Phi \cdot dS = \oint_{\partial\Omega} j \cdot dS \ . \tag{2.23}$$

The divergence theorem,

$$\oint_{\partial\Omega} F \cdot dS_{\Omega} = \int_{\Omega} \nabla \cdot F \ d\Omega \ , \tag{2.24}$$

can be used to express the charge flux across the boundary, $\partial\Omega$, in terms of the potential,

Φ, throughout Ω as

$$\frac{\partial}{\partial t}\int_\Omega q\ d\Omega = \int_\Omega \nabla\cdot(\sigma\nabla\Phi)\,d\Omega = \oint_{\partial\Omega} j\cdot dS\ . \tag{2.25}$$

σ is constant throughout Ω; equation 2.25 can be expressed more compactly as

$$\frac{\partial}{\partial t}\int_\Omega q\ d\Omega = \sigma\int_\Omega \nabla^2\Phi d\Omega\ . \tag{2.26}$$

With q as a continuous function on Ω, this relationship can be expressed in the differential form,

$$\frac{\partial q}{\partial t} = \nabla^2\Phi\ . \tag{2.27}$$

For this work we are interested in the steady-state form of equation 2.27 where $\frac{\partial q}{\partial t}=0$,

$$\nabla^2\Phi = 0\ . \tag{2.28}$$

2.2.2.3 Application to SOFCs

One way to view to the operation of a Ni-YSZ composite anode is as a pair of resistive elements, one conducting only negatively charged electrons and the other conducting only positively charged oxygen ions. The particular characteristic of interest for these phases is their resistance. As seen in Figure 2.7, the actual geometry of a phase within these types of composite electrodes is extremely complicated. Estimating the resistance defies any simple type of characterization. A method is required to make reasonable estimates of the resistance of a phase within a cermet. Developing and applying a method for estimating resistance is one of the the key problems that has to be solved in modeling SOFC anodes.

This problem is very similar to the problem of calculating the effective resistance of the
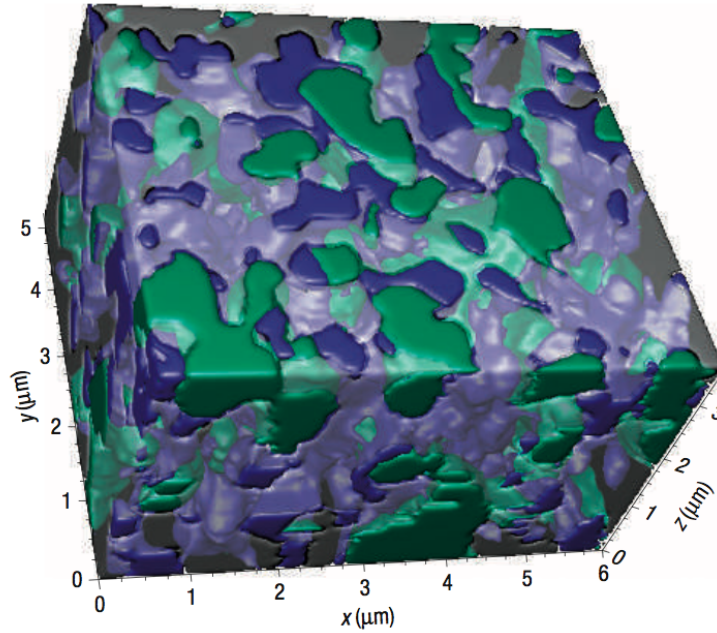
Figure 2.7: Three-dimensional reconstruction of the three-phase structure of a Ni-YSZ cermet from Barnett. (Reprinted by permission from [51].)

region, Ω, in Figure 2.8.

There are 2 knowns:

1. The resistivity within the region Ω, denoted by ρ.

2. The potential along the boundary of Ω, denoted by $\partial\Omega$. $\partial\Omega$ is divided into 4 regions, each with a fixed potential. The fixed potentials on the boundary $\partial\Omega$ are Φ_1, Φ_2, Φ_3, Φ_4.

The first step is to solve for the potential, Φ, across Ω. The governing equation for the potential within the region is equation 2.28. If Ω is treated as either a 2- or 3-dimensional domain, then equation 2.28 can be characterized as an elliptic PDE. In order to solve this PDE it is required that some combination of Φ and $\nabla\Phi$ be determined for the entire boundary. Φ_1 and Φ_2 are fixed unequal values, $\Phi_1 \neq \Phi_2$. In addition we impose
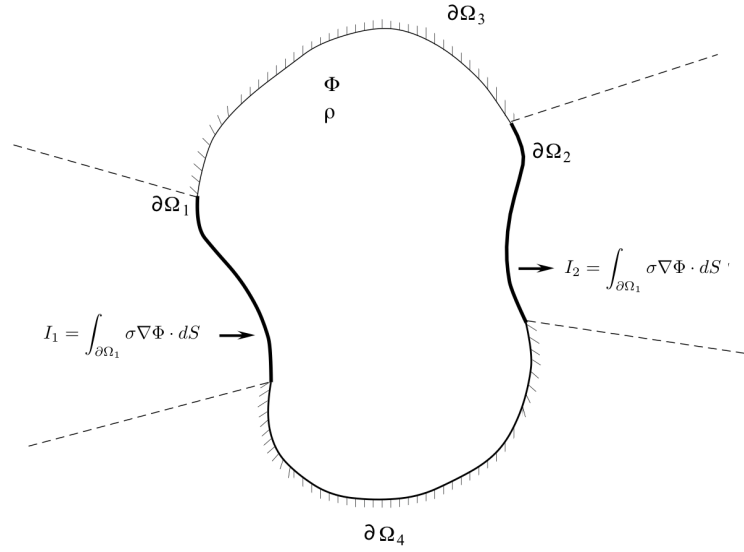
Figure 2.8: Current flow across a non-uniform irregular region

a no-flux condition across boundaries $\partial\Omega_3$ and $\partial\Omega_4$. From the application of equations 2.19 and 2.22

$$0 = \vec{j} \cdot dS = \frac{\nabla\Phi}{\rho} \cdot dS \ . \tag{2.29}$$

$dS \neq \bar{0}$, so

$$0 = \vec{j} = \nabla\Phi \ . \tag{2.30}$$

The no-flux condition across $\partial\Omega_3$ and $\partial\Omega_4$ allows for the boundary conditions of the problem to be specified. For the system in Figure 2.8 the full system can be stated as

$$\nabla^2\Phi = 0 \tag{2.31}$$

$$\Phi|_{\partial\Omega_1} = \Phi_1 \tag{2.32}$$

$$\Phi|_{\partial\Omega_2} = \Phi_2 \tag{2.33}$$

$$\nabla\Phi|_{\partial\Omega_3} = 0 \tag{2.34}$$

$$\nabla\Phi|_{\partial\Omega_4} = 0 \ . \tag{2.35}$$

Once the potential is known throughout Ω, then it is possible to calculate the current fluxes, I across each conducting boundary (in this case $\partial\Omega_1$ and $\partial\Omega_2$). At steady state the current flux across $\partial\Omega_1$ must be the additive inverse of the current flux across $\partial\Omega_2$,

$$I_1 = \int_{\partial\Omega_1} \sigma\nabla\Phi \cdot dS = -\int_{\partial\Omega_2} \sigma\nabla\Phi \cdot dS \ . \tag{2.36}$$

Once the current is calculated, it can be used in concert with the known potential difference across the region and Ohm's law to determine an effective resistance.

$$R_{\text{eff}} = \frac{V}{I} = \frac{|\Phi_1 - \Phi_2|}{I_1} \tag{2.37}$$

In order to replicate this procedure for a spherical-particle-based model of the composite electrode, a number of assumptions and calculations beyond what are presented here are necessary. The full details of these calculations will be presented in Section 2.4.

2.3 Model Description

The main goal of this work is to evaluate the conductivity and percolation characteristics of Ni-YSZ cermets in the context of their use in SOFCs. The primary tool for this will be the model presented within this section. The initial assumption of this model is that the composite electrode can be modeled as a collection of overlapping spheres. With that assumption the model has three requirements which are met separately. In this section the operation of the model and the methodology of the model's calculations will be explained in detail.

1. A domain of spherical objects must be generated. This includes generating spheres whose radii must conform to various sphere size distributions, including monodispersed, simple polydispersed, lognormal, and experimentally measured distribu-

tions.

2. The important geometrical parameters associated with composite electrodes must be calculated from the resulting domain. The parameters of interest include the phase fractions, phase surface areas, TPB length, coordination numbers, percolation, and conductivity participation rates for the particles and connections within the domain.

3. The potential throughout the system must be calculated. In this case, the guiding assumption will be that the inter-particle distance and potential difference between connected particles will be small enough that the entire volume of each particle can be considered to be at one potential.

2.3.1 Domain Generation

2.3.1.1 Particle Placement

As discussed in Section 2.1, most of the previous efforts to utilize particle-based models to describe composite anodes used the methodology introduced by Bennett [6]. Bennett's approach places new particles just in contact with existing particles in the ensemble. Particle overlap and polydispersed particle size distributions can then be achieved by resizing the particles in place. This method is unsuitable for this work because we will consider the packing of particles whose sizes vary greatly, in some cases by orders of magnitude. Bennett's method relies on an acceptance test for new particles. In the case when particles do not have a monodispersed size distribution, this method will result in a higher acceptance rate for smaller particles and a higher rejection rate for larger particles. Controlling the size distribution of the particle ensemble is extremely difficult using this method. To avoid this problem, a packing-sintering approach is used. This method assigns a penalty function to each particle as it is serially added to the

ensemble. The penalty function achieves its minimum when the particle reaches the desired contact and overlap position with respect to its neighboring particles. Using this method, random close packing can always be established between particles, regardless of their relative size.

The first step is to place a particle at a random location, (x_p, y_p) in the x-y plane of the cermet box. The next step is to determine the largest z location at which the particle will contact an existing particle, or the $z = 0$ boundary of the box. To accomplish the first task we consider the locations in the x-y plane of all existing particles. Let the x-y location of the ith existing particle be represented by (x_i, y_i). The radii of the ith particle and of the new particle are r_i and r_p, respectively. The test particle contacts the ith particle if the sum of the radii is less than the distance between the particles,

$$(r_i + r_p) \leq \sqrt{(x_i - x_p)^2 + (y_i - y_p)^2} \ . \tag{2.38}$$

If the set of particles satisfying this condition, U, is empty, then the test particle is placed at the location $(x_p, y_p, 0)$, as illustrated in Figure 2.9

As illustrated in Figure 2.10, if U is non-empty then the location, (x_i, y_i, z_i), of the existing particle within U with the largest z value is used to determine the initial location of the test particle. The initial z location of the test particle, z_p, is determined using equation 2.10

$$z_p = z_i + \sqrt{(r_i + r_p)^2 - (x_i - x_p)^2 + (y_i - y_p)^2} \ . \tag{2.39}$$

The location (x_p, y_p, z_p) establishes a distance between the particles equal to the sum of their radii. A path is calculated from the initial contact point to the final position of the particle using a set of differential equations representing the force of gravity and inter-particle forces. The final resting point of the particle is found when either the

Figure 2.9: Initial placement of a non-intersecting particle

particle is a specified distance from each of its neighboring particles, or the z coordinate of the particle is 0. A penalty function based on these conditions is used to calculate the acceleration of the particle, until the minimum is reached. The desired distance between two particles is determined by an overlap parameter, λ, and the radii of the two interacting particles. λ parameterizes the length between the minimum and maximum possible distances allowed between two particles. The maximum distance between two contacting particles, $d_{\max}$, is the sum of the radii of the two particles. The minimum distance is the point at which the radius of the circle of intersection between the particles is larger than the minimum of the two radii. This distance is:

$$d_{\min} = \sqrt{|r_1^2 - r_2^2|} \ . \tag{2.40}$$
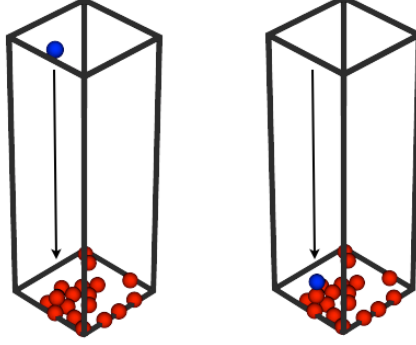
Figure 2.10: Initial placement of an intersecting particle

The desired spacing between the two particles is then

$$d_0 = d_{\min} + \lambda \cdot (d_{\max} - d_{\min}) \ . \tag{2.41}$$

To place the particle at this spacing, the penalty function is used to define an acceleration vector for the particle. The path of the particle is integrated using the penalty function to define the acceleration vector of the particle. The function describing the inter-particle force between particles is:

$$\bar{F} = \frac{d - d_0}{2} \ . \tag{2.42}$$

In addition, both a normal force $\bar{F}_{\mathrm{N}}$ with respect to the $z = 0$ boundary, and a viscous damping force $\bar{F}_{\mathrm{D}}$ are added to the differential equations in order to limit oscillatory behavior in the solution transients. The normal force between particles and the $z = 0$ boundary is:

$$\bar{F}_{\mathrm{N}} = \begin{cases} p_{\mathrm{rad}} & ; p_z > p_{\mathrm{rad}} \\ z & ; p_z \leq p_{\mathrm{rad}} \ . \end{cases} \tag{2.43}$$

The damping force is the additive inverse of the velocity, $\bar{F}_{\mathrm{D}} = -\hat{V}$.

The complete differential equation is:

$$\frac{d\ddot{\bar{X}}}{dt} = \sum_{i=1}^{N_p} \frac{\bar{p} - \bar{v}_i}{\|\bar{p} - \bar{v}_i\|} \cdot \frac{d - d_0}{2} + \bar{F}_{\mathrm{N}} + \bar{F}_{\mathrm{D}} \ . \tag{2.44}$$

The final placement of the particle is demonstrated in Figure 2.11. Note that, as the boundaries of x-y plane are periodic, particles can translate through the x-z and y-z boundary planes.

Figure 2.11: Final particle placement

2.3.2   Particle Size Determination

Calculations are made using 4 different particle size distributions:

1. Mondispersed and simple polydispersed particle distributions.

2. Distributions calculated based on experimental data.

3. Integer-based discrete particle size distributions.

4. Truncated lognormal particle size distributions.

2.3.2.1 Monodispersed and Simple Polydispersed Particles

Calculating the properties of mondispersed and simple polydispersed distributions will allow comparison to previous computational studies on composite cermet calculations. Because the filling problem is being solved in a different fashion than in previous studies it is important to consider the case of the simple monodispersed distribution, and the case in which the cermet is represented as a combination of two particle sizes, with each particle size assigned based on the type of particle represented. For structures with polydispersed particle distribution consisting of only two particle sizes assigned by phase, the ratio between particle sizes will be 1:0.781 YSZ:Ni. This ratio is based on the assumption that the precursor mixture for the composite anode is equal parts YSZ and nickel oxide (NiO) by volume, the percursor particles of YSZ and NiO are uniform and size, and there is a negligible amount of pore space in the precursor mixture. The manufacturing of the cermet involves the reduction of the NiO phase to Ni. The density of the precursor NiO is 6.67 g/cm^3, and the density of pure Ni is 8.91 g/cm^3.

2.3.2.2 Distributions Calculated from Experimental Data

Experimental measurement of precursor particles from Ni-YSZ composite anodes will be used to formulate a size distribution of particles for computation. The data will show non-analytical continuous size distributions. These distributions will typically contain particles with size differences of several orders of magnitude. In particular, studies will be based on particle arrays based on the particle size distributions described by Cho et al. [11].
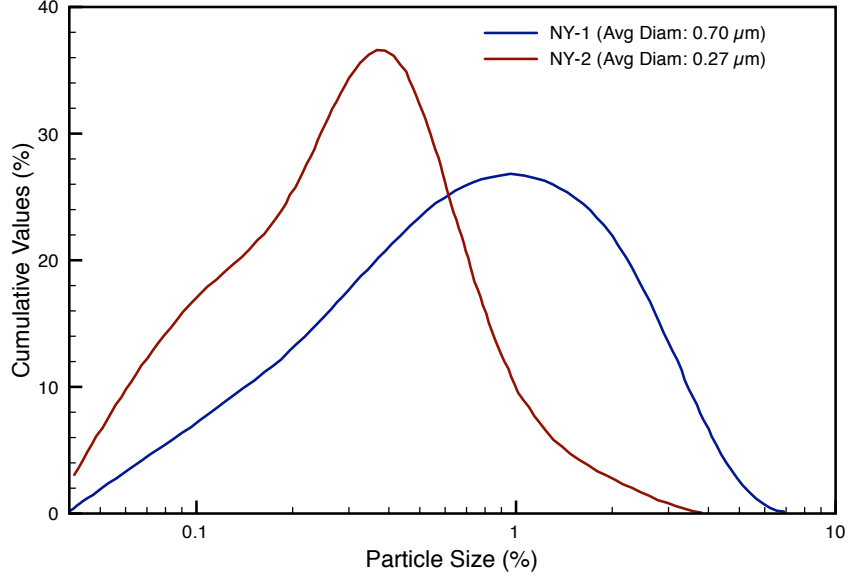
Figure 2.12: Particle size distributions published by Cho et al. [11]

Because these are empirical distributions with no known analytical form, there is no known analytical function which samples these distributions. These non-analytical distributions are sampled using the Metropolis-Hastings (MH) [36, 25] algorithm to sample the empirical distributions. The algorithm generates a Markov chain, the values of which have a distribution equivalent to the desired distribution. The process used in this study for drawing a sample from probability distribution, P, is described below.

1. A proposal distribution, Q, which can be directly sampled, is chosen. For this study, a lognormal distribution is used. The probability density of the lognormal distribution is

$$Q(x; \mu, \sigma) = \frac{e^{-\frac{(x-\mu)^2}{2\sigma^2}}}{\sqrt{2\pi\sigma^2}} \; . \tag{2.45}$$

The following function is used to generate a sample, x, with mean μ, and variance σ^2, from the lognormal distribution

$$x = \ln\left(1 + \frac{\sigma^2}{\mu^2}\right) + x_g \cdot \sqrt{\ln\left(1 + \frac{\sigma^2}{\mu^2}\right)} \tag{2.46}$$

where x_g is a sample pulled from a normal distribution. The value of the parameters μ and σ used were determined by a least-squares analysis comparing the lognormal distribution to the empirical distribution. This produced a lognormal distribution which matches more closely the empirical distributions, as compared to a lognormal distribution with the same μ and σ^2 as the empirical distributions in this study.

2. The initial value of the Markov chain, x_0, is set to a random value within the range of the empirical distribution. This becomes the current state of the Markov chain, x^t.

3. Draw a value, x, randomly from the lognormal proposal distribution.

4. Calculate, the acceptance ratio, α,

$$\alpha = \frac{P(x) \cdot Q(x^t)}{P(x^t) \cdot Q(x)}. \tag{2.47}$$

Then if $\alpha \geq 1$ then $x^{t+1} = x$; otherwise, $x^{t+1} = x$ with probability α, and $x^{t+1} = x^t$ with probability $1 - \alpha$.

For this case a modified lognormal distribution is used as the test distribution which is applied for the Markov chain. Examples of MH-generated sample distributions compared to the Cho data are shown in Figures 2.13 and 2.14.

The application of the MH algorithm used for this study has been simplified from the most general case, taking advantage of specific knowledge about the nature of this problem. While the lognormal distribution exists on the interval $0 < x < \infty$, the desired probability distributions being reproduced exist on finite non-negative intervals of the form $a \leq x \leq b$. In order to disallow any values outside of the interval $a \leq x \leq b$, $P(x; x < a, x > b)$ is set to the 1×10^{-14}. This almost perfectly prevents any results which fall outside of the desired interval. Setting $P(x; x < a, x > b) = 0$ will result
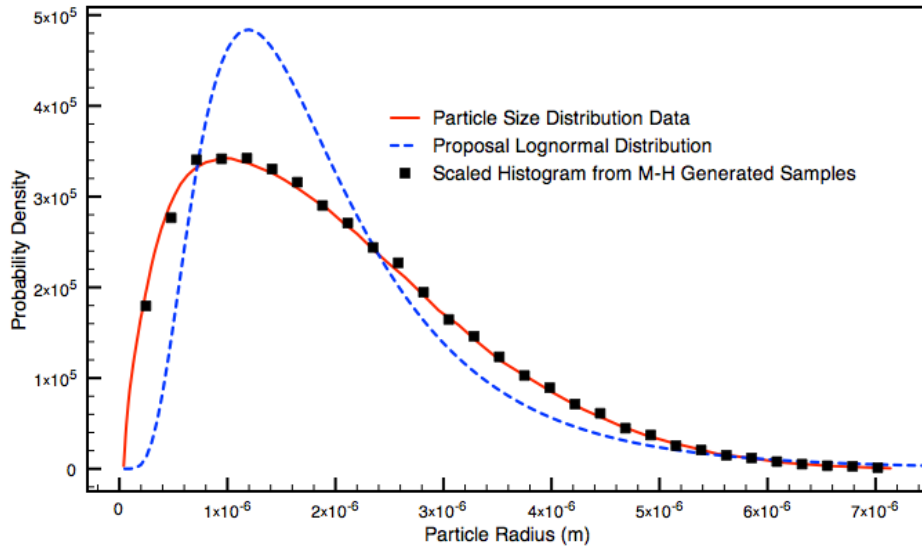
Figure 2.13: Metropolis algorithm samples from particle size distributions published by Cho et al., 2008

$\alpha = \infty$, and could cause errors in any computer based code.

2.3.2.3   Lognormal Particle Size Distributions

The distributions used in Section 2.3.2.2 do not have known analytical forms. For that reason it is not possible to parameterize these distributions and then examine the effect of changing parameters on important outputs. Lognormal distributions a set of well-understood, analytical probability distributions which can be easily parametrized. In addition, lognormal distributions are similar to the empirical distributions explored in Section 2.3.2.2. It was for this reason that lognormal distributions were chosen as the proposal distributions for the duplicating the empirical distributions via the Metropolis-Hastings methodology.
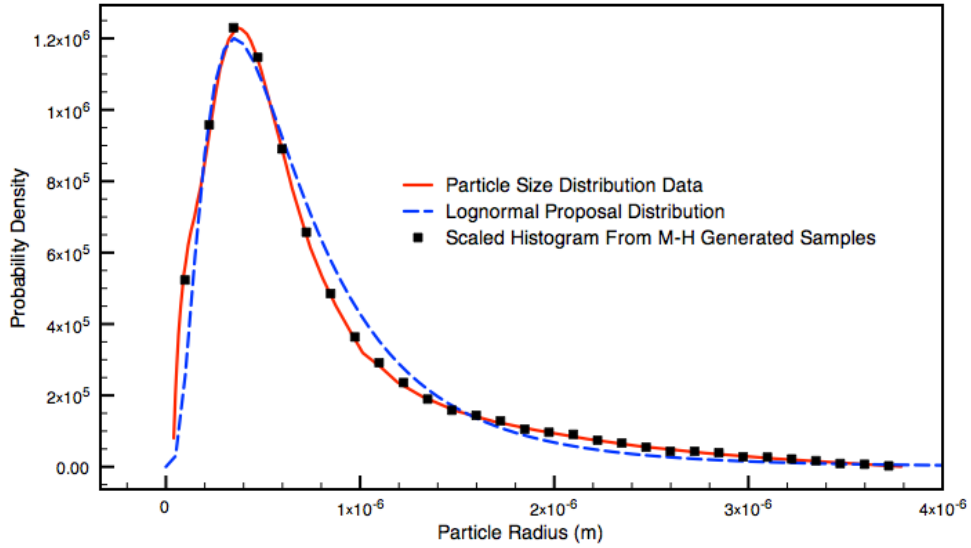
Figure 2.14: Metropolis algorithm samples from particle size distributions published by Cho et al., 2008

A lognormal distribution has the following probability density function, f,

$$f(x; \mu, \sigma) = \exp^{-\frac{(ln(x)-\mu)^2}{2\sigma^2}} \quad . \tag{2.48}$$

μ is the mean of the logarithm of the variable, x, and σ is the logarithm of the variance. The mean, variance, and standard deviation of the lognormal distribution, respectively, are

$$\mathrm{E}[X] = e^{\mu + \frac{1}{2}\sigma^2} ,$$

$$\mathrm{Var}[X] = (e^{\sigma^2} - 1)e^{2\mu + \sigma^2} ,$$

$$\mathrm{Std.\ Dev}[X] = \sqrt{\mathrm{Var}[X]} = e^{\mu + \frac{1}{2}\sigma^2}\sqrt{e^{\sigma^2} - 1} .$$

The logarithm of samples from this distribution have a normal distribution. This allows a sample from a normal distribution, s_{norm}, to be mapped to a sample from a lognormal distribution, s_{ln}, via

$$s_{ln} = s_{\text{norm}} \cdot \sqrt{\ln\left(1 + \frac{\sigma^2}{\mu^2}\right)} + \ln(\mu) - \frac{\ln\left(1 + \frac{\sigma^2}{\mu^2}\right)}{2} \ . \tag{2.49}$$

Methods for sampling a normal or Gaussian distribution can be found in a number of sources. For further information on the method used for this work, the reader is referred to pages 292–294 of Section 7.2 of *Numerical Recipes in C++* [39].

2.3.3 Calculation of Cermet Properties

After the computational domain has been generated and populated with particles, the next step is to calculate the geometrically-based parameters of the resulting virtual electrode. The geometrical parameters fall into two categories: Parameters which are primarily associated with the solid phases, and parameters which are primarily associated with the void phase. These parameters are:

1. **Solid Phase Parameters**

    (a) particle coordination numbers

    (b) TPB and connectivity

    (c) relative phase volume

    (d) surface areas of the two solid phases

    (e) inter-particle resistance

2. **Void Phase Parameters**

(a) porosity

(b) tortuosity of the void phase

(c) mean pore diameter

The solid phase parameters and porosity are important to all the aspects of the modeling of composite electrodes that will be presented in this work. The void phase parameters, excepting porosity, are only relevant to the discussion in Chapter 5.

2.3.3.1 Particle Coordination Numbers

All of the particles within the cermet are compared by location to find the intersecting particles within the cermet. Taking all pairs of particles p_i and p_j such that $i > j$ where particle p_i is located at the point $c_i = (x_i, y_i, z_i)$ and has a radius, r_i, a distance test determines whether or not the particles intersect. If the distance, d, between the respective particle centers is less than the sum of the particle radii, then the particles are assumed to intersect. The next step is to calculate the radius of the intersection, which using from the law of cosines and the Pythagorean theorem is

$$r_{intersection} = \sqrt{\left| r_i^2 - \frac{\left(r_i^2 + d^2 - r_2^2\right)^2}{d^2} \right|} \; . \tag{2.50}$$

With the radius of intersection, both the area and circumference of the intersection can be calculated.

From this process three pieces of information are saved:

1. A list of all particles intersections along with the area of intersection,

2. A separate list of all heterogenous particle intersections along with the circumference of the intersection,

3. A list, for each particle, of the particles with which it intersects.

With the intersection information generated above it is possible to calculate the co-ordination numbers, Z_x, of the cermet. The overall coordination number, Z, can be calculated by taking the total sum of intersecting particles for each particle in the ensemble and then dividing by the number of particles. The coordination numbers which are calculated are:

1. Z, Overall average coordination number.

2. Z_i, Average coordination number for ionically conducting particles.

3. Z_e, Average coordination number for electronically conducting particles.

4. Z_{i-i}, Average coordination of ionically conducting particles with respect to ionically conducting particles.

5. Z_{e-e}, Average coordination of electronically conducting particles with respect to electronically conducting particles.

2.3.3.2 TBP Calculations

After the intersections of the cermet particles have been tabulated, the location and extent of the TPB, as well as the conductance between particles, are calculated. The nominal TPB length of the cermet is simply the sum of the circumferences calculated from the particle intersections, but a significant portion of that nominal length can be occluded by third particles. Calculating the actual TPB length is accomplished by discretizing the TPB between pairs of particles and determining what portion of that TPB is in fact interior to other particles in the cermet.

The first step is to determine the equation of the circle which describes the nominal TPB. The center point as well as two vectors in the plane of the circle are required.

The center point can be found via trigonometry. Letting $\bar{d}$ be the vector $\bar{c}_i - \bar{c}_j$, the center point of the intersection, $\bar{C}$, between two particles, p_i and p_j, is:

$$\bar{C} = \bar{c}_i + \bar{d}\,\frac{\left(r_i^2 + \|d\|^2 - r_j^2\right)}{r_i\|d\|}\;. \tag{2.51}$$

Because any two vectors in the plane of the circle can be used for this calculation, there is no one method to determine the identity of the vectors. For this work the two vectors in the plane of the circle are generated as follows:

$$\bar{V}_1 = (\bar{d}_y, -\bar{d}_x, 0), \tag{2.52}$$

$$\bar{V}_2 = \bar{d} \times \bar{V}_1\;, \tag{2.53}$$

where $\times$ is the vector cross product operator.

The ξ parametrized equation of the nominal TPB between intersecting particles p_i and p_2 is

$$\bar{P}_{\text{TPB}}(\xi) = \bar{C} + \bar{V}_1 \sin\xi + \bar{V}_2 \cos\xi,\quad \xi \in [0, 2\pi]\;. \tag{2.54}$$

To assess the true length of the TPB, a set, N, of n points (usually 100) are generated along the nominal TPB by allowing $\xi = \frac{2\pi}{n}$. Each of these points then represents a partial arc of the circle of length Δs, where Δs is the total perimeter of the circle divided by the number of points:

$$\Delta s = \frac{2\pi r}{n}\;. \tag{2.55}$$

Each point in N is evaluated as to whether that point is located within any particle intersecting either p_i or p_j. The recorded TPB length for the intersection between p_i and

p_j is then scaled by the fraction of points in N not located within any other particle. If multiple non-adjacent points are removed from N via this process, the TPB generated by the intersection of p_i and p_j is a set of arcs, defined by points within N.

The set of of remaining points within N define the TPB between particles p_i and p_j. The TPB can be visualized using the saved points. The length of the TPB segments generated by the intersection of p_i and p_j is calculated as the fraction of points remaining in N multiplied by the circumference of the circle of intersection. The total TPB length for the cermet is then the sum of the scaled TPB lengths from each intersection between heterogenous particles.

The next step is to determine the connectivity of the TPB. The goal is to determine which segments of the TPB are in contact, as well as the frequency and extent of contacting networks of triple phase boundaries. The first step is determining the segments which will be used in the comparison process. The TPB segments determined using the procedure outlined above are not necessarily contiguous segments. The subtraction of points can create segments which are composed of discontiguous arcs. Once the TPB segments are separated into segments which consist of contiguous sets of points, the distances between all points within the contiguous segments are calculated. If any calculated distance is less than the criterion distance,

$$\Delta s_1 + \Delta s_2 \ , \tag{2.56}$$

then the two segments are assumed to intersect and to be part of one contiguous curve.

Note that Δs_1 and Δs_2 are the curvilinear distance between points on the arc, which is longer than the actual Cartesian distance between the points. The criterion captures the distance between points in two intersecting arcs where the actual intersection occurs halfway between points which are used to define the arcs. Using this method there will

be a very small number of cases in each calculation where two curves which are not actually connected are projected to be connected.

2.3.3.3 Inter-Particle Resistance

The conductance of a homogenous volume with a constant conductivity, σ, a fixed cross-sectional area, A, and a length perpendicular to A, l, is:

$$G = \frac{\sigma A}{l} \ . \tag{2.57}$$

If the volume is assumed to be a sphere then $A = 2\pi r$ and the conductivity can be restated as:

$$G = \frac{\sigma \pi r^2}{l} \ . \tag{2.58}$$

Sunde used the results determined by Feng [17] to calculate the resistance between homogeneous particles in a disordered random sphere network. Given an intersection diameter between two homogeneous particles of 2δ the conductance between the two particles can be estimated as the conductance of a cylinder of diameter and length 2δ:

$$G = \frac{\sigma \pi \delta^2}{2\delta} = \frac{\sigma \pi \delta}{2} \ . \tag{2.59}$$

For the same calculation Schneider [42] uses an empirical relation developed by Argento and Bouvard [3]. This relation utilizes the particle radius, r_p, and the intersection radius, r_c. The assumption is that the base conductance between two particles, G_i, is determined by the conductance of a cylinder of radius r_c and length r_p:

$$G_i = \frac{\sigma \pi r_c^2}{r_p} \ . \tag{2.60}$$

The base conductance is adjusted depending on the ratio r_c/r_p:

$$
\begin{cases}
G = 0.899 \, \frac{r_p}{r_c} \sqrt{1 - \left(\frac{r_c}{r_p}\right)^2} \, G_i, & \text{for } \frac{r_c}{r_p} < 0.744 \\[2em]
G = G_i, & \text{for } \frac{r_c}{r_p} > 0.744 \ .
\end{cases}
\tag{2.61}
$$

The initial approach used to determine the inter-particle conductance is a variation of the methods listed above. Given two homogenous intersecting particles with a radius of intersection, r_c, and a distance between the particle centers, d, the conductance, G, is assumed to be equivalent to a cylinder with radius r_c and length d.

$$
G = \frac{\sigma \pi r_c^2}{d}
\tag{2.62}
$$

These results were then compared to a finite element solution, using Ansys, of the potential over a small set of particles in a cubic volume. The system, shown in Figure 2.3.3.3, contained 40 particles. The solution was obtained with a fixed potential dif-
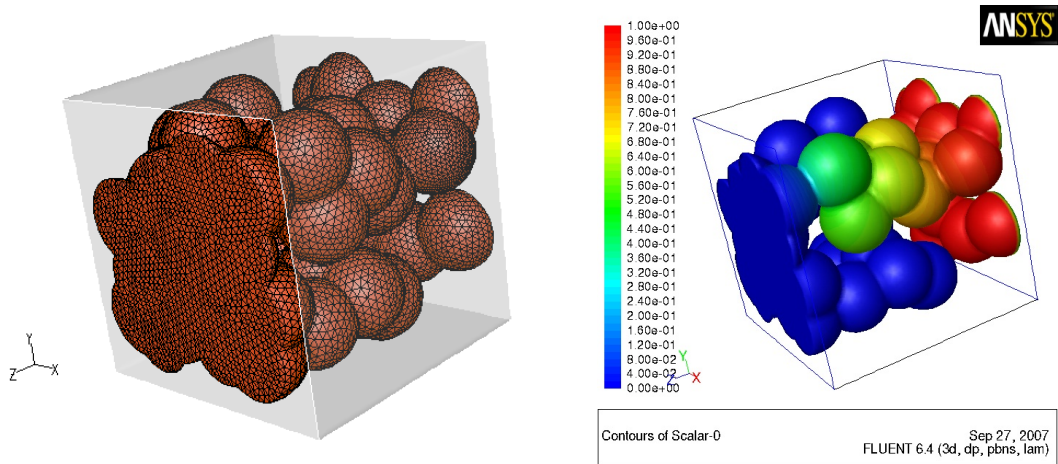
Figure 2.15: FEM mesh and solution for particle array by Jay Sandal of Ansys [41]

ference across the cubic volume. In the particle model, particles are assumed to have

a uniform potential throughout the particle volume. We compared the solution of the potential of a particle in the network model to the potential at the center of a particle within the finite element solution [41]. Because the scale of the particle model is much coarser than that of the finite element model, it is expected that there will be discrepancies between the two results. Figure 2.3.3.3 shows the potential differences between the particle centers of intersecting particles. For intersections between conducting particles not intersecting the boundary, the average difference in potential drop between the two methods was 3.1% of the total potential drop, and the standard deviation was 3.4% of the total potential drop. The largest discrepancy occurs at a point where the entire current flow travels through only one particle, with a angle between the current flow inlet and outlet of nearly 180°. In this case there is a 50% difference in the center-to-center potential drop. The error in the potential drop was much smaller between particles with a higher number of conducting neighbors, and in cases where the angular displacement of the current inflows and outflows was small. In this work the packing algorithm used guarantees a high coordination between particles. We cannot use these calculations to calculate a limit on the expected error from these calculations. But they do indicate that in the error of the particle potentials will be minimized in systems with high coordination between conducting particles.

2.3.3.4   Porosity and Solid Phase Fractions

The porosity and the solid phase fractions are determined via a Monte Carlo method. The procedure to calculate the porosity is outlined below:

1. A random test point within the geometrical limits of electrode model, $p = (x,y,z)$, is selected.

2. A sum, which is initially set to zero, is maintained.

3. If p is not located within the radius of an electronically conducting particle nor
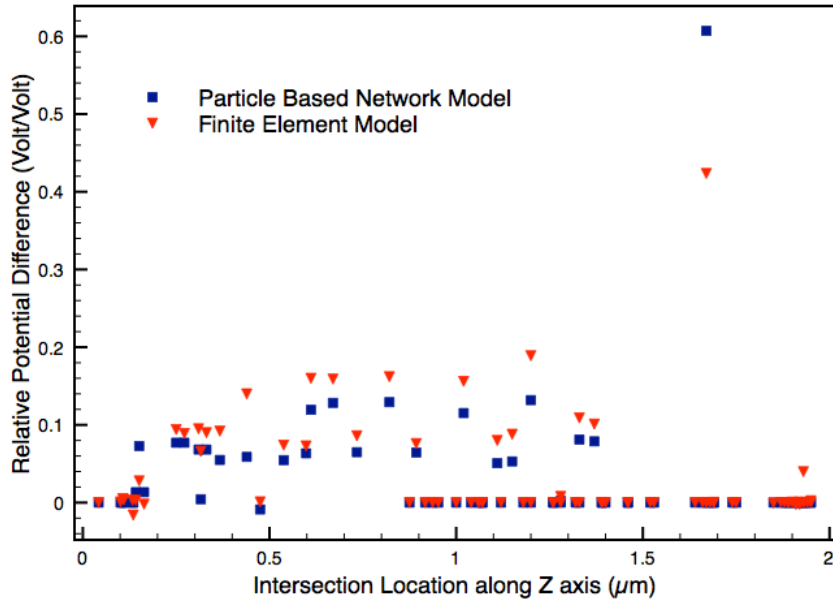
Figure 2.16: Comparison of potential, Φ, between particle model and FEM particle array by Jay Sandal of Ansys [41]

located within the radius of an ionically conducting particle, the the sum is incremented by one.

4. The porosity is then estimated as the value of the sum divided by the total number of test points.

In practice, 10,000 test points are usually used to estimate the porosity.

The method for calculating solid phase fraction differs from the porosity calculation because allowing particles to overlap means that the test point from a Monte Carlo method may lie inside of two different particles of differing types, corrupting the calculation. In order to avoid this problem the solid volume of each particle is calculated separately. The resulting particle volumes are then summed by type to provide an accurate measure of the aggregate volume of each solid phase.

1. A random test point within the radius of each particle, $p = (x,y,z)$, is generated.

2. A sum, which is initially set to zero, is maintained.

3. If p is not located within the radius of any neighboring particle, the sum is incremented.

4. If p is located within the radius of any neighboring particles, q_i, the distances between p and the centers of all of the particles within whose radius p falls are calculated.

5. If the the distance between p and the particle whose volume is currently being evaluated is the smallest distance, the sum is incremented; otherwise the sum is not changed.

6. The volume of the particles is then calculated as the nominal volume: $4\pi r^3/3$, multiplied by the sum, and divided by the total number of test points used.

In practice, 1000 test points are usually used to estimate the volume of each particle.

2.3.3.5 Solid Phase Surface Areas

The surface areas of the solid phases will be used in the calculation of heterogeneous chemistry. The method used to determine the surface area of the solid phases is similar to the method used to determine the phase volumes. A set of points are created which describe the surface of each particle within the system. For this work the typical number of points was 850. From the initial set of particles it is then necessary to determine the subset of particles which are not located within the radius of any other particle. The surface of the particle in question is the nominal spherical surface area,

$$A = \frac{4\pi r^3}{3} \ ,$$

(2.63)

divided by the number of initial points.

2.3.3.6   Void Phase Parameters

The tortuosity, porosity, average particle radius, and average pore diameter are esti-mated via a test-particle Monte Carlo (TPMC) method. TPMC is used to compute the motion of representative molecules in the gas flow through a porous structure. Com-putation at the molecular level is necessary for predicting rarefied gas flows where the Navier-Stokes equations for continuum dynamics no longer apply. Instead, TPMC uses probabilistic techniques to solve the Boltzmann equation for fluid flows. A number of simulated molecules are used to represent a large number of real molecules to give an accurate statistical description of the flow characteristics.

Details of the TPMC calculation method are given in *Solid-Oxide Fuel Cell Electrode Microstructures: Making Sense of the Internal Framework Affecting Gas Transport* by Hanna [23] and outlined below:

1. An idealized porous structure is created by placing simple geometric objects in a defined volume, to be referred to as the domain. Object placement can be governed by any set of rules to allow for varying levels of overlap, connectivity, etc., until some desired porosity or structure characteristics are obtained. Typically, sphere packings are used. The boundaries of the domain are given appropriate boundary conditions for the desired model (can mimic solid surfaces, create infinite periodic extensions, etc.).

2. The TPMC model does not require any meshing, since collisions are calculated using simple geometric equations for the intersection of a ray and a quadric surface.

3. After the porous structure or solid phase is constructed, a gas-phase species is created. A number of representative molecules is then used to simulate the real

gas.

4. A simulated gas molecule is randomly placed in the pore space of the idealized porous medium. It is assigned a speed (from a Maxwell-Boltzmann distribution) and direction (uniform distribution of all available directions). Possible collision locations are calculated between the ray extending from the molecule location along its assigned direction and any spheres it may intersect. The intersection is taken to be the closest point to the current location along the ray.
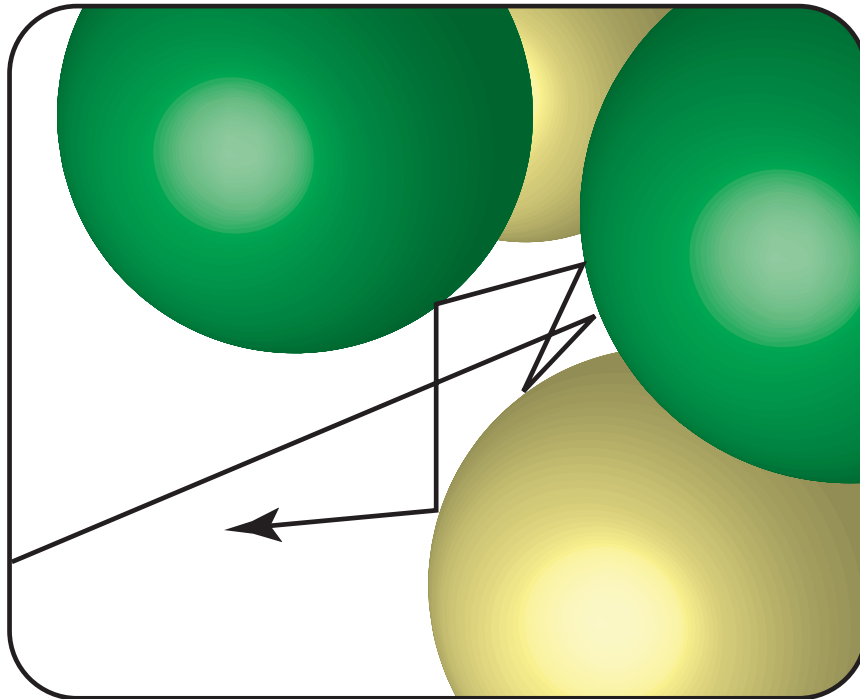
Figure 2.17: Example molecule trajectory for Kn ≤ 1

5. Since diffuse reflections are used at solid surfaces, it is implicitly assumed that molecules adsorb briefly, then desorb from the surface with no memory of incident angle. As a first guess, it is assumed that the sticking coefficient is unity so that all molecules desorb on the surface and therefore reflect diffusely (otherwise, some fraction may reflect specularly). Desorbing molecules are assigned a new speed

(consistent with the average kinetic energy) and a new set of directions from the cosine law [19]).

6. Subsequent intersections are computed in the same way, with molecules getting a new speed and direction at each collision. If a molecule collides with a domain boundary, the appropriate boundary conditions are used. This process repeats for a specified amount of time or number of steps (ideally large enough so that molecules have sampled representative areas of the pore structure). After this set time, the final molecule position is recorded, along with its total travel distance, displacement, and any other quantities.

7. Steps 4–6 are repeated for all molecules, and the desired statistical and averaged parameters can be calculated.

    (a) The effective diffusivity is

    $$D^e = \frac{<R^2>}{6t_d} \; ; \tag{2.64}$$

    (b) and the tortuosity is

    $$\tau = \Phi \frac{\mathcal{D}_{\mathrm{Kn}}^e}{D^e} \tag{2.65}$$

    where $<R^2>$ is the average of the square of the particle displacement, t_d is the diffusion time, and $\mathcal{D}_{\mathrm{Kn}}^e$ is the effective Knudsen diffusivity.

2.4 Network Model

Once the domain of the cermet is set up, the phase conductivity of the cermet is calculated by using a network model to calculate the potential field, as well as the ionic and electronic current flow throughout the cermet. The flow of electrons and ions through the solid matrix is modeled with a network model which treats each particle within the

system as a node in a network. Intersecting particles of the same type are treated as nodes connected by a resistor, where the resistance between particles is calculated using geometry and material properties.
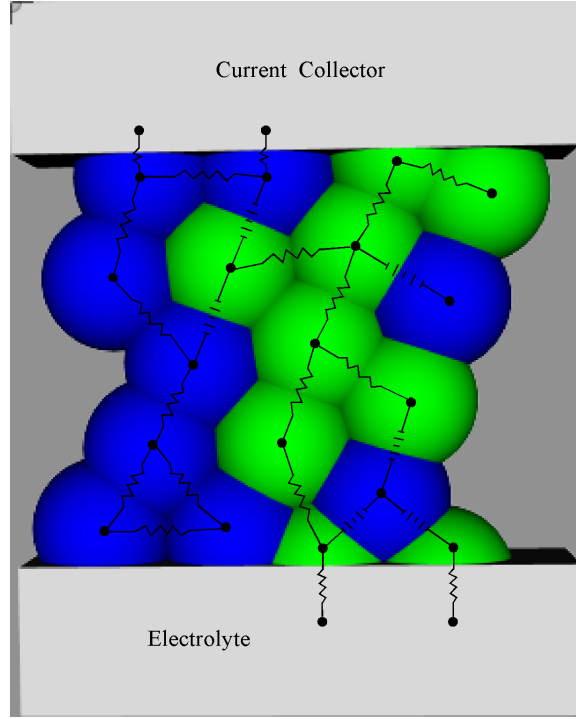
Figure 2.18: Illustration of the relationship between the resistor network model and the geometry of the composite cermet

Intersections between particles of differing types are treated as nodes connected by a current source, where the current is determined by the local triple-phase boundary electrochemistry. The net current across each cermet particle is

$$i_{\text{net}} = i_{\text{R}} + i_{\text{F}} \tag{2.66}$$

$$= \sum_{k}^{N_s} R(\Phi_k - \Phi) + \sum_{k}^{N_{\text{TPB}}} i_{\text{F}} . \tag{2.67}$$

For each particle within the system:

$$0 = \frac{dQ}{dt} = i_{\text{net}} = i_{\text{R}} + i_{\text{F}} \tag{2.68}$$

$$= \sum_{k=0}^{N_s} R(\Phi_k - \Phi) + \sum_{k=0}^{N_{\text{TPB}}} -\dot{\omega}_{\text{e}^-} \cdot l_{\text{TPB}}^k \ . \tag{2.69}$$

N_s is the number of intersecting particles of the same type, N_{TPB} is the number of heterogenous intersecting particles, R_k is the resistance between particles, and Φ is the potential. The equations are integrated using a backward differentiation formula. In this case, the network model uses the CVODES solver [9], a backward-difference numerical method, to integrate the following charge conservation equation in time until the steady-state criteria are met. As only the steady-state solution is of interest, terms associated with the capacitive current have been left out of the charge transfer equation; these terms evaluate identically to 0 at steady state. The independent variable in this relation is Φ, the potential of the particle being evaluated.

Chapter 3

Calculating Cermet Geometry and Performance Using Particle-Based Models

3.1 Introduction

The model described in Chapter 2 allows the calculation of geometrical and electronic properties of Ni-YSZ composite anodes. In this chapter the nominal performance and the variability of the performance of several geometries will be examined. Particular emphasis will be paid to the relationship between the calculations of this work and the existing body of composite anode modeling results, as well as the relationship between the modeling and experimental results. In the first part of the chapter, the properties of monodispersed and simple polydispersed particle ensembles will be explored. As detailed in Section 2.1, monodispersed and simple polydispersed particle ensembles form the basis of the majority of previous particle-based modeling efforts for composite electrodes.

3.2 Monodispersed and Simple Polydispersed Systems

This section will focus on the behavior of two models of Ni-YSZ systems whose particle size distributions are simple:

1. Type A: monodispersed systems where the size of all particles are the same.

2. Type B: polydispersed systems where the particle size is determined by particle type, with a radius ratio of 1.0:0.781 between YSZ and Ni particles, respectively.

3.2.1 System Size Determination

An important question for studying the geometrical and conductivity results is: How large must the geometry of the ensemble be in order that the results are not impacted by boundary effects? The boundary conditions of the system in the x and y directions are periodic.

$$\Phi(x = 0, y, z) = \Phi(x = L_x, y, z) \tag{3.1}$$

$$\Phi(x, y = 0, z) = \Phi(x, y = L_y, z) \tag{3.2}$$

In the z direction, defined as the direction normal to both the electrolyte and current collector boundaries, the boundary conditions are Dirichlet.

$$\Phi(x, y, z = 0) = \Phi_0 \tag{3.3}$$

$$\Phi(x, y, z = L_z) = \Phi_1 \tag{3.4}$$

The parameters of interest depend, to varying degrees, on the the domain size, the overlap parameter, λ (defined in Section 2.3.1.1), and the boundary conditions. The domain length or size will be defined in terms of the parameter L/r. L describes the dimensions of the system boundaries where $L = L_x = L_y = L_z/3$, and r is the mean

particle radius. The parameter groups of interest are:

1. phase fractions,

2. coordination numbers of the particles,

3. conductivity and percolation.

Each of these parameter groupings will be examined separately. In each case the system will have two phases: An electronically conducting Ni phase and an ionically conducting YSZ phase. Each particle within the system will have a 50% probability of being either Ni or YSZ. The results will be considered for systems both type A and type B. L/r will take on values of 12, 16, 20, 24, 28, and 32, and λ will take on values 0.965, 0.970, 0.975, 0.980, 0.985, 0.990, and 0.995. A total of 42 different cases will be evaluated. Some cases will be omitted from the graphs for clarity.

3.2.1.1 Phase Fractions and Particle Counts

For meaningful simulations, phase fractions of the system should have no dependence on the boundaries or the domain size, regardless of the boundary conditions. The results of the variation in phase fraction measurement for both types of systems are presented in Figures 3.1, 3.3, and 3.4. Some cases are omitted for visual clarity. The lines between data points serve to guide the eye and do not represent an underlying functional relationship. Selected data for variability of these systems is shown in Tables 3.2, 3.3, and 3.4. Tables for the entire data set are in Sections A.1 and A.2 of Appendix A. In these calculations there is no systemic dependence of phase fraction on the domain size. Error bars are not shown in Figures 3.1, 3.3, and 3.4 because the standard deviation is small in comparison with the measured mean value. In Figure 3.1 only the Ni phase is shown. It is clear from Tables 3.2 and 3.3 that there is no significant difference between the phase fraction of Ni as compared to YSZ. The maximum standard deviation across

all cases was 4.5% of the mean value. The highest standard deviation occurred for the cases with the smallest domains, and were inversely related to the domain size. Two apparent sources of variation in the Ni and YSZ phase fractions are:

1. The variation in the number of particles within the system due to the packing algorithm.

2. The variation in the number of particles of comprising each phase.

We assume that the variation in the packing of particles is mainly due to particle interactions at the boundary, and we recognize that for this geometry (see Section 3.2.1) the ratio of boundary particles to interior particles is very close to

$$\frac{3 \cdot (L/r)^3}{14 \cdot (L/r)^2} = \frac{3}{14} \cdot \frac{r}{L} \ . \tag{3.5}$$

Assuming that the variation in the particle packing at the boundaries is uniform with respect to the total boundary area, we can expect the variation in the number of particles at the boundary to vary proportionally with $(L/r)^2$. The number of particles, N, is proportional to the the volume, $N \sim (L/r)^3$. Using the same assumptions, the standard deviation as a fraction of the mean, σ/μ, should be inversely proportional to L/r, $\sigma/\mu \sim r/L$. The data in Tables 3.4, A.1, and A.2 are not sufficient to confirm or disprove these trends; this indicates that a higher number of trials is needed to establish the validity of these relationships.

The variation in the number of particles comprising each phase is better understood. The distribution of Ni and YSZ particles is a binomial distribution with N and, for these cases, $p = 0.5$. The expected mean for both Ni and YSZ particles is $N/2$, and the expected standard deviation is .25 N [15]. As $N \sim (L/r)^3$, $\sigma_{N_{\mathrm{Ni}}}$ and $\sigma_{N_{\mathrm{YSZ}}}$ should vary as $(L/r)^3$. When the measured results are fitted with a power law trendline, however, the increase in $\sigma_{N_{\mathrm{Ni}}}$ and $\sigma_{N_{\mathrm{YSZ}}}$ with respect to N is less than $(L/r)^3$. The exponent

results for the power law trendlines are given in Table 3.1.

Table 3.1: Power law exponent for $\sigma_{N_{\mathrm{YSZ}}}$ as a function of λ

λ	Power Law Exponent
0.965	1.77
0.970	1.76
0.975	1.74
0.980	1.52
0.985	1.21
0.990	1.55
0.995	1.13

In all cases, σ/μ for the phase fractions is less than .05; for cases with $L/r \geq 24$, $\sigma/\mu \leq .0211$. This confirms that phase fractions are not significantly impacted by the choice of L/r.
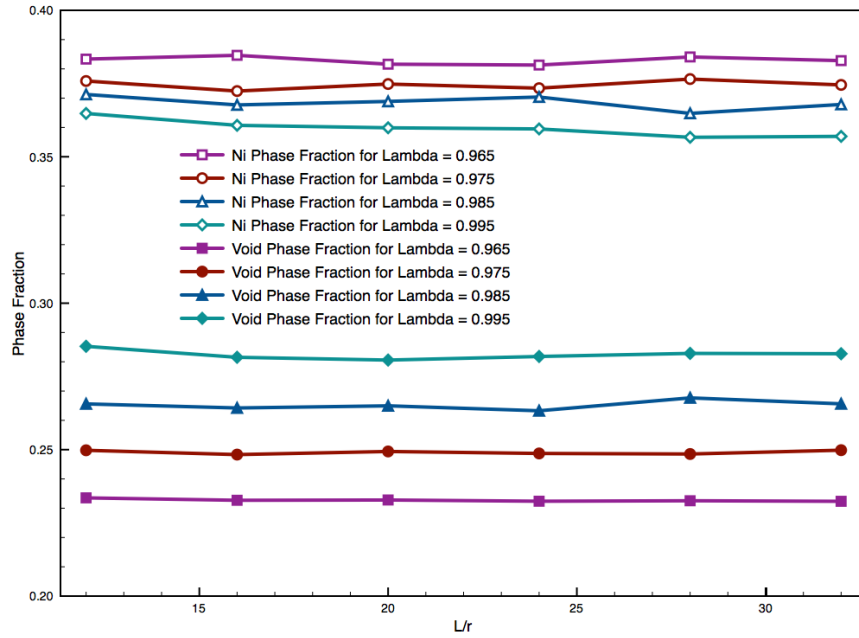
Figure 3.1: Mean phase fractions for systems of type A as a function of system size parameter, L/r

Phase fractions for systems of type B are presented graphically in Figures 3.3 and 3.4. Selected data is presented in Tables 3.5, 3.6, and 3.7, with the full data set available in

Table 3.2: Ni phase fraction and particle count for type A systems as a function of system size parameter, L/r

L/r	λ	Mean Nickel Phase Fraction	Standard Deviation	σ/μ	Mean Number of Nickel Particles	Standard Deviation	σ/μ
12	0.965	0.383	0.0110	2.88%	507	15.0	2.96%
16	0.965	0.385	0.00412	1.07%	1201	14.1	1.18%
20	0.965	0.382	0.00689	1.81%	2327	33.5	1.44%
24	0.965	0.381	0.00599	1.57%	3992	60.8	1.52%
28	0.965	0.384	0.00757	1.97%	6391	79.2	1.24%
32	0.965	0.383	0.00713	1.86%	9535	53.9	0.57%
12	0.975	0.376	0.0105	2.80%	492	13.0	2.64%
16	0.975	0.372	0.00670	1.80%	1152	17.9	1.55%
20	0.975	0.375	0.00725	1.93%	2268	30.2	1.33%
24	0.975	0.373	0.00632	1.69%	3894	46.7	1.20%
28	0.975	0.377	0.00569	1.51%	6181	51.6	0.84%
32	0.975	0.375	0.00671	1.79%	9221	70.0	0.76%
12	0.985	0.371	0.0138	3.71%	483	17.7	3.67%
16	0.985	0.368	0.00928	2.52%	1131	30.6	2.71%
20	0.985	0.369	0.00855	2.32%	2190	22.7	1.04%
24	0.985	0.370	0.00586	1.58%	3781	34.1	0.90%
28	0.985	0.365	0.00480	1.32%	6008	59.6	0.99%
32	0.985	0.368	0.00588	1.60%	8970	68.2	0.76%
12	0.995	0.365	0.0124	3.41%	471	13.7	2.91%
16	0.995	0.361	0.00987	2.74%	1100	22.3	2.03%
20	0.995	0.360	0.00673	1.87%	2136	18.8	0.88%
24	0.995	0.360	0.00554	1.54%	3689	32.2	0.87%
28	0.995	0.357	0.00508	1.42%	5805	30.2	0.52%
32	0.995	0.357	0.00460	1.29%	8633	46.2	0.54%

Table 3.3: YSZ phase fraction and particle count for type A systems as a function of system size parameter, L/r

L/r	λ	Mean YSZ Phase Fraction	Standard Deviation	σ/μ	Mean Number of YSZ Particles	Standard Deviation	σ/μ
12	0.965	0.383	0.0119	3.11%	510	16.7	3.27%
16	0.965	0.383	0.00629	1.64%	1197	14.0	1.17%
20	0.965	0.386	0.00593	1.54%	2352	33.6	1.43%
24	0.965	0.386	0.00449	1.16%	4069	61.3	1.51%
28	0.965	0.383	0.00694	1.81%	6391	76.6	1.20%
32	0.965	0.385	0.00646	1.68%	9526	58.6	0.62%
12	0.975	0.374	0.0107	2.86%	494	13.9	2.81%
16	0.975	0.379	0.00750	1.98%	1176	17.8	1.52%
20	0.975	0.376	0.00635	1.69%	2261	29.3	1.30%
24	0.975	0.378	0.00768	2.03%	3919	50.1	1.28%
28	0.975	0.375	0.00677	1.81%	6199	53.9	0.87%
32	0.975	0.376	0.00537	1.43%	9238	69.0	0.75%
12	0.985	0.363	0.0162	4.46%	473	19.5	4.14%
16	0.985	0.368	0.0110	3.00%	1125	30.4	2.70%
20	0.985	0.366	0.00662	1.81%	2198	20.3	0.92%
24	0.985	0.366	0.00593	1.62%	3790	38.4	1.01%
28	0.985	0.368	0.00421	1.15%	6000	55.3	0.92%
32	0.985	0.367	0.00533	1.46%	8927	67.2	0.75%
12	0.995	0.350	0.0114	3.25%	455	14.2	3.11%
16	0.995	0.358	0.00858	2.40%	1088	23.5	2.16%
20	0.995	0.360	0.00778	2.16%	2120	20.0	0.94%
24	0.995	0.359	0.00757	2.11%	3655	38.0	1.04%
28	0.995	0.361	0.00531	1.47%	5831	30.0	0.51%
32	0.995	0.360	0.00358	0.99%	8730	50.8	0.58%

Table 3.4: Void phase fraction and total particle count for type A systems as a function of system size parameter, L/r

L/r	λ	Mean Void Phase Fraction	Standard Deviation	σ/μ	Mean Number of Particles	Standard Deviation	σ/μ
12	0.965	0.234	0.00608	2.60%	1017	4.74	0.466%
16	0.965	0.233	0.00549	2.36%	2398	5.40	0.225%
20	0.965	0.233	0.00358	1.54%	4679	8.94	0.191%
24	0.965	0.232	0.00477	2.05%	8061	9.64	0.120%
28	0.965	0.233	0.00347	1.49%	12782	23.2	0.181%
32	0.965	0.232	0.00462	1.99%	19062	12.3	0.0643%
12	0.975	0.250	0.00345	1.38%	986	3.52	0.357%
16	0.975	0.248	0.00355	1.43%	2327	4.68	0.201%
20	0.975	0.249	0.00477	1.91%	4529	7.16	0.158%
24	0.975	0.249	0.00538	2.16%	7813	7.36	0.0943%
28	0.975	0.249	0.00239	0.96%	12380	12.4	0.100%
32	0.975	0.250	0.00364	1.46%	18459	16.5	0.0895%
12	0.985	0.266	0.00556	2.09%	955	4.73	0.495%
16	0.985	0.264	0.00527	1.99%	2256	4.98	0.221%
20	0.985	0.265	0.00342	1.29%	4388	5.02	0.114%
24	0.985	0.263	0.00523	1.99%	7571	8.80	0.116%
28	0.985	0.268	0.00461	1.72%	12009	6.22	0.0518%
32	0.985	0.266	0.00560	2.11%	17898	18.0	0.100%
12	0.995	0.285	0.00679	2.38%	926	4.84	0.523%
16	0.995	0.282	0.00411	1.46%	2188	3.75	0.172%
20	0.995	0.281	0.00503	1.79%	4255	7.69	0.181%
24	0.995	0.282	0.00532	1.89%	7344	10.0	0.137%
28	0.995	0.283	0.00385	1.36%	11636	11.0	0.0944%
32	0.995	0.283	0.00236	0.834%	17363	12.4	0.0712%

Tables A.13, A.14, A.15, A.16, A.17, and A.18 of Appendix A. The results for type B systems largely mirror the results for type A systems. One difference is the divergence in the variance of the phase fractions for Ni and YSZ. For type A systems the variance of the particle counts for YSZ particles, as well as the variance of phase fractions for Ni and YSZ, were similar. For the survey of type B systems, the standard deviation in the number of YSZ particles is about half of the standard deviation in the number of Ni particles. This discrepancy is due to the 48-bit pseudo-random number generator from the standard C++ library. The generator does provide a uniform distribution of values across its range, and this can be evaluated via the mean values of the particle types. However, as shown in Figure 3.2, the number of Ni particles for a single case varies across a larger range. For the cases in Figure 3.2 the mean number of Ni particles is 2911 versus 2900 for YSZ particles, a difference of only 0.40%. σ for the Ni samples is 50.5 versus 23.8 for YSZ particles, a factor of 2. We expect that the impact of this phenomenon will be to increase variability of the calculated properties.
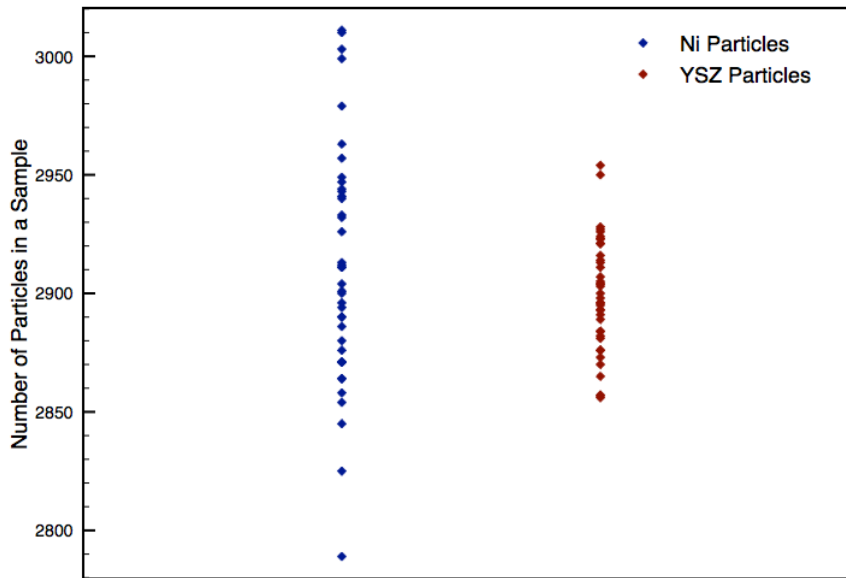
Figure 3.2: Number of particles created by type for 40 trials

Table 3.5: Ni phase fraction and particle count for type B systems as a function of system size parameter, L/r

L/r	λ	Mean Nickel Phase Fraction	Standard Deviation	σ/μ	Mean Number of Nickel Particles	Standard Deviation	σ/μ
12	0.965	0.245	0.00737	1.88%	683	13.8	1.88%
16	0.965	0.246	0.00633	1.82%	1605	41.0	1.82%
20	0.965	0.246	0.00628	1.21%	3142	47.1	1.21%
24	0.965	0.244	0.00510	1.08%	5392	67.9	1.08%
28	0.965	0.245	0.00554	1.15%	8532	73.3	1.15%
32	0.965	0.245	0.00467	1.11%	12820	126	1.11%
12	0.975	0.238	0.00725	1.77%	663	14.6	1.77%
16	0.975	0.240	0.00362	0.930%	1559	13.9	0.93%
20	0.975	0.242	0.00694	1.11%	3060	32.8	1.11%
24	0.975	0.240	0.00439	0.76%	5269	56.3	0.76%
28	0.975	0.240	0.00455	1.11%	8334	69.5	1.11%
32	0.975	0.239	0.00410	1.03%	12429	92.4	1.03%
12	0.985	0.238	0.0101	1.77%	653	20.0	1.77%
16	0.985	0.237	0.00764	1.56%	1522	37.7	1.56%
20	0.985	0.237	0.00726	1.29%	2980	59.9	1.29%
24	0.985	0.236	0.00477	0.85%	5127	47.7	0.85%
28	0.985	0.233	0.00417	0.87%	8083	101.5	0.87%
32	0.985	0.237	0.00412	0.96%	12078	79.7	0.96%
12	0.995	0.234	0.0116	3.24%	638	24.5	3.24%
16	0.995	0.231	0.00616	1.00%	1494	28.3	1.00%
20	0.995	0.231	0.00519	1.24%	2906	36.5	1.24%
24	0.995	0.232	0.00420	1.26%	5001	58.2	1.26%
28	0.995	0.232	0.00588	1.03%	7922	81.6	1.03%
32	0.995	0.232	0.00414	1.08%	11805	87.7	1.08%

Table 3.6: YSZ phase fraction and particle count for type B systems as a function of system size parameter, L/r

L/r	λ	Mean YSZ Phase Fraction	Standard Deviation	σ/μ	Mean Number of YSZ Particles	Standard Deviation	σ/μ
12	0.965	0.515	0.00966	1.88%	676	8.13	1.20%
16	0.965	0.517	0.00941	1.82%	1599	19.9	1.25%
20	0.965	0.514	0.00620	1.21%	3108	21.5	0.692%
24	0.965	0.518	0.00561	1.08%	5375	29.6	0.550%
28	0.965	0.517	0.00592	1.15%	8543	32.1	0.375%
32	0.965	0.517	0.00576	1.11%	12693	59.4	0.468%
12	0.975	0.510	0.00903	1.77%	662	7.09	1.07%
16	0.975	0.506	0.00472	0.93%	1561	8.25	0.529%
20	0.975	0.505	0.00562	1.11%	3031	15.1	0.497%
24	0.975	0.509	0.00384	0.76%	5234	26.8	0.512%
28	0.975	0.506	0.00559	1.11%	8302	34.6	0.417%
32	0.975	0.509	0.00524	1.03%	12392	44.6	0.360%
12	0.985	0.496	0.00879	1.77%	640	9.49	1.48%
16	0.985	0.495	0.00770	1.56%	1517	17.1	1.13%
20	0.985	0.496	0.00638	1.29%	2955	31.5	1.07%
24	0.985	0.500	0.00423	0.85%	5103	21.0	0.412%
28	0.985	0.499	0.00433	0.87%	8107	48.9	0.604%
32	0.985	0.496	0.00478	0.96%	12088	46.0	0.380%
12	0.995	0.482	0.0156	3.24%	623	11.2	1.79%
16	0.995	0.488	0.00488	1.00%	1479	15.8	1.07%
20	0.995	0.487	0.00604	1.24%	2881	19.9	0.691%
24	0.995	0.488	0.00617	1.26%	4971	28.3	0.568%
28	0.995	0.488	0.00501	1.03%	7883	39.3	0.499%
32	0.995	0.489	0.00530	1.08%	11767	41.4	0.352%

Table 3.7: Void phase fraction and particle count for type B systems as a function of system size parameter, L/r

L/r	λ	Mean Void Phase Fraction	Standard Deviation	σ/μ	Mean Number of Particles	Standard Deviation	σ/μ
LoR	Overlap	Void Fraction			Num Particles		
12	0.965	0.240	0.00420	1.75%	1359	7.13	0.525%
16	0.965	0.237	0.00593	2.50%	3204	21.7	0.677%
20	0.965	0.241	0.00576	2.39%	6250	26.8	0.429%
24	0.965	0.237	0.00451	1.90%	10767	40.1	0.372%
28	0.965	0.239	0.00367	1.54%	17076	42.9	0.251%
32	0.965	0.238	0.00276	1.16%	25513	69.6	0.273%
12	0.975	0.252	0.00502	1.99%	1324	8.78	0.663%
16	0.975	0.253	0.00478	1.89%	3120	11.2	0.360%
20	0.975	0.254	0.00538	2.12%	6091	20.6	0.338%
24	0.975	0.252	0.00251	1.00%	10503	32.6	0.311%
28	0.975	0.254	0.00321	1.26%	16636	39.3	0.236%
32	0.975	0.252	0.00469	1.86%	24822	50.3	0.203%
12	0.985	0.266	0.00652	2.45%	1293	12.3	0.953%
16	0.985	0.268	0.00386	1.44%	3039	21.2	0.697%
20	0.985	0.267	0.00443	1.66%	5935	30.8	0.519%
24	0.985	0.265	0.00339	1.28%	10229	28.7	0.281%
28	0.985	0.268	0.00411	1.53%	16190	53.5	0.330%
32	0.985	0.267	0.00505	1.89%	24166	37.4	0.155%
12	0.995	0.284	0.00799	2.81%	1260	13.9	1.10%
16	0.995	0.281	0.00368	1.31%	2973	17.6	0.591%
20	0.995	0.282	0.00506	1.79%	5787	18.7	0.323%
24	0.995	0.281	0.00500	1.78%	9972	31.5	0.316%
28	0.995	0.280	0.00387	1.38%	15805	46.0	0.291%
32	0.995	0.280	0.00557	1.99%	23571	50.1	0.212%

Figure 3.3: Ni and YSZ phase fractions for systems of type B as a function of system size parameter, L/r

3.2.1.2 Coordination Numbers

The next set of parameters are the particle coordination numbers, Z_i, of the system. If the boundary conditions of the system are periodic in all three dimensions, the coordination numbers are independent of the size of the system. This can be understood in terms of a system consisting of a regular array of spheres in a simple cubic configuration. For an infinite cubic array the coordination number is exactly 6. This result is also true for a finite cubic domain with periodic boundaries where the size of the domain is an integer multiple of the diameter, as in equation 3.6.

$$L = 2nr, n \in 1, 2, 3, ... \tag{3.6}$$

If the array is periodic in only two dimensions, the coordination number depends on L. If the domain length, L, is twelve times the sphere diameter, $12r$, the coordination
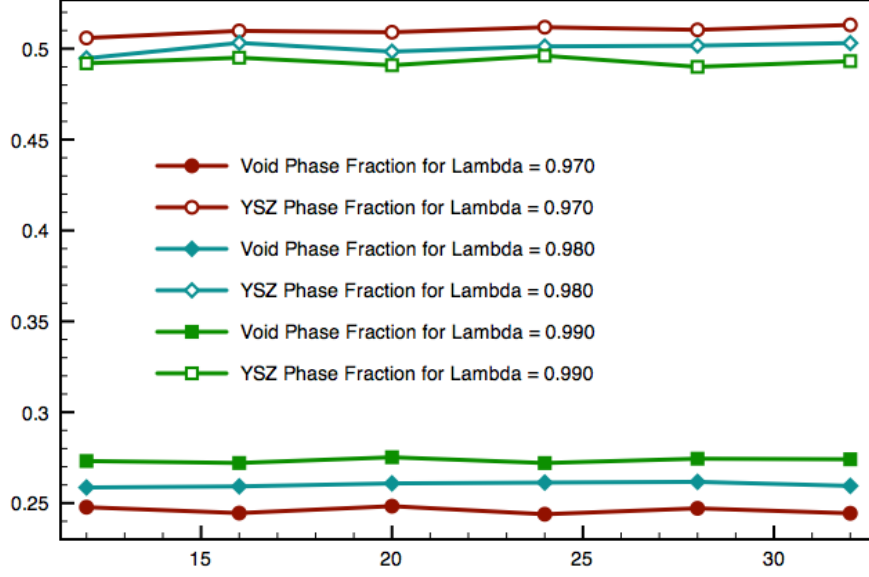
Figure 3.4: Mean phase fractions for systems of type B as a function of system size parameter, L/r

number, Z is $5.3\bar{3}$. Increasing L to $24r$ increases Z to $5.6\bar{6}$. The particles within the array which are not in contact with the non-periodic boundary have a coordination number of 6. The particles at the non-periodic boundaries have a coordination number of 5. Z is the average of all coordination numbers. There are $L/2r$ layers within the array, and $(L/2r)^2$ within each layer of the array. The total number of particles in the system is $(L/2r)^3$. For the general case the coordination number for the system is

$$Z = \frac{6\left[(\frac{L}{2r} - 2) \cdot \left(\frac{L}{2r}\right)^2\right] + 5 \cdot 2 \cdot \left(\frac{L}{2r}\right)^2}{\left(\frac{L}{2r}\right)^3} \ , \tag{3.7}$$

which can be simplified to

$$Z = 6 - 4 \cdot \frac{r}{L} \ . \tag{3.8}$$

For this relation $Z \to 6$ as $L \to \infty$. The systems being evaluated here are neither infinite

in extent nor periodic along all three boundaries, so we must inquire: How large does L/r need to be in order to minimize the impact of boundary effects on the coordination numbers? Equations 3.7 and 3.8 demonstrate that the difference between Z_i for the infinite case and the finite case is proportional to the fraction of particles in contact with the non-periodic boundary. The exact numerical relationship will be different for packings that are not simple cubic, but the final result will have the form of

$$Z = a - b \cdot \frac{r}{L} \tag{3.9}$$

with a and b being determined by the domain, boundary conditions, and particle packing geometry.

The systems we are using are periodic in the x and y dimensions, but not in the z dimension. In particular, the domain is $L_x = L_y = L_z/3$. The coordination numbers for various values of the L/r parameter are shown in Tables 3.8, 3.9, 3.10, and 3.11. The parameters detailed in the tables are as follows:

1. Z is the average coordination number for all particles.

2. Z_{YSZ} is the average coordination number for YSZ particles.

3. Z_{Ni} is the average coordination number for Ni particles.

4. $Z_{\text{YSZ}-\text{YSZ}}$ is the average coordination number for YSZ particles with respect to YSZ particles.

5. $Z_{\text{Ni}-\text{Ni}}$ is the average coordination number for Ni particles with respect to Ni particles.

Z_i is used to refer collectively to all of the above coordination numbers.

For systems of type A and type B, the coordination numbers increase as L/r increases. The increase in Z_i is inversely proportional to L/r. From this we can derive that the

expected difference in Z from $L/r = 24$ to $L/r = 1000$ is greater than to the expected difference in Z from $L/r = 2$ to $L/r = 24$. From the values listed in Tables 3.8, 3.9, 3.10, and 3.11, a system size of $L/r = 24$ results in coordination numbers within 1% of that for $L/r = 1000$, and at a much lower computational cost.

Table 3.8: Z and Z_{Ni} for type A systems as a function of system size parameter, L/r

L/r	λ	Z	σ_Z	σ/μ	Z_{Ni}	$\sigma_{Z_{\mathrm{Ni}}}$	σ/μ
12	0.965	8.12	0.0724	0.89%	8.11	0.0571	0.70%
16	0.965	8.15	0.0391	0.48%	8.15	0.0466	0.57%
20	0.965	8.18	0.0232	0.28%	8.19	0.0215	0.26%
24	0.965	8.19	0.023	0.28%	8.17	0.0272	0.33%
28	0.965	8.2	0.0199	0.24%	8.2	0.0184	0.22%
32	0.965	8.21	0.0138	0.17%	8.21	0.0158	0.19%
12	0.975	7.92	0.0542	0.68%	7.93	0.0716	0.90%
16	0.975	7.96	0.0262	0.33%	7.96	0.0399	0.50%
20	0.975	7.99	0.0225	0.28%	7.98	0.0221	0.28%
24	0.975	8	0.0199	0.25%	7.99	0.0267	0.33%
28	0.975	8	0.0198	0.25%	8	0.0233	0.29%
32	0.975	8.02	0.0114	0.14%	8.02	0.0138	0.17%
12	0.985	7.69	0.0375	0.49%	7.67	0.0356	0.46%
16	0.985	7.75	0.029	0.37%	7.75	0.0337	0.43%
20	0.985	7.78	0.0225	0.29%	7.78	0.0278	0.36%
24	0.985	7.8	0.0135	0.17%	7.8	0.0236	0.30%
28	0.985	7.82	0.0108	0.14%	7.81	0.014	0.18%
32	0.985	7.81	0.0163	0.21%	7.81	0.0192	0.25%
12	0.995	7.49	0.0594	0.79%	7.47	0.0734	0.98%
16	0.995	7.54	0.0316	0.42%	7.53	0.0345	0.46%
20	0.995	7.56	0.0174	0.23%	7.55	0.0262	0.35%
24	0.995	7.58	0.024	0.32%	7.57	0.0293	0.39%
28	0.995	7.59	0.0147	0.19%	7.59	0.0179	0.24%
32	0.995	7.6	0.0101	0.13%	7.6	0.0146	0.19%

In all cases for $L/r \geq 20$, the mean value of Z_i varied by less than 1% from the value for the largest case considered, $L/r = 40$. For the cases of type A σ_Z varied between 0.89% and 0.13% of μ_Z. The largest values of σ_Z occurred at $L/r = 12$. There was a greater variation in the coordination numbers between like particles, Z_{i-i} and Z_{e-e} than for Z. σ is inversely related to L and varies from 4.46% of the mean to 0.57% of the mean. For the cases of type B the variation in Z was similar to the type A cases with σ_Z varying from 0.77% to 0.09% of μ_Z. $\sigma_{Z_{i-i}}$ and $\sigma_{Z_{e-e}}$ are in a similar range, varying between 4.56% and 0.24% of the mean value. σ_{Z_i} of the the smaller Ni particles

Table 3.9: $Z_{\text{YSZ}-\text{YSZ}}$ and $Z_{\text{Ni}-\text{Ni}}$ for type A systems as a function of system size parameter, L/r

L/r	λ	$Z_{\text{YSZ}-\text{YSZ}}$	$\sigma_{Z_{\text{YSZ}-\text{YSZ}}}$	σ/μ	$Z_{\text{Ni}-\text{Ni}}$	$\sigma_{Z_{\text{Ni}-\text{Ni}}}$	σ/μ
12	0.965	4.07	0.149	3.66%	4.04	0.121	3.00%
16	0.965	4.06	0.0962	2.37%	4.07	0.0707	1.74%
20	0.965	4.11	0.0766	1.86%	4.07	0.0576	1.42%
24	0.965	4.15	0.0645	1.55%	4.04	0.0768	1.90%
28	0.965	4.11	0.048	1.17%	4.1	0.0564	1.38%
32	0.965	4.1	0.027	0.66%	4.1	0.026	0.64%
12	0.975	3.97	0.155	3.91%	3.97	0.0866	2.18%
16	0.975	4.05	0.0859	2.12%	3.97	0.0585	1.48%
20	0.975	3.98	0.0561	1.41%	3.98	0.0655	1.64%
24	0.975	4.01	0.0576	1.44%	3.98	0.061	1.54%
28	0.975	4.01	0.055	1.37%	3.99	0.0306	0.77%
32	0.975	4.02	0.0309	0.77%	4.01	0.0393	0.98%
12	0.985	3.83	0.158	4.11%	3.86	0.172	4.46%
16	0.985	3.87	0.119	3.07%	3.88	0.0977	2.52%
20	0.985	3.91	0.0464	1.18%	3.9	0.0487	1.25%
24	0.985	3.9	0.0364	0.93%	3.9	0.04	1.03%
28	0.985	3.92	0.0338	0.86%	3.91	0.043	1.10%
32	0.985	3.9	0.0325	0.83%	3.92	0.0286	0.73%
12	0.995	3.69	0.11	2.99%	3.79	0.126	3.32%
16	0.995	3.74	0.109	2.92%	3.77	0.0677	1.80%
20	0.995	3.75	0.0501	1.33%	3.77	0.0426	1.13%
24	0.995	3.77	0.0488	1.30%	3.79	0.0248	0.66%
28	0.995	3.8	0.0308	0.81%	3.79	0.0278	0.73%
32	0.995	3.82	0.0394	1.03%	3.78	0.0276	0.73%

Table 3.10: Z, $Z_{\mathrm{YSZ-YSZ}}$, and $Z_{\mathrm{Ni-Ni}}$ for type B systems as a function of system size parameter, L/r

L/r	λ	Z	σ_Z	σ/μ	$Z_{\mathrm{YSZ-YSZ}}$	$\sigma_{Z_{\mathrm{YSZ-YSZ}}}$	σ/μ	$Z_{\mathrm{Ni-Ni}}$	$\sigma_{Z_{\mathrm{Ni-Ni}}}$	σ/μ
12	0.965	7.97	0.0617	0.77%	5.12	0.0916	1.79%	3.04	0.0679	2.23%
16	0.965	8.02	0.018	0.23%	5.18	0.0847	1.63%	3.1	0.0585	1.89%
20	0.965	8.05	0.0134	0.17%	5.18	0.0529	1.02%	3.11	0.0597	1.92%
24	0.965	8.06	0.0165	0.21%	5.21	0.0385	0.74%	3.09	0.0429	1.39%
28	0.965	8.08	0.0102	0.13%	5.23	0.029	0.56%	3.09	0.0267	0.86%
32	0.965	8.08	0.0154	0.19%	5.22	0.0261	0.50%	3.12	0.036	1.15%
12	0.975	7.82	0.0475	0.61%	5.04	0.0866	1.72%	2.99	0.0679	2.27%
16	0.975	7.87	0.0353	0.45%	5.05	0.0551	1.09%	3.01	0.0657	2.18%
20	0.975	7.89	0.025	0.32%	5.06	0.0454	0.90%	3.01	0.0572	1.90%
24	0.975	7.91	0.0213	0.27%	5.09	0.0282	0.55%	3.04	0.035	1.15%
28	0.975	7.91	0.0157	0.20%	5.09	0.0301	0.59%	3.03	0.0226	0.75%
32	0.975	7.92	0.0072	0.09%	5.1	0.0277	0.54%	3.03	0.0208	0.69%
12	0.985	7.65	0.0483	0.63%	4.85	0.0825	1.70%	2.91	0.0858	2.95%
16	0.985	7.69	0.0354	0.46%	4.92	0.0598	1.21%	2.93	0.0883	3.01%
20	0.985	7.73	0.0243	0.31%	4.95	0.0507	1.02%	2.96	0.0739	2.50%
24	0.985	7.74	0.0124	0.16%	4.94	0.0415	0.84%	2.93	0.0258	0.88%
28	0.985	7.74	0.0096	0.12%	4.97	0.0309	0.62%	2.94	0.0396	1.35%
32	0.985	7.75	0.0095	0.12%	4.97	0.0153	0.31%	2.94	0.03	1.02%
12	0.995	7.48	0.0331	0.44%	4.71	0.115	2.43%	2.83	0.0959	3.38%
16	0.995	7.53	0.0337	0.45%	4.8	0.0845	1.76%	2.87	0.0687	2.39%
20	0.995	7.55	0.0237	0.31%	4.78	0.0401	0.84%	2.87	0.0489	1.71%
24	0.995	7.56	0.0097	0.13%	4.81	0.0405	0.84%	2.87	0.0307	1.07%
28	0.995	7.56	0.0103	0.14%	4.81	0.0281	0.58%	2.88	0.0324	1.12%
32	0.995	7.57	0.0088	0.12%	4.81	0.0209	0.44%	2.86	0.0235	0.82%

Table 3.11: Coordination number for system of type B distribution and $\lambda = 0.965$ for systems as a function of system size parameter, L/r

L/r	Z	$Z_{\mathrm{YSZ-YSZ}}$	$Z_{\mathrm{Ni-Ni}}$	Z_{Ni}	Z_{YSZ}
12	7.97	5.12	3.04	9.03	6.92
16	8.02	5.18	3.10	9.07	6.97
20	8.05	5.18	3.11	9.11	7.00
24	8.06	5.21	3.09	9.12	7.00
28	8.08	5.23	3.09	9.14	7.02
32	8.08	5.22	3.12	9.15	7.02
40	8.09	5.22	3.12	9.16	7.03

was greater than σ_{Z_i} for the larger YSZ particles in all cases.

3.2.1.3 Conductivity

The final parameters to be considered are conductivity and percolation. Percolation will be discussed in detail in Section 3.2.2. Selected data for the conductivity of type A systems is shown in Figures 3.5 and 3.6, and Table 3.12. The full data set is available in Tables A.11 and A.12. The variation in the reduced conductivity is significant, especially for cases with small L/r. For this reason, $\pm\sigma$ error bars are included in Figures 3.5, and 3.6. In Figures 3.5, 3.6, 3.7, and 3.8, the proportional conductivity is defined as the conductivity calculated in the z direction, divided by the conductivity in the z direction, of a cube of the same material (Ni or YSZ) of dimension $L_x \times L_y \times L_z$.

For the type A systems, the variation in conductivity is a very strong function of system size. The cases with $L/r \geq 24$ are within 6% of the results at $L/r = 40$. For $L/r = 12$ the σ/μ varies from 14% to 31.3%, with no discernible relationship between σ and λ. This variability declines with increasing L/r such that at $L/r = 40$ the σ/μ ranges from 5.5% to 2.5%. While this is the expected trend of decreasing variability with increasing domain size, the variation is not smooth.

For type B system distributions there is a similar pattern. The particle size ratio for type B systems is 1:0.781, with the smaller particles being assigned to the Ni phase. Selected data for the conductivity of type B systems is shown in Figures 3.7 and 3.8, and Table 3.13. The full data set is in Tables A.21 and A.22. For the Ni phase the variation was larger than for the type A systems. The value of σ varies from 34.2% to 73.3% of the mean for systems with $L/r = 12$, declining to a range of 9.34% to 13.9% for a system with $L/r = 40$. There was significantly less variation in the conduction of the phase consisting of the larger particles. For $L/r = 40$, the standard deviation varies from 6.37% to 12.5% of the mean. At $L/r = 12$, the standard deviation varies from

Table 3.12: Reduced conductivity for type A systems as a function of system size parameter, L/r

L/r	λ	Reduced Conductivity of Ni Phase	σ	σ/μ	Reduced Conductivity of YSZ Phase	σ	σ/μ
12	0.965	0.0293	0.00472	16.1%	0.0323	0.00699	21.7%
16	0.965	0.0345	0.00335	9.70%	0.0324	0.00360	11.1%
20	0.965	0.0338	0.00173	5.12%	0.0357	0.00314	8.81%
24	0.965	0.0340	0.00286	8.41%	0.0374	0.00241	6.45%
28	0.965	0.0353	0.00215	6.08%	0.0357	0.00215	6.01%
32	0.965	0.0357	0.00116	3.25%	0.0360	0.00126	3.50%
12	0.975	0.0260	0.00430	16.5%	0.0281	0.00437	15.5%
16	0.975	0.0274	0.00328	12.0%	0.0291	0.00242	8.34%
20	0.975	0.0290	0.00233	8.03%	0.0286	0.00239	8.38%
24	0.975	0.0281	0.00199	7.08%	0.0295	0.00251	8.51%
28	0.975	0.0298	0.00115	3.85%	0.0303	0.00162	5.34%
32	0.975	0.0299	0.00104	3.48%	0.0307	0.00112	3.64%
12	0.985	0.0228	0.00319	14.0%	0.0201	0.00393	19.5%
16	0.985	0.0233	0.00347	14.9%	0.0228	0.00307	13.4%
20	0.985	0.0236	0.00200	8.46%	0.0233	0.00178	7.61%
24	0.985	0.0246	0.00133	5.39%	0.0240	0.00138	5.74%
28	0.985	0.0250	0.00111	4.46%	0.0245	0.00097	3.96%
32	0.985	0.0249	0.00093	3.72%	0.0244	0.00111	4.54%
12	0.995	0.0184	0.00481	26.1%	0.0156	0.00282	18.1%
16	0.995	0.0188	0.00195	10.4%	0.0179	0.00194	10.8%
20	0.995	0.0187	0.00194	10.3%	0.0184	0.00122	6.65%
24	0.995	0.0190	0.00108	5.68%	0.0188	0.00093	4.91%
28	0.995	0.0191	0.00087	4.59%	0.0196	0.00114	5.82%
32	0.995	0.0188	0.00103	5.46%	0.0198	0.00089	4.48%

Figure 3.5: Reduced conductivity of Ni phase for systems of type A as a function of system size parameter, L/r

1.35% to 2.73% of the mean.

An important consideration is the computation time required to generate and solve the system. Figure 3.9 shows that the domain generation time increases nearly exponentially with the size of the domain over the range of interest. In order to calculate a statistically meaningful number of results, it is necessary to compromise on the size of the calculated domains versus the desire to minimize boundary effects from the calculations. We use domains with L_x and L_y satisfying $L/r \geq 24$ and $L_z = 3L_x$ for all calculations. The generation of the domain is the limiting factor for calculation time. The time to solve the potential across the domain, as well as the conductivity of the domain, is significantly shorter than the domain generation time, and, consequently, does not impact this decision. In Sections 3.2.1.1, 3.2.1.2, and 3.2.1.3 we demonstrated that using domains where $L/r = 24$ captures the qualitative relationships between different configurations; the results are close to the results that would be obtained from larger

Table 3.13: Conductivity for type B systems as a function of system size parameter, L/r

L/r	λ	Reduced Conductivity of Ni Phase	σ	σ/μ	Reduced Conductivity of YSZ Phase	σ	σ/μ
12	0.965	0.00130	0.000446	34.2%	0.0110	0.001376	12.5%
16	0.965	0.000945	0.000375	39.6%	0.0109	0.000737	6.74%
20	0.965	0.00110	0.000293	26.7%	0.0106	0.000631	5.96%
24	0.965	0.000869	0.000176	20.3%	0.0103	0.000395	3.85%
28	0.965	0.000902	0.000117	13.0%	0.00989	0.000339	3.43%
32	0.965	0.000925	0.0000956	10.3%	0.00997	0.000159	1.59%
36	0.965	0.000861	0.0000873	10.1%	0.00993	0.000180	1.81%
40	0.965	0.000822	0.0000823	10.0%	0.00993	0.000166	1.67%
12	0.975	0.00110	0.000448	40.7%	0.00951	0.001290	13.6%
16	0.975	0.000935	0.000184	19.7%	0.00912	0.000561	6.15%
20	0.975	0.000773	0.000227	29.4%	0.00908	0.000390	4.30%
24	0.975	0.000677	0.000096	14.2%	0.00868	0.000323	3.72%
28	0.975	0.000680	0.000139	20.5%	0.00865	0.000289	3.34%
32	0.975	0.000729	0.000113	15.5%	0.00852	0.000249	2.92%
36	0.975	0.000708	0.0000727	10.3%	0.00843	0.000208	2.47%
40	0.975	0.000641	0.0000599	9.34%	0.00830	0.000151	1.82%
12	0.985	0.000592	0.000434	73.3%	0.00841	0.000536	6.37%
16	0.985	0.000775	0.000258	33.3%	0.00754	0.000645	8.55%
20	0.985	0.000667	0.000181	27.1%	0.00730	0.000450	6.16%
24	0.985	0.000651	0.000200	30.7%	0.00716	0.000469	6.54%
28	0.985	0.000541	0.000083	15.4%	0.00702	0.000224	3.20%
32	0.985	0.000558	0.000121	21.7%	0.00706	0.000222	3.15%
36	0.985	0.000547	0.0000449	8.20%	0.00707	0.000158	2.23%
40	0.985	0.000513	0.0000596	11.6%	0.00690	0.000093	1.35%
12	0.995	0.000551	0.000234	42.4%	0.00694	0.000863	12.4%
16	0.995	0.000528	0.000148	28.0%	0.00602	0.000655	10.9%
20	0.995	0.000520	0.000133	25.6%	0.00588	0.000236	4.02%
24	0.995	0.000472	0.000163	34.5%	0.00570	0.000438	7.69%
28	0.995	0.000428	0.0000527	12.3%	0.00576	0.000227	3.93%
32	0.995	0.000444	0.0000693	15.6%	0.00560	0.000164	2.93%
36	0.995	0.000394	0.0000629	16.0%	0.00562	0.000178	3.18%
40	0.995	0.000420	0.0000586	13.9%	0.00553	0.000151	2.73%

Figure 3.6: Reduced conductivity of YSZ phase for systems of type A as a function of system size parameter, L/r

but computationally impractical values of L/r. The choice of $L/r = 24$ allows for a large number of cases to calculated within a reasonable time frame.

3.2.2 Percolation

Percolation and conductivity are closely related. The details of calculating conductivity are presented in Sections 2.2.2.2 and 2.2.2.3. Percolation is a precondition for conductivity, and the conductivity of an unpercolated network is identically zero. Percolation is defined here in terms of two parallel planar boundaries of a system. A system is percolated for a conducting phase if there exists a conduction path from one boundary of the system to another parallel boundary. This can be restated in terms of the conductivity of a system. For a system where a conducting phase has zero resistivity, the system is percolated if the conductivity is non-zero. The occurrence of percolation is a function of the geometry of the conducting phase. Percolation is a Boolean property;
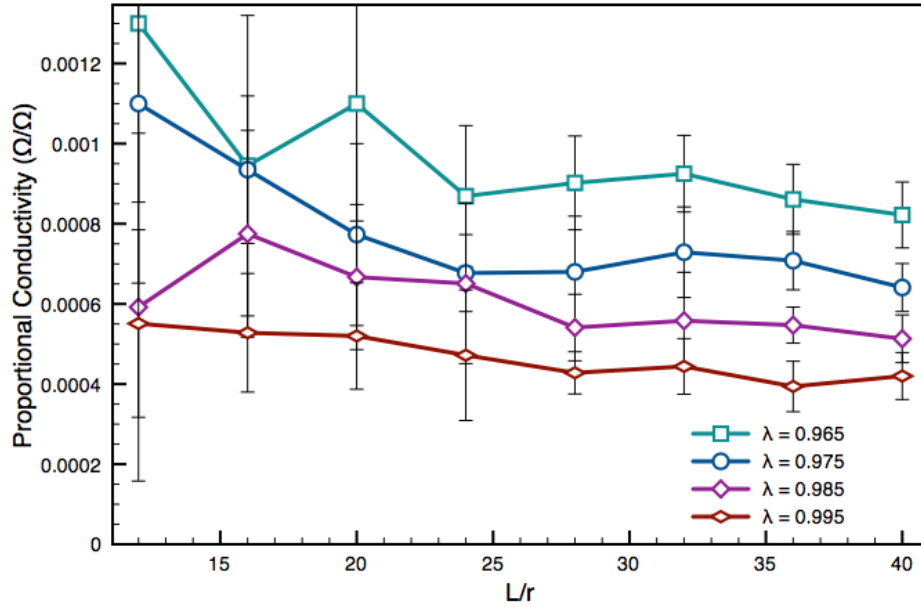
Figure 3.7: Reduced conductivity of Ni phase for systems of type B as a function of system size parameter, L/r

one useful measure is the probability, P_p, of percolation occurring for a particular type of system.

The percolation characteristics and conductivity characteristics of monodispersed particle arrays have been studied extensively. There are two sets of well-defined expected results which can be used to determine the accuracy of the model:

1. percolation threshold,

2. phase conductivity.

3.2.2.1   Percolation Threshold for Periodic Simple Cubic System

What is the actual process that precedes from the non-percolation state to the percolating state? A way to gain understanding of the behavior of these systems near the
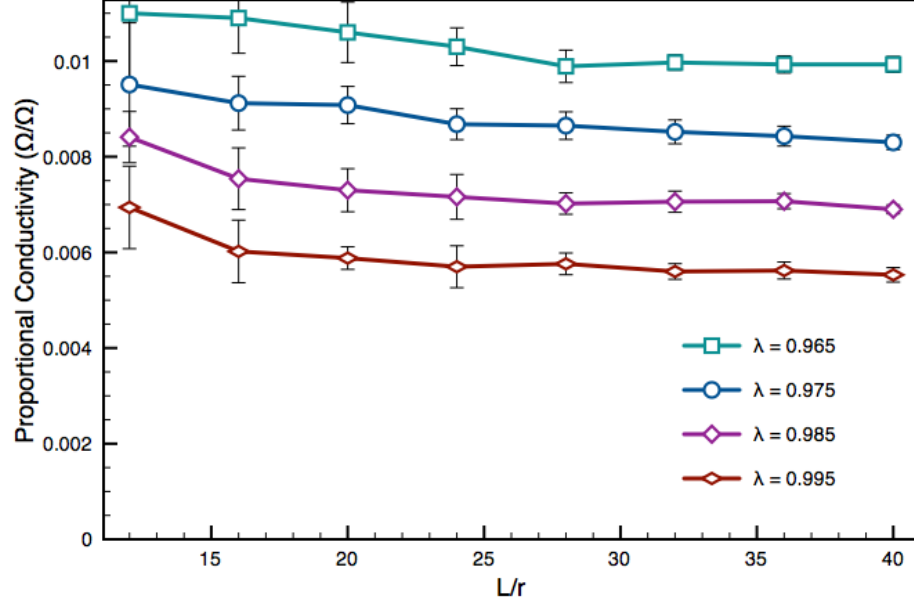
Figure 3.8: Reduced conductivity of YSZ for systems of type B as a function of system size parameter, L/r

percolation threshold is to examine a simplified system, a cubic array of spheres. The dimensions of the system will be small, $L/r = 6$, and the particle placement will be simple cubic as opposed to the random close packing. The center-to-center particle spacing will be $1.15r$. The consequence of this choice is that each particle will be in contact with 26 nearest neighbors. This system will have 27 particles, and it is possible to fully calculate every possible state. If we do not label specific particles, let n_1 represent the number of conducting particles within the system of type 1, and n_2 represent the number of non-conducting particles within the system of type 2. This system has periodic boundary conditions in the x and y directions. Percolation of the n_1 phase, in the z direction, occurs if and only if there is an n_1 type particle in each vertical layer of the structure.

$$\frac{27!}{n_1!(n_1 - n_2)!} \tag{3.10}$$
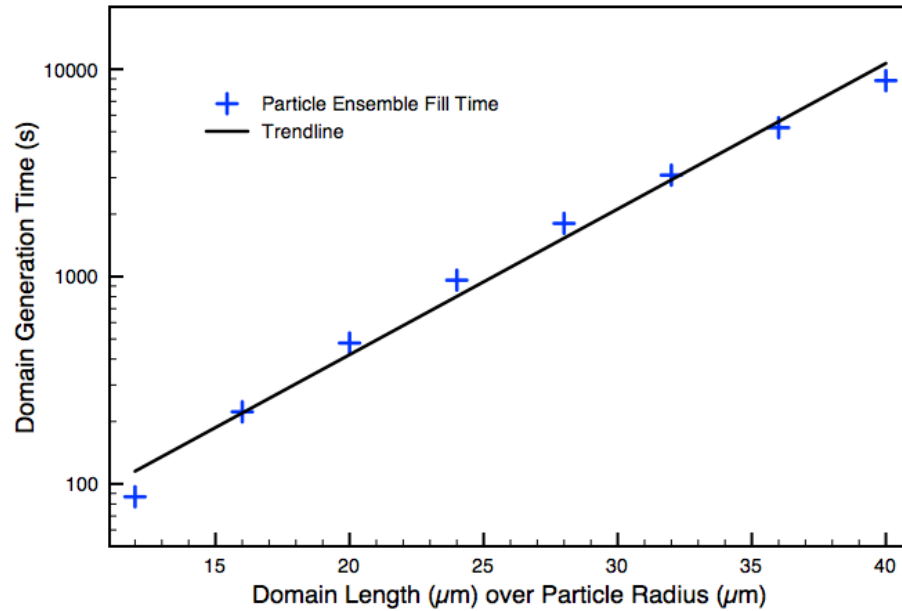
Figure 3.9: Time required to generate and solve particle systems as a function of system size parameter, L/r

As n_1 varies, the model undergoes transitions between 3 distinct phases, which are analogous to behavior which can be seen in random close packed models.

1. $n_1 < 3 \Rightarrow p = 0$. There is no percolation for any configuration. Examples with $n_1 = 2$ are shown in Figure 3.10.
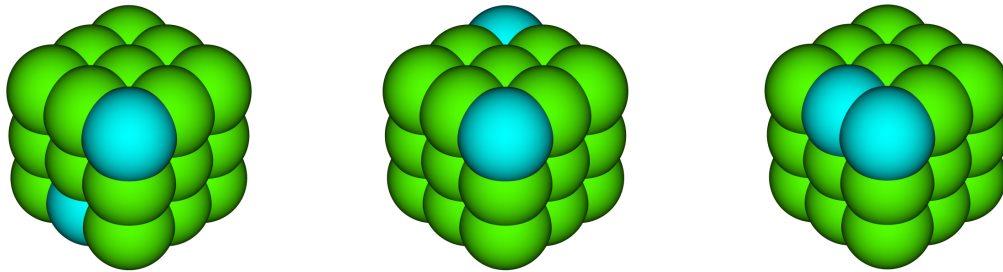
Figure 3.10: Three cases for a 3 X 3 X 3 particle ensemble with two particles of type n_1 and no percolation

2. $3 \leq n_1 \leq 18$: $\Rightarrow 0 < P_p < 1$. Percolation is possible. p is an increasing function

of n_1, but the increase in the percolation probability decreases as n_1 increases. For this system, because of the overlap and the periodic boundary conditions in x and y, the system will percolate for any case in which there is at least 1 n_1 type particle within each z-layer of the the structure. Three percolating examples with $n_1 = 3$ are shown in Figure 3.11.
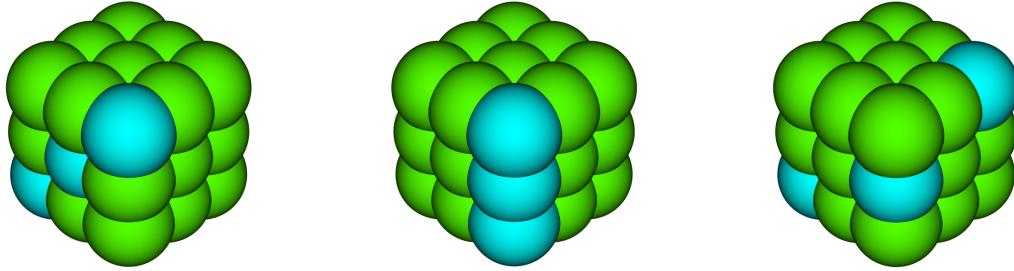
Figure 3.11: Three out of 243 cases with percolation for a 3 X 3 X 3 particle ensemble with three particles of type n_1

In Figure 3.12 the three possible configurations for $n_1 = 18$ for which percolation does not occur are shown.

3. $n_1 > 18 \Rightarrow p = 1$. Percolation is guaranteed for every possible configuration.

The initial jump in Figure 3.14 from $P_p(n_1 = 2)$ to $P_p(n_1 = 3)$ is .249, and P_p is > .9 for $n_1 = 8$. The full statistics for this system are given below in Table 3.14; Figure 3.14 shows P_p as a function of n_1. The calculation of these values are a straightforward exercise in combinations. The percolation probability is the number of percolating cases
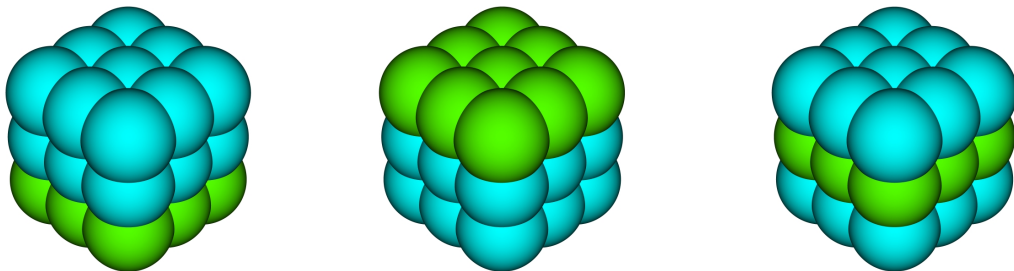
Figure 3.12: The three cases without percolation for a 3 X 3 X 3 particle ensemble with 18 particles of type n_1
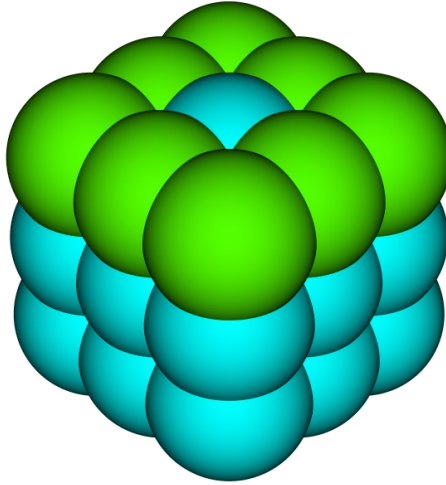
Figure 3.13: One out of 27 cases with percolation for a 3 X 3 X 3 particle ensemble with 19 particles of type n_1. Note that there is no non-percolating case for $n_1 \geq 19$

divided by total number of cases for value of n_1.

Details of these combinatorial calculations can be found in most elementary probability and statistics texts, such as those written by Ross [40] or Devore [15]. For each value of n_1 the number of cases is:

$$\frac{27!}{n_1!(27 - n_1)!} \ .$$

(3.11)

In order to calculate the number of percolating cases for $3 \leq n_1 \leq 18$, two combinatorial calculations must be combined. Percolation occurs when there is at least one n_1 type particle in each layer. The first calculation determines how many ways the n_1 particles can be separated into 3 non-empty groups, where the order of the groups does not matter. For each of these combinations the total number of geometrical configurations must be calculated. The total number of configurations is the product of the number of configurations for each of the 3 groups. The number of configurations for one group where n is the number of n_1 particles in that group is

$$\frac{9!}{n!(9 - n)!} \ .$$

(3.12)
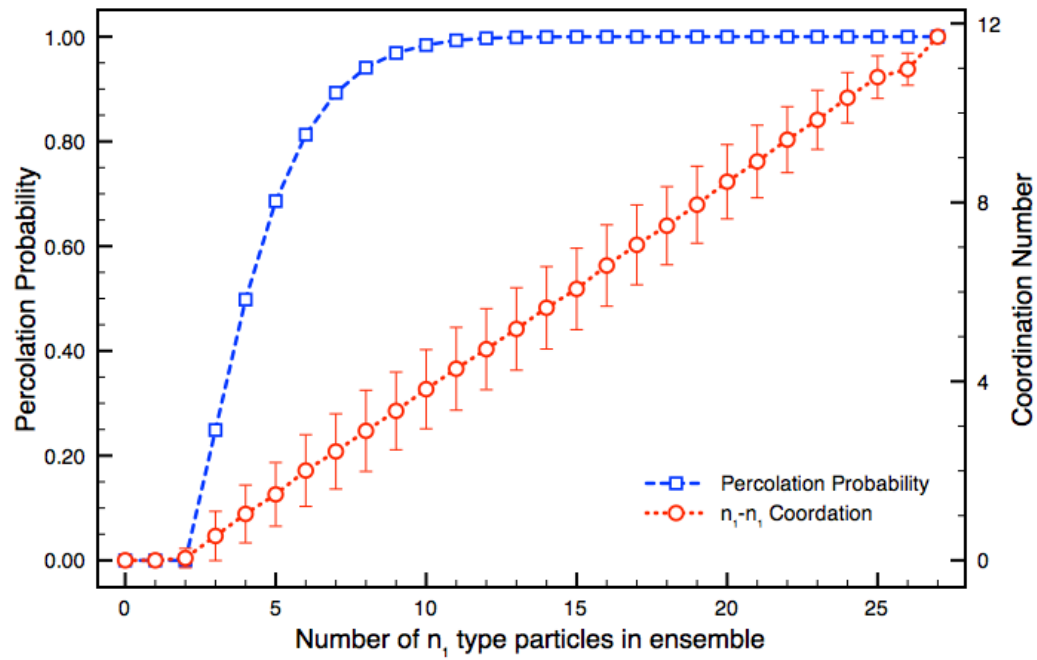
Figure 3.14: Percolation probability, P_p, and $Z_{n_1-n_1}$ vs the number of n_1 particles in an ensemble of 27 overlapping particles. $Z_{n_1-n_1}$ is shown with 1.0 σ error bars, based on 1000 samples at each step

Percolation, and therefore conduction, is not possible until a minimum volume of conducting particles are added to the system. This point occurs when the system contains the minimum number of particles to span the dimension for which percolation is being calculated. For ensembles of spherical particles this minimum number is:

$$1 + \frac{L - 2r}{d}, \tag{3.13}$$

where d is the center-to-center distance between the particles. This result is realized by recognizing that the distance spanned by a finite chain of n spheres with radius r and center-center spacing d is

$$(n - 1) \cdot d + 2r . \tag{3.14}$$

If the span of a chain of particles is set equal to L,

$$L = (n - 1) \cdot d + 2r . \tag{3.15}$$

It is possible to recover equation 3.13 from equation 3.15 by solving for n. In Figure 3.14, the percolation probably increases rapidly from this point; this behavior is particular to this specific system. The rapid increase in percolation does not occur until the the average coordination number of particles is greater than 2. This behavior is exhibited in highly-structured simulations of perfectly spherical objects as well. With respect to particle-based electrode simulations, the coordination number is typically what is recorded. In the above example the average coordination number closely mirrors the percentage of conducting particles, n_1. However the property of interest, conductivity, much more closely mirrors the percolation probability, which follows a much more complicated progression, as demonstrated both in the simple example above and in the following sections. As a consequence, percolation and conductivity are discussed in terms of Z_{x-x}.

Table 3.14: Percolation in a 3 X 3 X 3 cubic lattice of particles

Number of Particles	n_1	n_2	No. of Cases	Number of Percolating Cases	Percentage of Percolating Cases
27	0	27	1	0	0.0%
27	1	26	27	0	0.0%
27	2	25	351	0	0.0%
27	3	24	2925	729	24.9%
27	4	23	17550	8748	49.8%
27	5	22	80730	55404	68.6%
27	6	21	296010	240570	81.3%
27	7	20	888030	792666	89.3%
27	8	19	2220075	2088828	94.1%
27	9	18	4686825	4540968	96.9%
27	10	17	8436285	8305011	98.4%
27	11	16	13037895	12942423	99.3%
27	12	15	17383860	17328411	99.7%
27	13	14	20058300	20034783	99.88%
27	14	13	20058300	20049120	99.95%
27	15	12	17383860	17381412	99.99%
27	16	11	13037895	13037436	99.996%
27	17	10	8436285	8436231	99.9994%
27	18	9	4686825	4686822	99.99994%
27	19	8	2220075	2220075	100%
27	20	7	888030	888030	100%
27	21	6	296010	296010	100%
27	22	5	80730	80730	100%
27	23	4	17550	17550	100%
27	24	3	2925	2925	100%
27	25	2	351	351	100%
27	26	1	27	27	100%
27	27	0	1	1	100%

3.2.2.2 Percolation Threshold for Closed Packed Spheres

Particle arrays of heterogeneous close-packed spheres are considered first. The regular geometry of this configuration makes it possible to analytically determine the percolation threshold. The percolation threshold depends on the coordination number between the particles within the particle array. Modeling and experimental results demonstrate that the probability of percolation within a particle system increases rapidly to unity once the probability of percolation is significant. Percolation is possible, $P_p > 0$, if there are enough enough particles of the percolating type to geometrically span the domain.

In these systems there is a progression from percolation being possible to percolation being very likely. For close-packed spheres, percolation is possible for a very low fraction of conducting particles. If the particles are arranged with no overlap, $P_p = 0$ for all cases where there are less than $L/2r$ percolating particles. There is one special case with a single chain of particles spanning L. In this case, with the exception of the two particles in contact with the boundaries, each of these particles is in contact with 2 other particles, with the connections between the particles separated by 180 degrees. The two particles in contact with the boundaries are in contact with one other particle whose contact point is separated from the boundary by 180 degrees. All of the interior particles in the conducting chain have a coordination number of 2 with respect to other conducting particles. The particles at the boundaries have a coordination of 1 with respect to the other conducting particles. $L/2r$ particles are required to span the distance L. In this case, the coordination number between percolating particles is

$$Z_{i-i} = \frac{2 \cdot (\frac{L}{2r} - 2) + 2}{\frac{L}{2r}} \ , \tag{3.16}$$

which can be simplified to

$$Z_{i-i} = 2 - \frac{4r}{L} \ . \tag{3.17}$$

The center-to-center distance between particles is $2r$. Substituting this into equation

3.13 yields the result that the system is spanned by $L/2r$ particles. The total number of particles in the system is $(L/r)^3$. In this case, the percentage of particles which are of the percolating type is the number of percolating particles, $L/2r$, divided by the total number of particles $(L/r)^3$

$$\frac{\frac{L}{2r}}{\left(\frac{L}{r}\right)^3} = \frac{1}{2} \cdot \left(\frac{r}{L}\right)^2 = \left(\frac{\sqrt{2}r}{2L}\right)^2 . \tag{3.18}$$

Consequently, for large ensembles, percolation can be possible with a very small fraction of percolating particles. At this condition, percolating cases are unlikely to occur and are a very small subset of the total possible cases. Of interest is the limit at which percolation becomes likely. There is a clear transition behavior when $Z_{i-i} \sim 2.2$. At this point the percolation probability undergoes a rapid transition from $P_p \sim 0$ to $P_p \sim 1$.

Figure 3.15 shows the progression in the percolation probability for a particle-based Ni-YSZ anode model with a monodispersed particle size distribution. This system has r = 0.3 μm, $L_x = L_y = 7.2$ μm, and $L_z = 21.6$ μm. There are five distinct phases of percolation behavior. 20 cases are run for most of the cases. For the cases with a nickel phase fraction between 0.20 and 0.27—the cases during which the transition to perco-lation occurs, 65—cases were run. The transition region is displayed in greater detail in the inset. These are not enough cases to precisely define the percolation probability, but the progression of percolation with respect to ϕ_{Ni} is clearly illustrated.

1. $\phi_{\text{Ni}} < 0.0022$; Percolation in the z direction is not possible; $P_p = 0$.

2. $0.0022 < \phi_{\text{Ni}} < 0.21$; Percolation is possible but extremely unlikely; $P_p \sim 0$. When the number of particles is greater than the minimum number required for percolation, percolation can occur when $Z_{i-i} < 2$. Percolation is unlikely in these cases. Percolation does not become a likely result until the average Z_{i-i} for a given configuration is greater than 2.

3. $0.21 < \phi_{Ni} < 0.27$; P_p progresses rapidly from approximately 0 to $\sim 100\%$.

4. $0.27 < \phi_{Ni} < 0.986$; $P_p \sim 1$.

5. $0.986 < \phi_{Ni} \leq 1.00$.
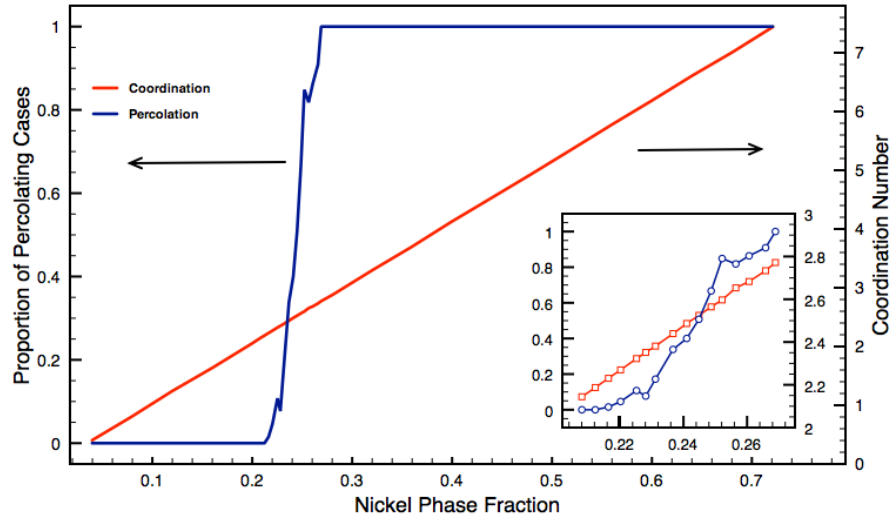
Figure 3.15: Nickel percolation and coordination for a type A system vs Ni phase fraction

The point at which the transition from $p \sim 0$ to $p \sim 1$ occurs has been reported for a number of packing geometries with a monodispersed particle size distribution:

1. .146 for a diamond lattice to .167 for body centered cubic for periodic packings [52],

2. .160 for random tight packing [18],

3. .183 for simulated random packings [38].

In addition, Oger established ϕ_p for particle packings with different size ratios between percolating and non-percolating particles [37].

Figure 3.16 illustrates the onset of conductivity in comparison to the conductivity. The initial conductivity is non-zero because the YSZ phase has a electronic conductivity.

As the nickel phase fraction crosses the percolation region, there is a large increase in the conductivity as the electronic conductivity is dominated by the presence of the percolated nickel network. The electronic conductivity increases at a lower rate with respect to the Ni phase fraction in the region where probability of percolation is $\sim$ 1.0.
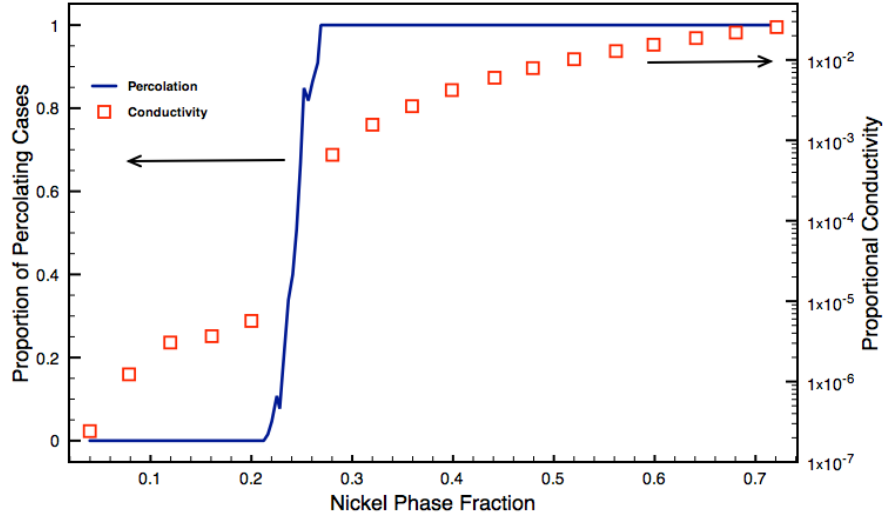
Figure 3.16: Nickel percolation and electronic conductivity for a type A system vs Ni phase fraction

In Figure 3.17 the proportional conductivity is compared to the coordination number. For this set of measurements the electronic conductivity of the YSZ phase is ignored. Conductivity is non-zero only when the Ni is percolated. There is a very sharp percolation threshold, as shown in Figures 3.16 and 3.15. The increase in the conductivity within the region where $p \sim 1.0$ is more gradual. This is because, as shown in Table 3.15, the fraction of Ni particles participating conducting network is nearly 1.0 after the region where $p \sim 1.0$. The increase in the conductivity of the Ni phase is dependent on the increase in the fraction of the nickel phase and the impact of that increase on the geometry of the conduction pathways throughout the medium. This point can be further illustrated by examining the relationship between Z_{i-i} for Ni particles at the onset
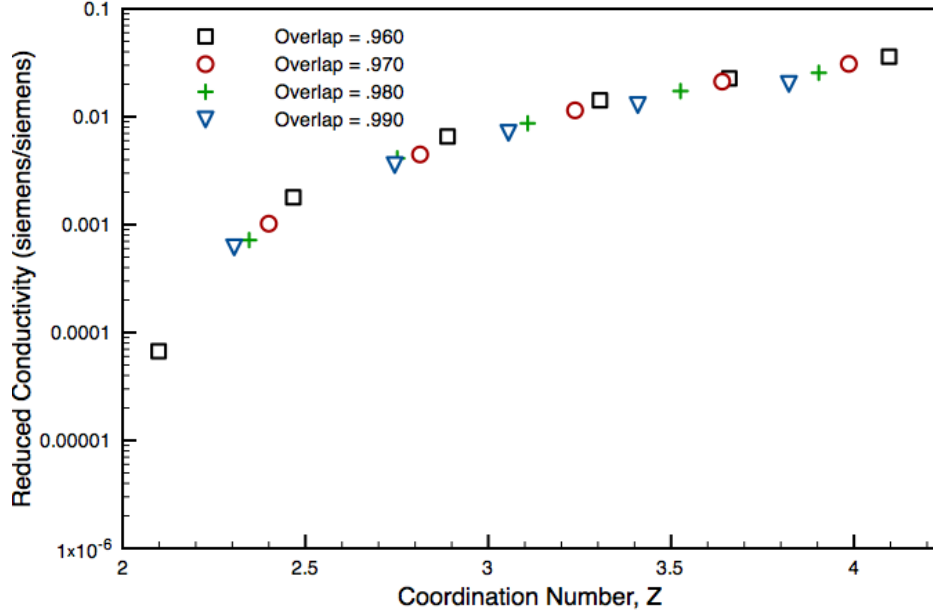
Figure 3.17: Measured conductivity of uniform particle array vs coordination number

of conductivity to the expected values. Based on computational results, Bouvard and Lang [8] proposed the following empirical relationship between Z_{i-i} and the percentage of percolated particles, P_c, for monodispersed systems:

$$P_c = \left(1 - \left(\frac{4 - Z_{i-i}}{2}\right)^{2.5}\right)^{0.4}, \tag{3.19}$$

where Z_{i-i} is the coordination number between like particles. This relation is valid only for cases with percolation. As explained in Section 3.2.2.2, this limits the applicability of equation 3.19 to cases where $Z_{i-i} > 2$. This result follows directly from a physical intuition of the problem, as the minimum requirement for percolation is one continuous chain of particles of type i. When the absolute minimum of particles required for percolation exists within the system, percolation occurs when $Z_{i-i} \sim 2$; however, percolation is not likely to occur until $Z_{i-i} \sim 2.2$. The measured proportion of percolated values from type A cases is compared to equation 3.19 in Figure 3.18. The computational re-

Table 3.15: Mean proportion of percolated Ni particles for percolated monodispersed cases

Φ_{Ni}	Proportion of Percolated Ni Particles
≤ 0.212	0.000
0.216	0.626
0.228	0.684
0.245	0.812
0.256	0.856
0.280	0.915
0.320	0.967
0.359	0.985
0.399	0.993
0.441	0.997
0.479	0.999
≥ 0.520	1.000

sults follow the expected curve closely. We take this as a strong indication that although the packing methodology outlined in Section 2.3.1.1 is significantly different from earlier studies, it is a valid method for studying the behavior of these systems.

3.2.3 Comparison to Previous Results

3.2.3.1 Conductivity

As described in Section 2.1, previous modeling work on this area has focused on models using monodispersed and simple polydispersed distribution of particle sizes. The first step in the evaluation of the model presented here is to compare the results for those distributions with past experimental and modeling work.

Particle-based models of the Ni-YSZ assumption have generally used the assumption that Ni and YSZ particles should either be of equal diameters or a ratio of YSZ:1.0 to Ni:0.781. This assumption is based on the assumption of equal sized particles of YSZ and NiO in the precursor mix, and the subsequent reduction of NiO to Ni in the
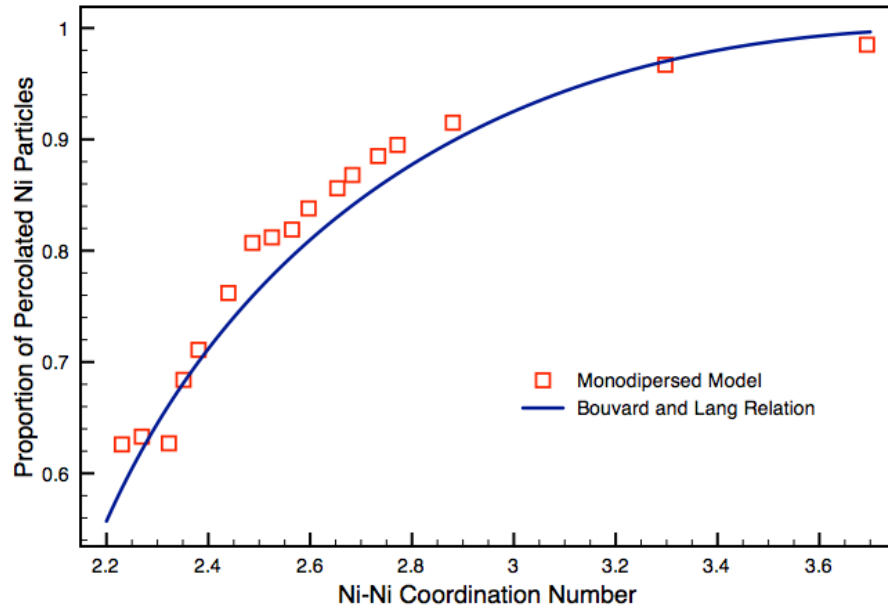
Figure 3.18: Comparison of proportion of percolated particles with Bouvard and Lang relation (Equation 3.19)

manufacturing process. This assumption leaves out the fact that unless the precursor elements are milled in the same type of machinery, they will in fact not have the same particle size or particle size distribution. This is an important fact, as the difference in average particle size (and particle size distribution) does impact the conductive properties of the material. Dees [14] and Huebner [28] demonstrated that both differences in precursor material properties and in Huebner's case, manufacturing procedures produce different Ni conductivity. Dees measured conductivity for Ni-YSZ cermets using two different types of YSZ powders. The results are shown in Figure 3.19. The Toyo Soda powder has a larger average particle size than the Zircar powder. Data particle size distributions are available. Data from type A and B systems are also shown in this graph. The lines in the graph serve to guide the eye and do not represent an underlying functional relationship.

Figure 3.19 shows that the Ni conductivity has both a sharper onset and higher peak
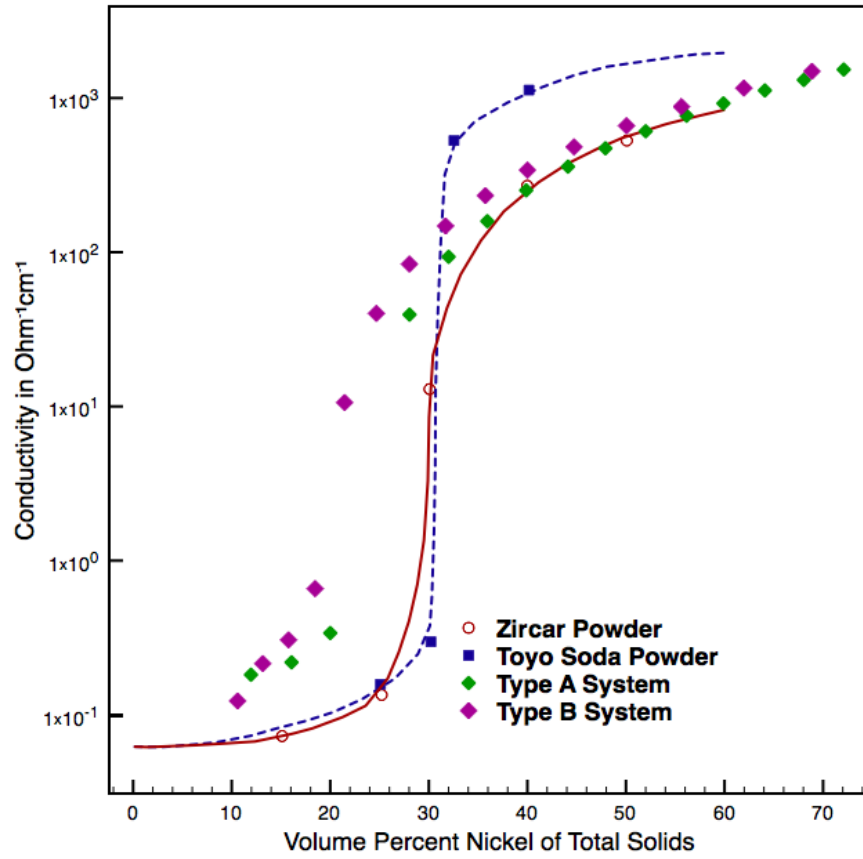
Figure 3.19: Effect of the Ni phase fraction on the conductivity of Ni-YSZ cermets for systems of type A and B, as well as data published by Dees et al. [14]

when combined with the YSZ powder having a larger agglomerate size. The type A calculation shows a very similar behavior for higher Ni phase fractions. The percolation threshold occurs earlier, and the values at low Ni phase fractions are significantly higher. We believe this result to be the result of overestimating the contact resistance between Ni and YSZ phase particles. The type B systems show a comparatively lower percolation threshold. While this result is consistent with other particle-based modeling [46, 48], it is contrary to the result indicated in the Dees data. This indicates a limitation in trying to project the qualitative behavior of composite anodes using these types of simple models. Possible reasons for this discrepancy are addressed in greater detail in Chapter 4

These results are also echoed in experiments produced by Huebner et al. [28], illustrated in Figure 3.20, as well as in the computational results of Sunde, which match Dees' data quite closely. In Huebner's results the percolation threshold occurs at lower Ni phase fractions, between 0.20 and 0.25. Huebner's results also directly illustrate that, even when using the same input materials, the conductivity properties depend on the fabrication process—in this case parametrized by the sintering temperature. The results for the monodispersed model shows similar behavior, with the percolation threshold occuring at a slightly higher Ni phase fraction than the experimental cases, and the same discrepancy in behavior at low Ni phase fractions that was evident in Figure 3.19

Sunde compared a monodispersed particle model to Dees data [46, 48], in order to demonstrate the validity of his approach. However, in order to obtain a reasonable quantitative match to the Dees data, Sunde adjusted the inter-particle resistance. This adjustment of the overlap makes the particle-to-particle resistance in this model a fitting parameter rather than a phenomenological one. As shown in Figure 3.21, this parameter fit can produce strong agreement near the percolation threshold, but overstates the conductivity of the cermet at higher Ni phase fractions. The limitation of this approach
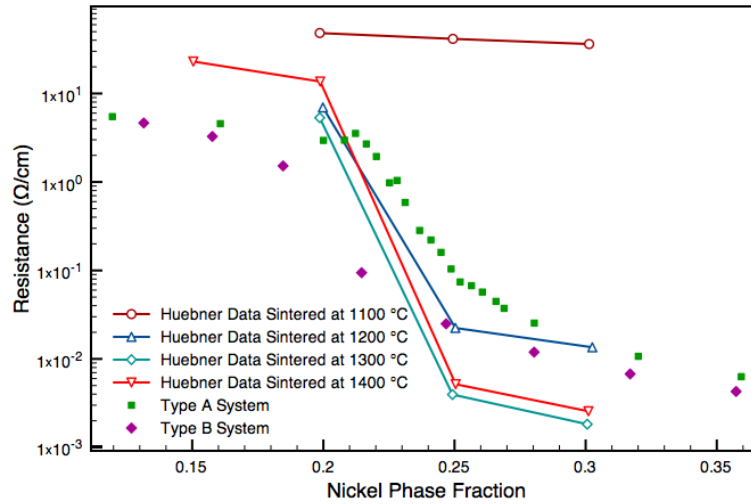
Figure 3.20: Comparison effect of the Ni phase fraction on the conductivity of Ni-YSZ cermets to data published by Huebner et al. [28]

is that it does not yield a phenomenological approach to predicting the overlap that should be used between particles. While it should be possible to further develop guidelines for using this approach to determine an overlap parameter, this approach has not been explored in the literature. Consequently, this approach is left with the limitation of being a backward-looking approach, which can successfully predict the properties of data to which it has been fit. In addition, while Dees provides data for two different initial powder geometries, only one of two geometries is investigated by Sunde. This leaves open the question of whether the matching method used by Sunde can be applied to other cases, and also whether each particular geometric case will require a different result.

The two assumptions of overlapping spheres with a uniform overlap does yield similar qualitative performance as experimental results. However, in terms of actually quantitatively matching the data, these models fall far short. As shown by Sunde, the underlying assumptions of these models can be adjusted to fit the data, but there is no systematic method to make these adjustments based on phenomenological data. Consequently,
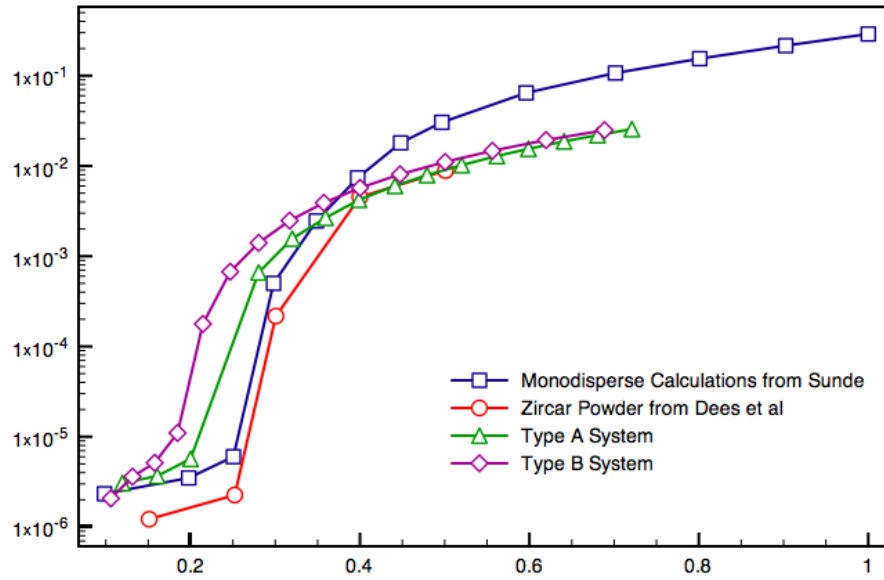
Figure 3.21: Comparison of Sunde's particle-based conductivity model with Dee's experimental results [46]

this type of model creates a situation where the model can be adjusted so that it can correctly match an existing data set, but cannot be used to then extrapolate the quantitative effects of phenomenological changes in the system. One approach to trying to improve this situation is to drop the assumption that the particles within the model obey simple distributions. This approach will form the basis of the next section.

3.3 TPB Length and Connectivity

The next major set of comparisons is the density and connectivity of the TPB. The density of the TPB is defined as the sum of the lengths of all of the TPBs divided by the volume of the composite cermet model. As detailed in Section 1.1.1, in an actual fuel cell a TPB section is only functional if the respective Ni and YSZ phases which are part of that TPB section have a conduction path to the electrode and electrolyte, respectively.

The method for determining whether a TPB section is functional is explained in detail in Section 2.3.3.2. For the monodispersed system, the TPB is a symmetric function of both the Ni and YSZ phase fractions, with the maximum occurring at $\phi_{Ni}=\phi_{YSZ}$. This can be seen in Figure 3.22. The occurance of the maximum TPB length at $\phi_{Ni}=\phi_{YSZ}$ confirms the results from Schneider [42] for monodispersed particle ensembles. The TPB sections consist of the circles of intersection between heterogenous particles. Decreasing λ increases the circumference of the circle of intersection between overlapping particles. Because of this the TPB length is a decreasing function of λ, as seen in Figure 3.22
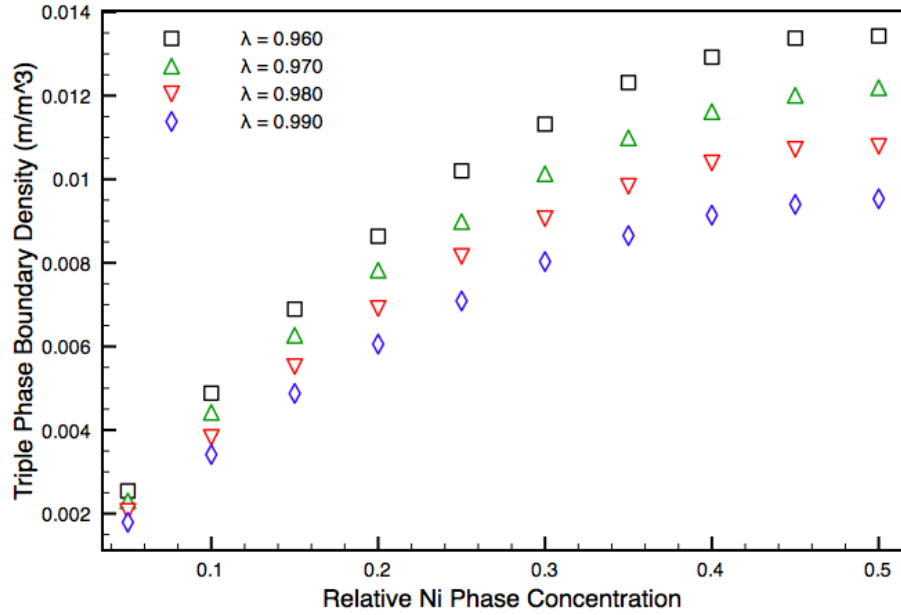
Figure 3.22: TPB density for type A systems

The functional TPB length is dominated by percolation within the particle model. Figure 3.23 shows that the functional TPB is minimal until the percolation threshold is reached. If these values are compared to the percolation from Figure 3.15, it can be seen that for the type A system percolation is largely achieved when $\phi_{Ni} \geq 0.27$. In order to highlight the symmetry of these results with respect to the relative phase concentration

of Ni versus YSZ defined as

$$\frac{\phi_{\text{Ni}}}{\phi_{\text{Ni}} + \phi_{\text{YSZ}}} \ , \tag{3.20}$$

the x coordinate is the relative phase concentration, as opposed to ϕ_{Ni}. The transition behavior shown in Figure 3.22 does coincide with the percolation threshold for the type A system as described in Section 3.2.2.2.
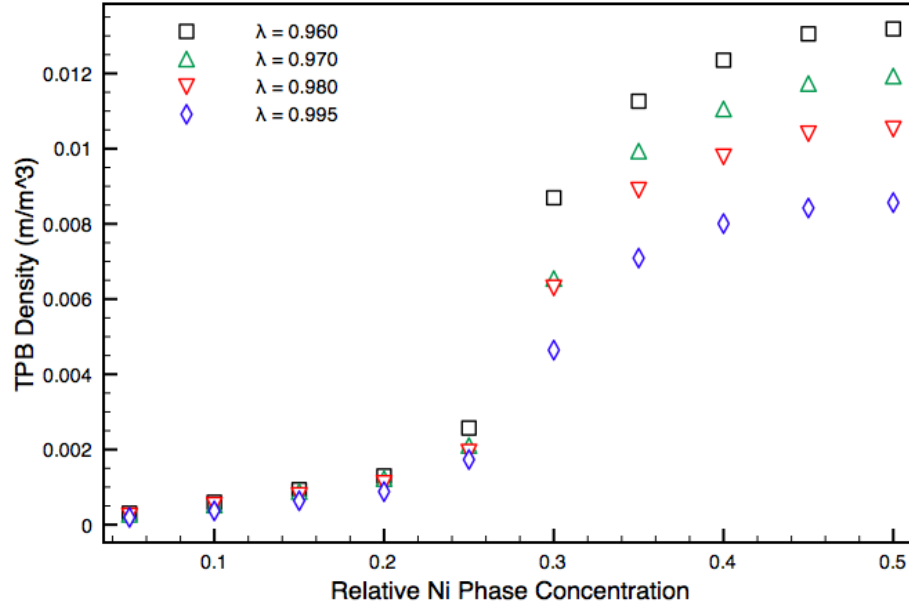
Figure 3.23: Functional TPB density for type A systems

For the type B system, the symmetry with respect to the relative phase concentration of Ni versus YSZ is not present. This can be seen in Figure 3.24.

3.4 Experimental Distributions

As discussed in Section 2.1, recent research has made it possible to understand the particle size distribution of both the precursor particles used to create composite cermets and to measure the size distribution of the resulting particle agglomerates with a com-
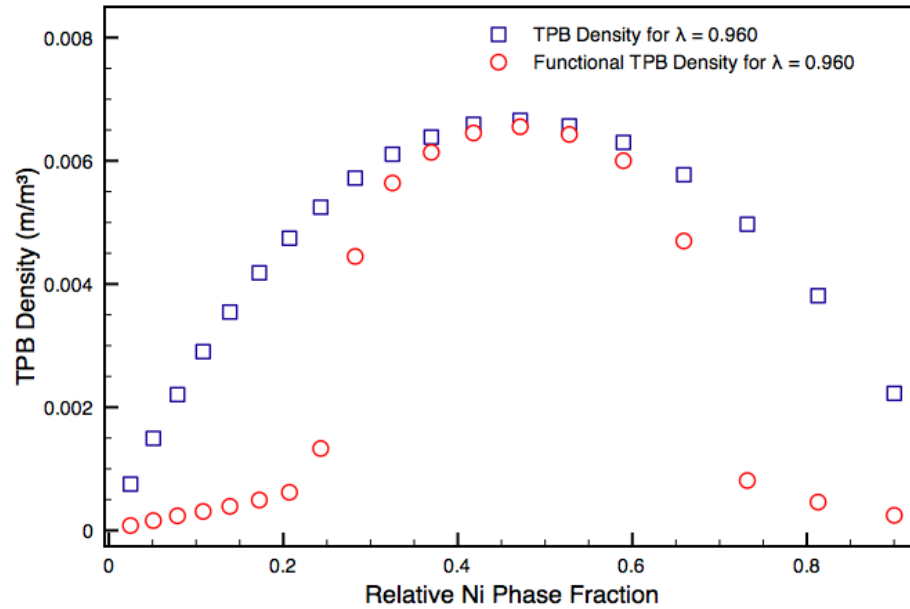
Figure 3.24: TPB density and functional TPB density for type B systems with $\lambda = 0.960$

posite electrode in situ. With this data it is possible to construct particle-based models with far more complex internal structures. The important question with respect to these types of models is: Does the additional complexity yield better quantitative prediction or new qualitative insights into the behavior of composite electrodes? Also, with monodispersed and simple polydispersed particle distributions it is possible create particle arrays whose structure goes beyond the configurations explored in Section 3.2.3.1. For example, it is possible to consider monodispersed particle distributions with non-uniform distributions of inter-particle overlaps. In terms of monodispersed and simple polydispersed ensembles, there is no rationale for exploring particle orientations which are not essentially random. In considering more complex particle size distributions, this question of spatial distribution becomes more important. The initial hypothesis is: Increasing the complexity of the ensembles by better matching the size distribution of the particles will improve the match between model and experiment.

In this section we will examine the properties of particle assemblies using experimentally determined particle size distributions which have been described in greater detail in Section 2.3.2.2. The results of these calculations will differ greatly from the results of uniformly distributed ensembles. These results will be examined in the light of experimental data that can give insight into the divergence between the two classes of solutions. In the final part of this chapter, the results based on experimental particle size distributions will be extended. As noted in detail in Section 2.3.2.2 the experimental distributions have no closed-form analytical expression, but are similar to logarithmic distributions.

The two particle size distributions used in this sections are based on the work of Cho et al. The particle size distributions are displayed in Figure 3.25. The nomenclature of labeling the distributions 'NY-1' and 'NY-2' will be retained. Figures 3.26 and 3.27 show particle models constructed using these particle size distributions.
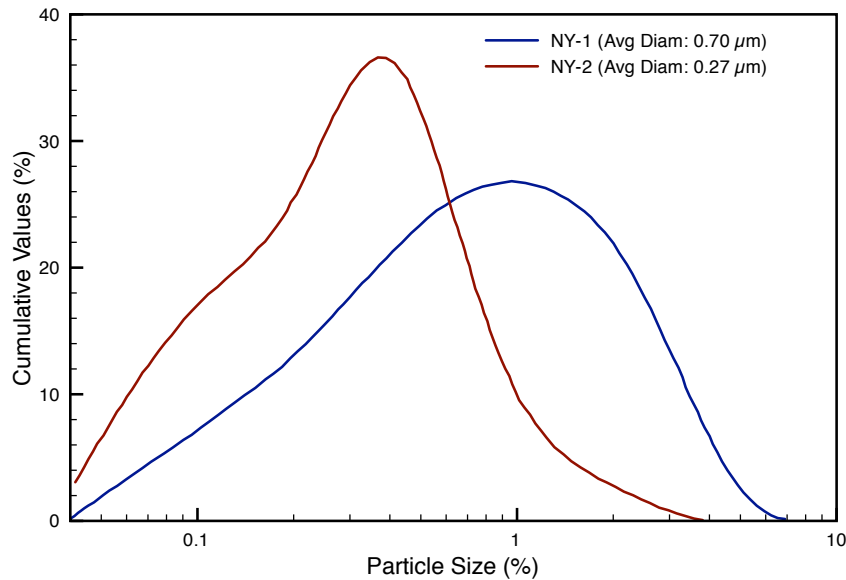
Figure 3.25: Particle size distributions published by Cho et al. [11]
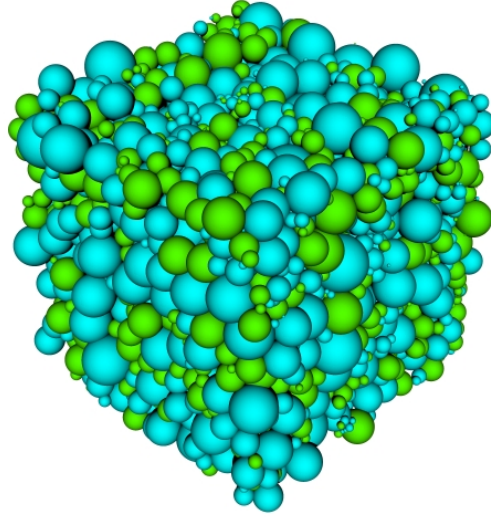
Figure 3.26: Particle model based on NY-1 particle size distribution published by Cho et al. [11]

3.4.1 Conductivity

The conductivity results for the NY-1 and NY-2 distributions show a similar behavior to the type A and type B systems, as shown in Figures 3.28 and 3.29.

The nominal performance of the NY-1 and NY-2 systems is very similar to the performance of the monodispersed and simple polydispersed systems. The percolation behavior of the NY-1 and NY-2 distributions is also similar, in that the percolation threshold occurs near $Z_{i-i} = 2.2$. We did not make detailed calculations in the area of the percolation threshold, as was done for the type A systems, but for both NY-1 and NY-2 systems there was no percolation of the Ni phase until $Z_{i-i} > 2.2$. In terms of the nominal performance, there is a question of whether the more complex scheme provides more information than using simpler models. There is a significant difference in the conductivity performance of the NY-1 and NY-2 systems which is not apparent in the monodispersed and simple polydispersed models.
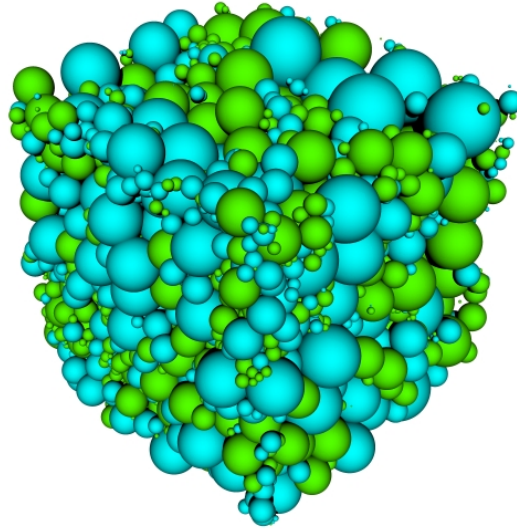
Figure 3.27: Particle model based on NY-2 particle size distribution published by Cho et al. [11]

In Figures 3.30 and 3.31 the reduced conductivity is plotted with $\pm\sigma$ error bars. The variance in the conductivity of the experimentally-based ensembles is significantly larger than for the monodispersed case. The type B system is not shown, for clarity, but the variance in the reduced conductivity of the type B system is similar to that of the monodispersed type A systems. Without experimental data on the variability of performance of composite anode sections, we cannot say with confidence whether this significant behavioral departure is more or less reflective of real world performance, but we believe understanding what level of variability does exist in real systems is very important in understanding designing useful tools for modeling the performance of Ni-YSZ composite anode systems.
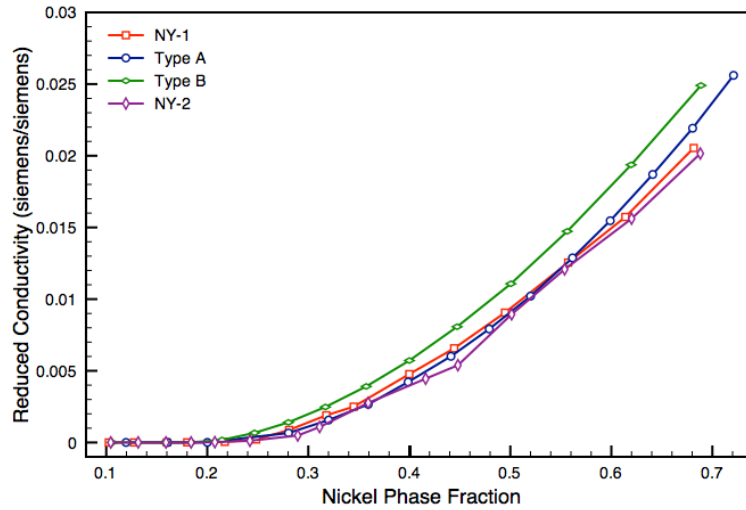
Figure 3.28: Comparison of reduced conductivity between particle ensembles of types A and B and particle ensembles based on the experimental measurements of Cho et al. [11]

3.5 TPB Length

The TPB properties of the model using experimentally-based distributions differ significantly from the cases where the particle size distributions are monodispersed or simple polydispersed. The TPB density for the NY-1 and NY-2 cases shows the same qualitative nominal behavior as the type A and type B cases. The total TPB length is maximized near the point at which the solid phase fractions are equal. With regard to the proportion of the TPB which is available for electrochemical reactions, there is a sharp percolation-driven increase which occurs when the nickel phase fraction is near the percolation threshold for electronic conductivity, and a similar decrease when the YSZ phase fraction is near the percolation threshold for ionic conductivity. This is visible in Figures 3.32 and 3.33

The variability of the TPB lengths for the NY-1 and NY-2 cases is significantly higher than for the type A and type B cases. For the type A cases the σ/μ for both TPB length is less than 0.04 for all cases. As for the conductivity measurements there is no
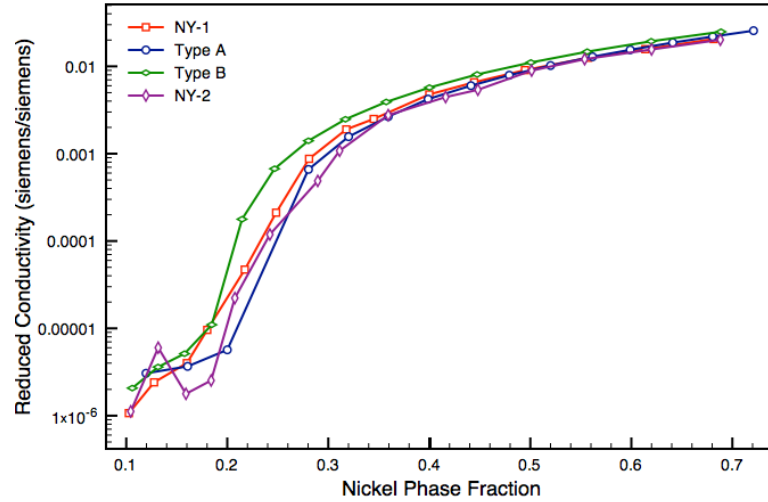
Figure 3.29: Comparison of reduced conductivity between particle ensembles of types A and B and particle ensembles based on the experimental measurements of Cho et al. [11]

basis in the literature for deciding whether lower or higher variability is more reflective of physical Ni-YSZ composite anode systems. For the functional TPB length, the results (shown in Table 3.16) are more complicated. In the region where both cases are percolated, the σ/μ is < 0.03. In the percolation threshold regions, the variation is significantly higher. With respect to the NY-1 and NY-2 cases, the range of values of σ/μ is from 0.3–0.9 and 0.5–1.1, respectively. Moreover, these values do not have a significant variation with regard to the percolation state of the system. The values are shown graphically in Figures 3.34 and 3.35

In addition to the increased variability in the measurements, there is a significant difference in the calculated values for the TPB density for the NY-1 and NY-2 systems. Figure 3.36 shows the TPB density of all of the systems examined in this chapter. The TPB density of the NY-2 system is approximately two orders of magnitude lower than both the type A and type B systems. The TPB density of the NY-1 systems is approximately three orders of magnitude lower than both the type A and type B systems. Wilson et
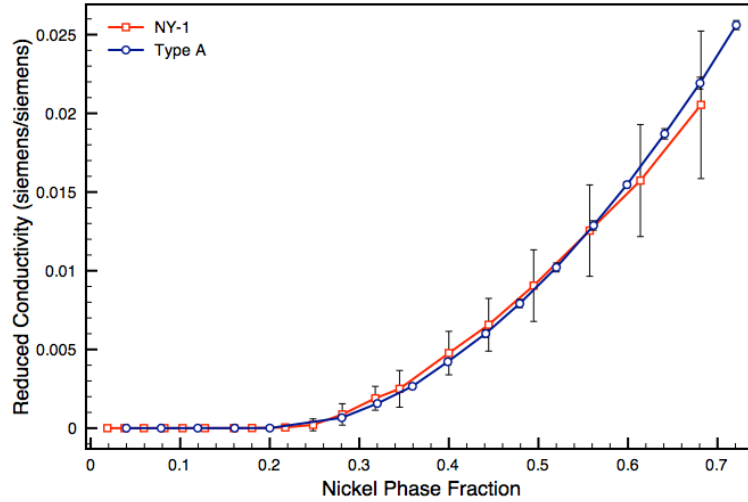
Figure 3.30: Comparison of the variability in reduced conductivity between particle ensembles of type A and particle ensembles based on the experimental measurements of Cho et al. [11]

al. measured the TPB density of a Ni-YSZ anode with $\phi_{\text{Ni}} = .195$ and $\phi_{\text{Ni}} = .544$ [51]. They measured a TPB density of $4.28 \times 10^{12}\text{m/m}^3$, which is slightly lower than the TPB density for the type A and B cases, but significantly higher than either the NY-1 or NY-2 case. More importantly, in that case $> 90\%$ of the TPB was one section. This result is not captured by any of the configurations that we have evaluated in this chapter. A nearly contiguous TPB indicates that the Ni and YSZ phases are themselves nearly contiguous, a result that, in the models being evaluated here, occurs only near the point where $\phi_{\text{Ni}} = \phi_{\text{YSZ}}$.

3.6   Conclusions

In terms of measuring the phase conductivity, modeling the Ni-YSZ cermet anode system as a simple particle ensemble can produce reasonable qualitative results when compared to the available experimental results. Adding complexity in terms of duplicating the
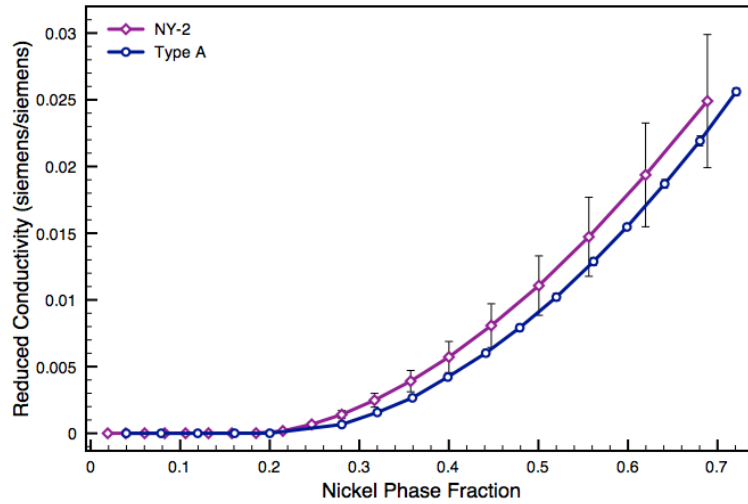
Figure 3.31: Comparison of the variability in reduced conductivity between particle ensembles of type A and particle ensembles based on the experimental measurements of Cho et al. [11]

precursor particle size distribution does not appreciably improve the predictive ability of the model, but it does increase the variability of the results. We cannot know based on the the information that we have whether this increase in variability is a feature which improves or degrades the performance of the model in terms of reflecting the performance of the physical system.

We expect both the extent and geometry of the TPB to strongly affect the electrochemical performance of Ni-YSZ anode systems. For this reason the large variance in the TPB density based solely on the particle size distribution is disconcerting. Hanna [23] has discussed the difference between the TPB density and structure of particle-based models as compared to physical systems, but in those cases the differences were less than one order of magnitude. It is necessary to have a better understanding of the true geometry of the TPB in Ni-YSZ anodes. It is important to consider the possibility that for a more complex model which considers the TPB electrochemistry, the values to be used for the TPB density will have to be estimated from factors beyond the geometry
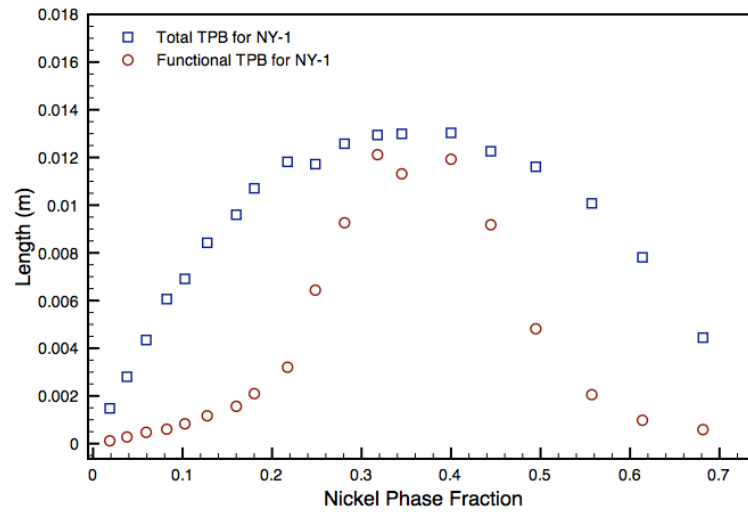
Figure 3.32: TPB length and functional TPB length for NY-1

produced by particle-based models.
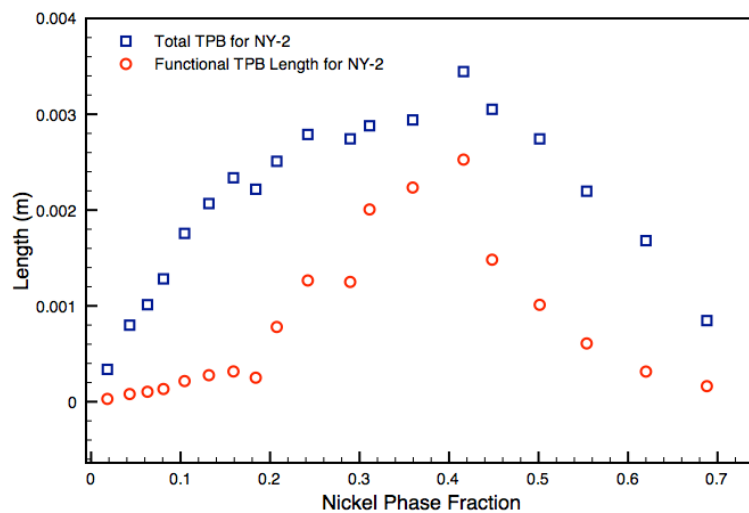
Figure 3.33: TPB length and functional TPB length for NY-2

Table 3.16: σ/μ for functional TPB length of type A cases

Φ_{Ni}	σ/μ
0.0397518	0.143
0.0786688	0.0908
0.119563	0.102
0.160729	0.0892
0.200024	0.3361
0.280418	0.0270
0.320086	0.0076
0.359332	0.0079
0.398808	0.0076
0.441201	0.0074
0.479162	0.0133
0.520046	0.0186
0.561557	0.3506
0.598898	0.3756
0.640959	0.110
0.680459	0.0775
0.720963	0.0875
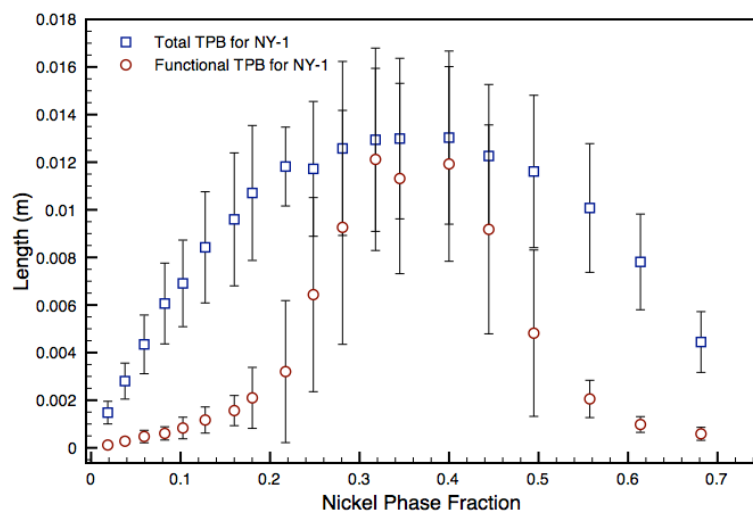
Figure 3.34: TPB length and functional TPB length with $\pm\sigma$ error bars for NY-1
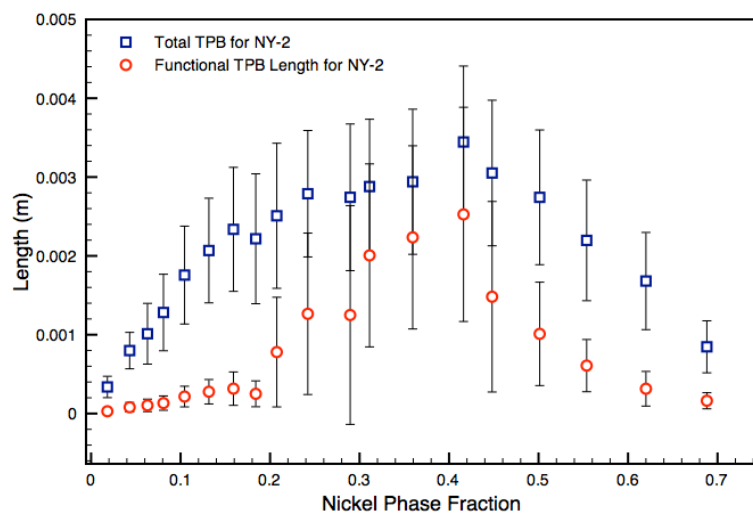
Figure 3.35: TPB length and functional TPB length with $\pm\sigma$ error bars for NY-2
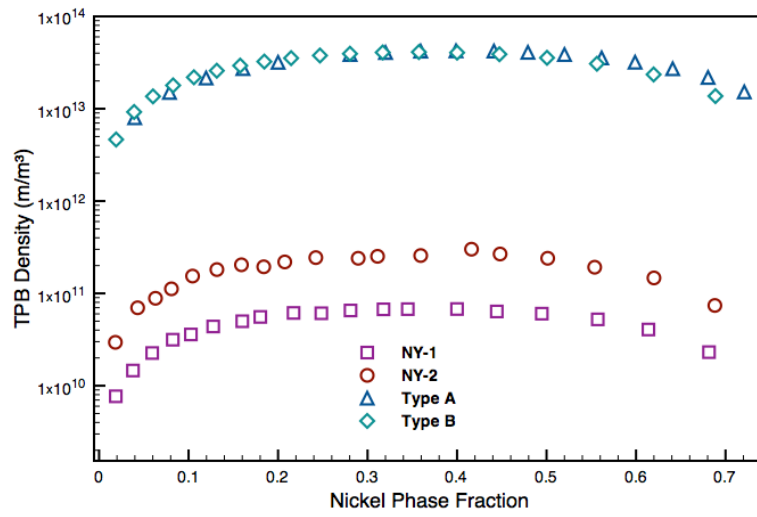
Figure 3.36: Comparison of TPB density

Chapter 4

Measurements of Ni-YSZ Interactions and Importance for Particle-Based Modeling

4.1 Introduction

In Chapter 3, we determined that a particle ensemble composed of essentially random ensembles with monodispersed and simple polydispersed particle size distributions gave useful results in terms of predicting the qualitative behavior of SOFC composite anode structures. Attempting to improve and extend those results by adding greater detail, principally by using continuous distributions of particle sizes based on experimental measurements, did not improve the qualitative or quantitative predictive ability of the models at all. In fact, the addition of these additional factors, in some ways, reduced the usefulness of the models. In this chapter, reasons for these rsesults are explored. The emphasis of this chapter will be on understanding how the presence of structure within a composite anode precludes the assumption that the distribution of particles is essentially random. In this context the term structure will denote any deviations from the random spatial distribution of particles. Two approaches will be used to understand this point. In Section 4.2, the dynamics of Ni percolation within the cermet will explored

by considering the behavior of thin Ni coatings on YSZ substrates, particularly at temperatures that can be expected to arise during the manufacturing and operation of a Ni-YSZ composite anode. In Section 4.3, the experimentally determined structure of one particular composite anode section will be examined to determine the critical differences in the structure of an actual composite anode versus an essentially random particle assembly.

4.2   Pulsed Laser Deposition (PLD)

As discussed in Chapter 2, particle array models have been used in metallurgy to study the properties of powder-based structures. In those cases the problem being studied is the interaction of particles with uniform physical properties; in addition, no chemical changes are involved in the process. In the case of a SOFC electrode, particularly in the case where a metal such as Ni is used as a major constituent, the formation processes involve a level of complexity that limits the ability of particle packing to approximate physical processes.

When a uniform set of hard particles, with relatively uniform compression characteristics, are pressed, the deformation is well understood. The extent of deformation from the spherical is typically small, 4% [34, 43]; in addition, the center-to-center distance between particles remains nearly uniform. However, in an Ni-YSZ anode, the precursor materials are often YSZ particles and NiO particles. The NiO is then reduced in situ to Ni. The reduction to Ni produces a number of important changes to the resulting cermet structure. The NiO loses a substantial portion of its initial volume, producing most of the void phase within the electrode. At the temperatures which are experienced during the manufacture of a Ni-YSZ SOFC cermet, the Ni has significantly lower resistance to deformation as compared to YSZ. As a result the deformation and arrangement forces on the YSZ matrix are no longer easily calculable. In addition, we will demonstrate

that at these same temperatures, the Ni phase will undergo deformations which are not induced by the contact pressure between particles.

In terms of the parameters of interest listed earlier, the behavior of the Ni phase will most strongly affect the percolation of the Ni phase and the length of the TPB. We explored the behavior of Ni in contact with YSZ via a series of experiments. In these experiments Ni was applied to a single crystal YSZ substrate via pulsed laser deposition. In one series of experiments the Ni was applied to the YSZ at near room temperature. In the second set of experiments the Ni was applied to a substrate that was heated to temperatures in the range of 460–500°C. The major result from these experiments was that the Ni demonstrated both high mobility and a high surface tension, which resulted in self-aggregation of the Ni on the surface of the YSZ. Scanning electron microscope (SEM) images of the Ni-coated surface of a YSZ surface were obtained in which the coating was applied via PLD in a vacuum environment at both a lower temperature range of 25–38°C and a higher temperature range of 460–500°C.

4.2.1   Experimental Setup

PLD is a conceptually simple method for depositing thin films, first discovered in the 60s [44]. A high-power laser is used to vaporize a substrate material in a vacuum. The vaporized material forms a plume which expands in the direction of the substrate to be coated. While this process is conceptually simple, actually producing high quality coatings using this approach is a complex enterprise. The concepts and techniques of PLD are described in great detail in *Pulsed Laser Deposition of Thin Films* by Chrisey and Hubler [12]. For this particular set of experiments we used a Lambda-Physik, Inc., 248 nm krypton-florine excimer laser capable of a 500 mJ energy/pulse with a pulse width of 34 ns as the energy source. 99% pure Ni was used as the target, and 1 cm × 1 cm × 1 mm single-crystal specimens of YSZ were used as the substrate to be coated. The Ni target was mounted on a spindle rotating at 0.11 Hz. Rotating the

target with respect to the laser reduces the incidence of splashing on the coated surface. The YSZ substrate is mounted on a heater using stainless steel clips. A schematic of the experiment, as well as images of the setup, are given Figures 4.1, 4.2, and 4.3. In addition, a thermocouple was placed in contact with the midsection of one edge of the YSZ substrate in order to measure the temperature of the substrate during the coating process.

During the coating process the vacuum chamber was maintained within a pressure range between 0.55 and 0.85 milliTorr. The operating conditions for the laser were 500 mJ/pulse at 10 Hz. Two distinct temperature regimes were used:

1. Low Temperature: The substrate was unheated, except by the plume caused by laser ablation of the Ni target. In these cases the initial temperature of the substrate was typically 25°C, with an induced temperature rise of approximately 0.22°C per minute up to 38°C during the 1st hour of coating.

2. High Temperature: The substrate heater was used to ramp the temperature from ambient to 460°C over a one hour period at a heating rate of 0.12°C per second, in addition to the heating during the coating process. The temperature was ramped at rate of 0.12°C per second after the cooling was done, over a period of 90 minutes, in order to prevent the buildup of large thermal gradients during the cooling process.

The thickness, smoothness, and overall profile of the coatings were measured using a profilometer, and images of the surface were generated using SEM. As will be discussed in Section 4.2.2, the change in the temperature regime produces a very large change in the resulting layers of Ni on the YSZ substrate.

The plume produced by the laser-induced ablation of the Ni target contains a dynamic combination of vapor, plasma, and droplets. This leads to a major problem in producing usable coatings. Liquid droplets can be ejected from the target, as well as condensed
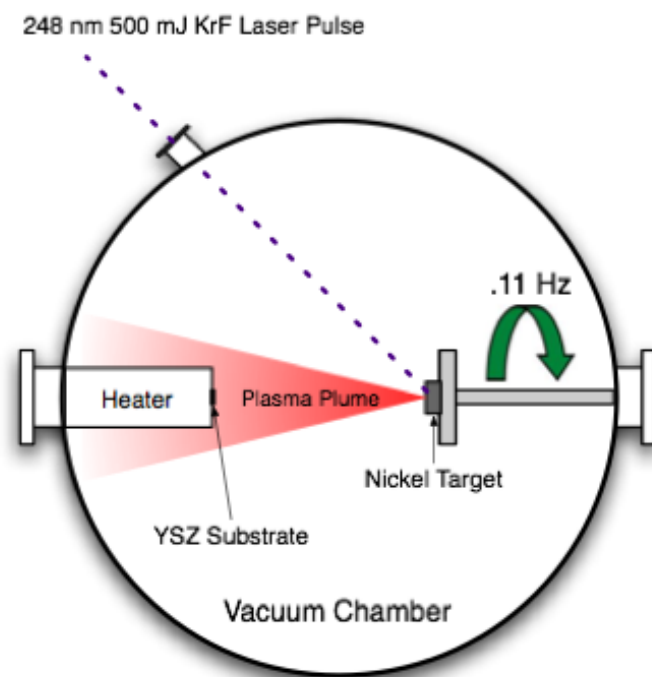
Figure 4.1: Illustration of the PLD setup for coating a YSZ substrate with Ni
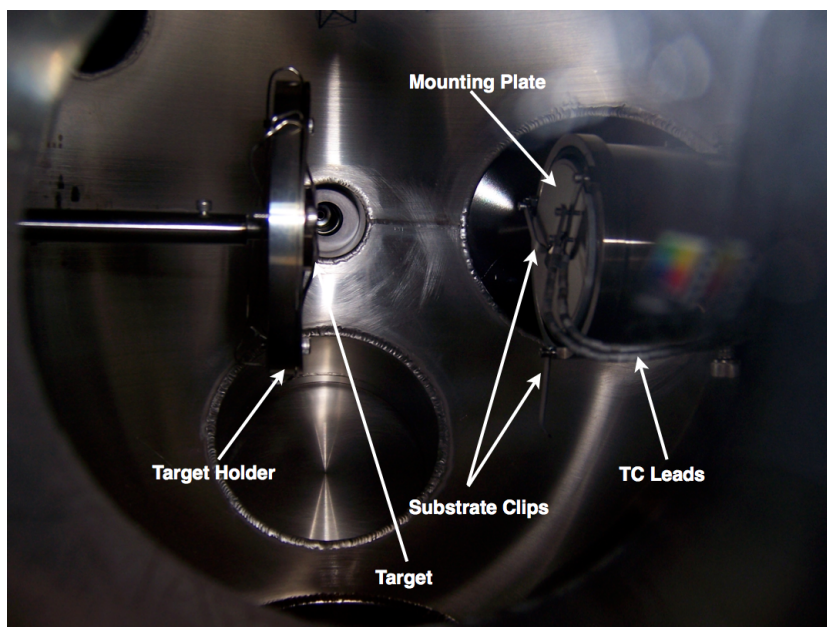
Figure 4.2: PLD setup for coating a YSZ substrate with Ni
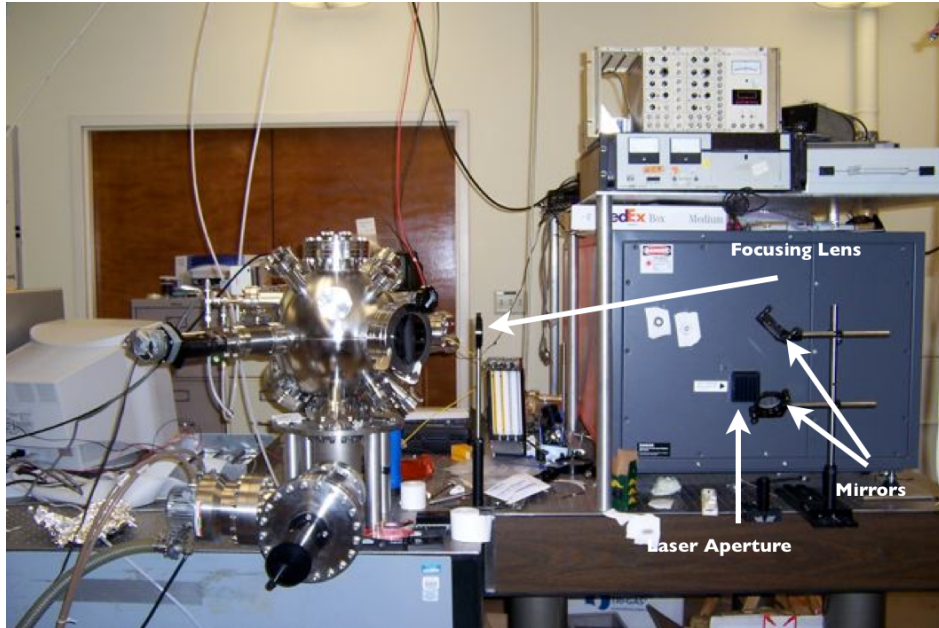
Figure 4.3: PLD setup for coating a YSZ substrate with Ni

within the plume. Droplets that are deposited on the substrate form particulates on the surface of the substrate. The diameter of these particulates can be large with respect to the desired thickness of the coating, obscuring the thickness and smoothness measurements. Figure 4.4 shows SEM images of both high temperature and low temperature coating with a high incidence of particulates. The formation of these particulates are influenced by a number of factors, including the laser wavelength [29], the distance between the target and the substrate, the angle of incidence between the laser and the target, and the quality of the vacuum.

We took steps were taken to minimize the incidence of particulates:

1. The Ni target was mounted on a spindle rotating at 0.11 Hz during coating. The purpose of the rotating spindle is to minimize the laser striking regions of the target which are still heated from the previous laser pulse.

2. The laser is directed at a fixed point. Because the target is rotating, the laser

traces a circle onto the target. The target was positioned such that this circle occurred as close to the outer edge of the target as was deemed safe. Similar to (1), the purpose of this choice is maximize the distance between sequential laser pulses on the Ni target.

Using these two strategies, it was possible to greatly reduce the amount of particulates being deposited on the YSZ substrate and produce coatings which were useful for analysis, as demonstrated in Figure 4.4.
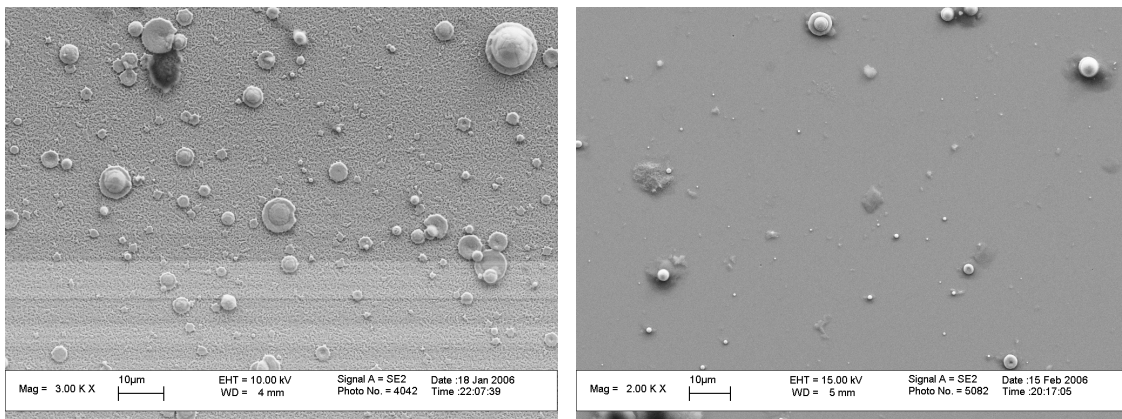
Figure 4.4: SEM images for PLD coating with a high incidence of particulates, for a coating at 460–500°C and a coating at 25–35°C, respectively

4.2.2 Results and Discussion

The spherical and irregular structures are caused by droplets of Ni impacting the surface during the deposition process. Other than these imperfections, the Ni leaves a fine-grained surface which evenly covers the surface of the YSZ. The images below are of the same surface at higher resolution. There is no visible structure or asymmetry within the Ni coating.

The Ni component of composite anodes is produced within a high temperature reducing environment. To partially simulate this environment, the PLD process was conducted
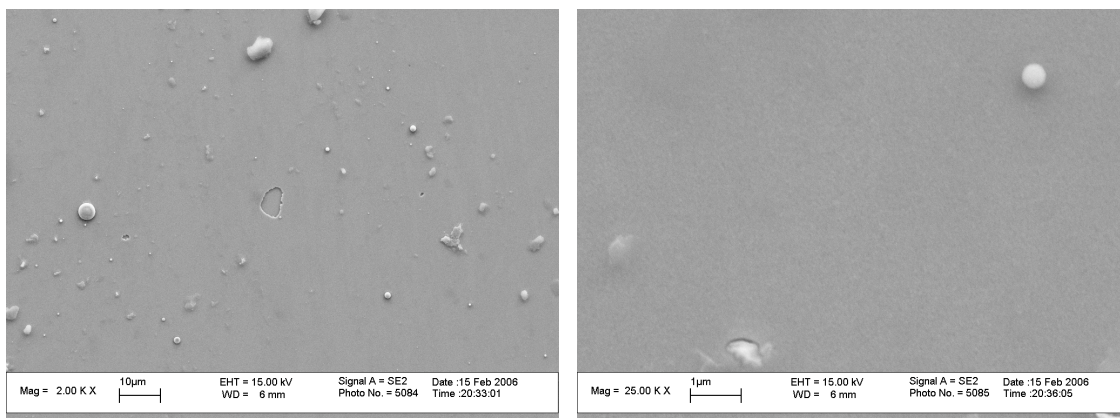
Figure 4.5: SEM images for PLD coating with a high incidence of particulates, for a coating at 25–35°C
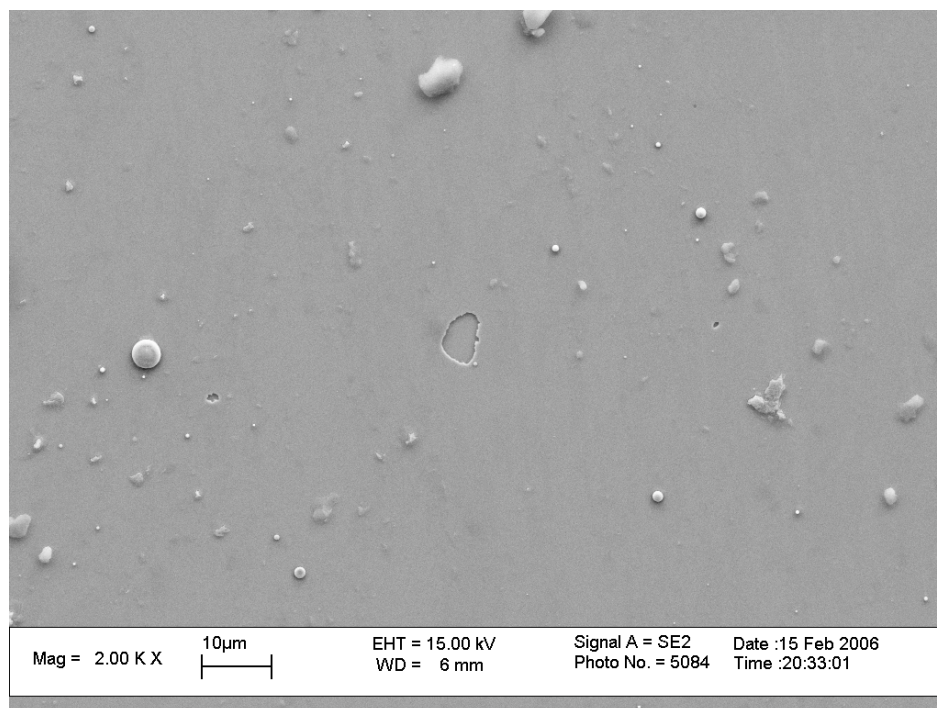
Figure 4.6: SEM image of a low temperature PLD Ni coating on YSZ

on a heated substrate of YSZ. We heated the substrate to approximately 460–500°C, well below the melting point of Ni, or the temperatures that would be experienced during either manufacture or operation of a Ni-YSZ composite anode. In this case the resulting Ni deposition did not evenly coat the surface. Most of the Ni coating formed into a network, leaving parts of the YSZ surface exposed. The Ni which was not part of the network formed isolated nodules along the surface of the YSZ. The SEM images in 4.7 and 4.8 illustrate this point.
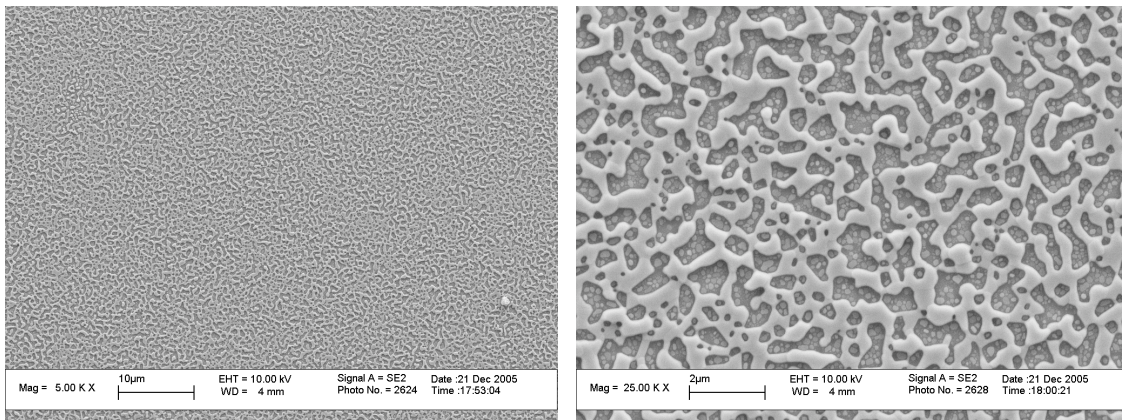
Figure 4.7: SEM images of high temperature PLD Ni coating on YSZ

The PLD experiments, as well as the measurement of Huebner [28] discussed in Section 3.2.3.1, indicate that the conditions of the manufacture of composite electrodes can have a strong impact on their structure. It would be ideal to find evidence to support these conjectures in actual SOFC anodes. As described in greater detail in Chapter 2, recent breakthroughs have allowed the three-dimensional structure of SOFC electrodes to be visualized. Analysis of these reconstructions can provide a confirmation of the expected structure of the Ni phase. In addition, the underlying data from these reconstructions can provide a method of creating a particle-based SOFC model which is more representative of actual SOFC electrodes.

To this end we will use the a sequence of SEM images which show the internal structure of a representative SOFC anode. To create these images, a thin layer of the electrode
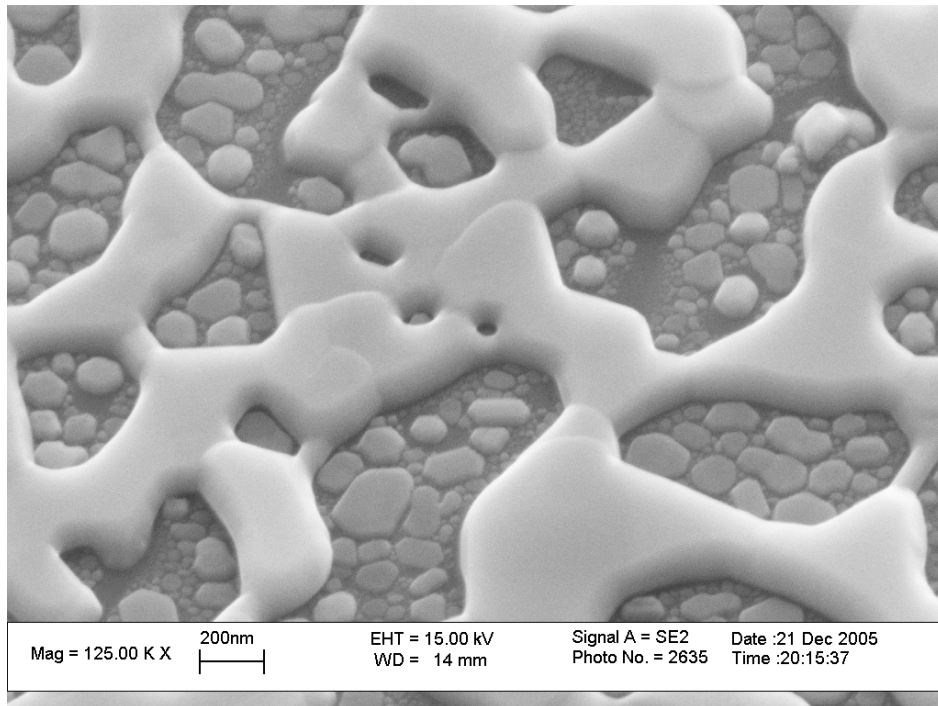
Figure 4.8: SEM image of a high temperature PLD Ni coating on YSZ

is milled via a dual-beam focused ion beam (FIB) between each SEM image. This pioneering work was published by Wilson et al. [51], and the original SEM image files were shared for this project. In Section 4.3 of this chapter, a process for creating a sphere-based reconstruction from the FIB-SEM images will be presented. The resulting reconstruction will be compared to the results of the particle-based ensembles introduced in Chapters 2 and 3. The patterns of connections between particles of various sizes will be of particular interest. In particle ensembles with an essentially random spatial distribution of particles, the likelihood of particles of particular sizes being in contact is related only to the relative particle size and abundance. In the particle reconstruction based on the FIB-SEM images, the likelihood of connectivity between particles will show a different pattern. Additionally, the connectivity of the TPB will be of interest. In the original voxel-based reconstruction by Wilson et al., the connectivity of the TPB is greater than 90%. However in the ensembles from Chapter 3, the connectivity is

an order of magnitude lower. This is true for all Ni phase fractions tested, and for all particle size ratios tested. Consequently, the fidelity of the sphere-based reconstruction, with respect to the connectivity of the TPB, will be of particular interest.

4.3 Creating Cermet Data from Ion Beam Data

The first step in rendering this data into a sphere-based reconstruction is to put the data in the form of a locus of tagged points. Each point represents a location within the cermet and whether the phase present at that point is Ni, YSZ, or pore. This locus can be readily reconstructed from graphics files of the cross sections of the cermet. In the case of the FIB-SEM data the source data was in the form of '.tif' files. The '.tif' data from 82 separate sections were reinterpreted into one data object, where each pixel from the '.tif' files was used to set the location and type of a volume element, a voxel, within a 3-D structure. The voxels are then used to determine the type, size, and placement of spherical particles in a particle-based cermet model.

The FIB-SEM images are organized into 82 '.tif' files. Each '.tif' file represents one 2-D image of the cermet and can be read in MATLAB as an ordered 2-D array of pixel color data. The FIB-SEM data contains only three colors: white for Ni, 50/50 grey for YSZ, and black for void. The overall dimensions of the cermet in the x, y, and z directions are, respectively, $6 \times 5.2 \times 3.4$ μm. Each '.tif' file represents one x-y plane. In the x and y directions each file is 430×370 pixels. Based on these dimensions, the implied spacing of the pixels is $\delta x = \delta y = 14$ nm, and $\delta z = 42$ nm.

Because this method relies on placing spheres, it is better to have each voxel represent a cubic volume, as opposed to an asymmetric cuboid. One approach is to place extra points in the z-direction so that the z spacing matches the x, y spacing. This method allows all of the information contained within the original data structure to be preserved. The primary disadvantage of this approach is that the number of points to be
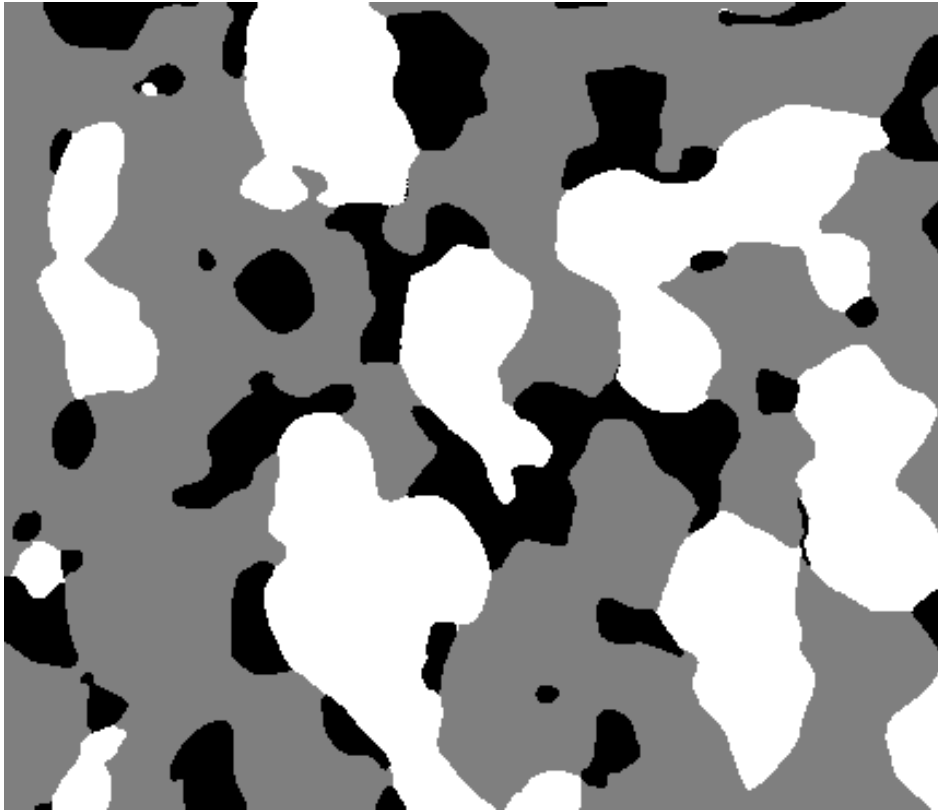
Figure 4.9: Focused ion beam data as a 'TIF' image (Ni: White, YSZ: Grey, Pore: Black)

processed is tripled. Given that the cermet calculations require a non-trivial amount of computation time, this is a serious disadvantage. A second approach is to use an simple averaging method to simplify the structure of the x-y slices. In this case, because 430 modulo 3 and 370 modulo 3 are both equal to 1, it is straightforward to reduce each 3 $\times$ 3 pixel section into a single pixel. The resulting image has a resolution of 143 $\times$ 123 pixels. The disadvantage of this method is that some of the fine detail of the original structure is lost. In this case, the type of the reduced pixel is determined by counting the types of the 9 original pixels and placing a pixel of the plurality type. The resulting coarsening of the image is demonstrated in Figure 4.10.

There is some loss of information and corresponding small change in the statistics of the cermet using this method of reduction. As an example in the original format with
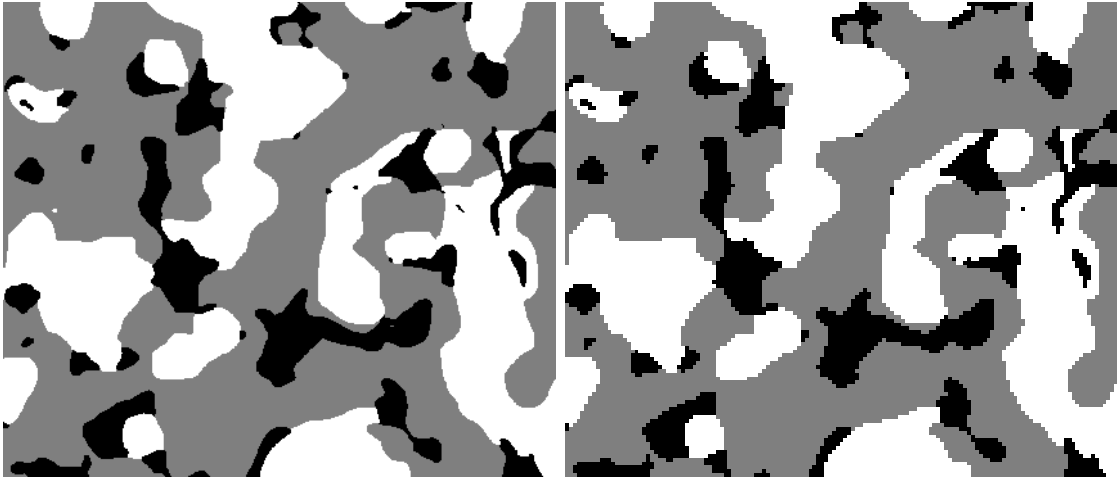
Figure 4.10: Comparison of original 430 × 370 FIB-based '.tiff' image image (left) and reconstructed 143 × 123 image '.tiff' (right)

12,887,100 voxel units, the volume fraction of each phase is:

1. YSZ fraction: 54.38%,

2. Ni fraction: 19.50%,

3. void fraction: 26.11%.

In the reduced format the number of voxels is 1,424,709, and the volume fraction of each phase is:

1. YSZ fraction: 54.29%,

2. Ni fraction: 19.86%,

3. void fraction: 25.85%.

Using this method 82 new '.tif' images are generated at the lower resolution, 143 × 123. In these reduced images, the implied distance between pixels in the x, y, and z directions are equal, that is, $\delta x = \delta y = \delta z = 42$ nm. The pixels in these images can be readily interpreted as cubic voxels in a 3-D structure. The next step is to translate

these voxels into a series of spheres. Note that the volume can equivalently be viewed as a lattice of equidistant cubes with a edge length equal to dx, or as a lattice of equidistant overlapping spheres with radius $\sqrt{2}\,\delta x$. The decision about the radii of the replacement spheres does impact the final geometry and the fidelity to the original cubic reconstruction. If the sphere radius is chosen such that the sphere contains the voxel, that is,

$$r = \frac{\sqrt{3}}{2}\delta x \ , \tag{4.1}$$

a cap-shaped volume will project in to the void space, distorting the geometry and reducing the volume of void space. Additionally, this choice increases the apparent surface area of the solid phases, and the calculated length of the TPB. For each solid phase voxel in contact with the void phase, the void volume is reduced by

$$\delta_v = \left(\frac{\sqrt{2}\pi - 3}{18}\right)\delta x^3 \ . \tag{4.2}$$

In this case, the void fraction of the sphere-based reconstruction will be smaller than the void fraction of the voxel-based reconstruction. At the 1 sphere per voxel level of reconstruction, this does not make a major difference in void fraction, but in other cases this distortion is significant. An alternative is to to make the volume of the spheres match the volume of the voxels. In this case the radii of the spheres are

$$r = \sqrt{n}\ \frac{3\ \delta x^3}{4\pi} \ . \tag{4.3}$$

This approach still changes the geometry of the boundaries between the void and solid phases as well as the geometry of the TPB, but preserves the void fraction and the relative solid fractions.

The formula of using 1 sphere per voxel results in a system with 1,424,709 spheres and similar number of TPB sections. Calculations with this many elements are computationally intensive. In order to make the calculations practical, we chose to reduce
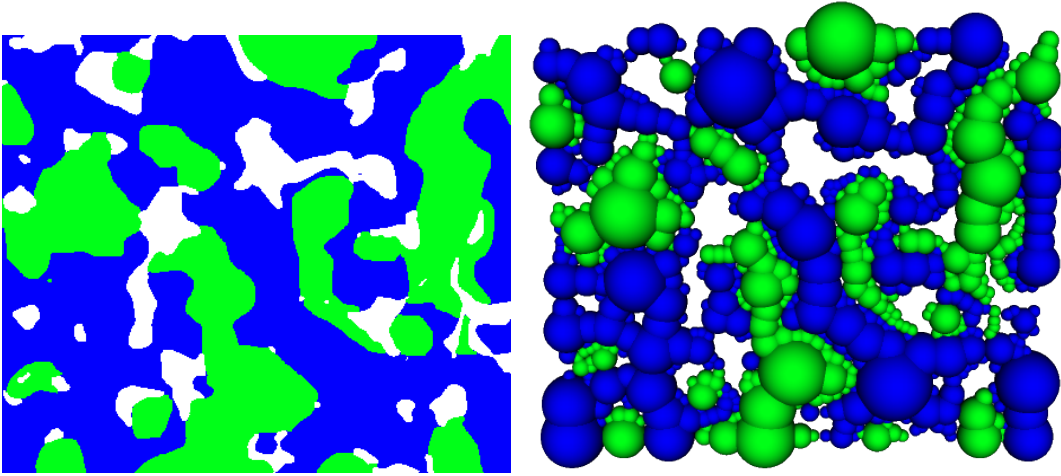
Figure 4.11: Image file and resulting particle array (Ni: Green, YSZ: Blue)

the complexity of the system while minimizing the loss of important information. The method we have chosen to reduce the complexity of the system is to allow groups of homogenous voxels, within a given neighborhood, to be represented by a single sphere. This is accomplished by sequentially considering each voxel. If the voxel represents either the Ni phase or the YSZ phase, the location of that voxel, $\bar{c}$, is considered as the center point of a sphere. The voxels in the neighborhood of $\bar{c}$ are then tested. For an integer value, $b \geq 0$, the neighborhood consists of all voxels for which the distance between that voxel and $\bar{c}$ is less than $b \cdot \delta x$. If all of the voxels within the neighborhood are of the same type, b, then the next step is a collocation test. If $\bar{c}$ is within the radius of an existing sphere, the process moves to the next voxel. At this point, a sphere of radius $b \cdot \delta x$ can be placed with center located at $\bar{c}$. This process is repeated until every voxel has been tested. Once every voxel has been evaluated, b is decremented and the process is repeated. This continues until $b = 1$. At this point, every voxel has been incorporated into a sphere. Figure 4.11 shows an example of a sphere-based structure based on a single frame from from a '.tif' file. The resulting cermet structure is shown in Figure 4.12.

Reconstructions of the three separate phases of the cermet: YSZ, Ni, and the void phase,

are shown from various angles in Figures 4.15, 4.16, 4.13, 4.14, 4.17, and 4.18.

The YSZ phase comprises more than 50% of the volume of the cermet section. While the details of the structure are not readily discernible from the images shown, the YSZ phase is the one phase that is nearly contiguous. Given that the YSZ phase represents more than half of the volume of the cermet, this is an expected result. In Chapter 3, we showed that, even in an essentially random particle ensemble, when 50% of the total volume was comprised of one phase, more than 99% of the volume within that phase was contiguous.

Only 19.6% of the cermet structure consists of Ni. The majority of the Ni phase comprises a single structure, although in some places the connection is limited to relatively narrow, neck structures. This is consistent with the idea, developed in Section 4.2.2, that the connectivity of Ni phase increases through sintering. This reconstruction confirms that the limiting Ni phase fraction for percolation is lower than the limit that would be suggested by modeling based on particle accumulation and overlap limits based on physical and mechanical calculation; this invalidates the use of spherical particle models in predicting the onset of percolation for the Ni phase.

The pore structure consists of the remainder of the cermet volume after the Ni and YSZ phases have been determined. Unlike the Ni and YSZ phases, the visualization of the void phase in Figures 4.17 and 4.18 does not represent exactly the volumes used in the calculations. Despite this, these visualizations still indicate the overall structure of the pore phase. Though the volume of the pore phase is actually greater than that of the Ni phase, the pore phase is the least connected of the three phases.

Table 4.1 gives the distribution of particle sizes resulting from the cermet reconstruction. The distribution is quite different from the empirical measurements presented by Cho, but it is qualitatively similar to the results presented by Chiu. The connectivity between particles is detailed in terms of the coordination numbers of particles of various sizes in

Table 4.1: Particle distribution data for cermet reconstruction

Radius Ratio	r (nm)	Number of Particles	Number of YSZ Particles	Number of Ni Particles	% YSZ	% Ni	Nominal Volume (μm^3)
2	85	17945	12139	5806	67.6%	32.4%	1.650
3	127	4969	3290	1679	66.2%	33.8%	1.542
4	169	1871	1197	674	64.0%	36.0%	1.376
5	211	761	426	335	56.0%	44.0%	1.093
6	254	300	182	118	60.7%	39.3%	0.7448
7	296	127	92	35	72.4%	27.6%	0.5007
8	338	32	18	14	56.3%	43.8%	0.1883
9	380	10	7	3	70.0%	30.0%	0.0838
10	423	6	3	3	50.0%	50.0%	0.0690
11	465	1	1	0	100.0%	0.0%	0.0153

Tables 4.2 through 4.11. Two points are immediately observable:

1. The patterns of the inter-particle connections have only a small variation based on the phase of the particle. There is a very similar pattern of connections for both Ni and YSZ particles.

2. The pattern of inter-particle connections can be broken into three distinct groupings. These groupings are based on the size of the particles:

   (a) particles in the range from 85 nm to 169 nm,

   (b) particles in the range from 211 nm to 296 nm,

   (c) particles in the range from 338 nm to 465 nm.

The smallest particles of the reconstruction, from 85 nm up to 169 nm, display several important characteristics. The majority of particles of these sizes, $\geq$ 94%, are only connected to particles that are one size larger or one size smaller. Also, these particles are most commonly connected to particles of the same size. These attributes are readily discernible in Figures 4.20 and 4.19.

The coordination numbers show that these particles are mainly in contact with particles of the same phase. For example, examining the coordination numbers of 85 nm particles,

$Z_{YSZ} = 12.27$. $Z_{YSZ-YSZ} = 9.52$; 75% of the connections to YSZ particles are YSZ-YSZ connections. YSZ particles are 67.6% of all particles, so a high percentage of YSZ-YSZ connections is expected. However, the same pattern emerges for the less abundant Ni particles (32.4% of the total). For 85 nm Ni particles, $Z_{Ni} = 10.48$. $Z_{Ni-Ni} = 9.17$; 87.5% of the neighboring particles are of the same phase. This pattern is repeated for particles of 127 nm and 169 nm. For particles in the 85–169 nm range, which make up a significant portion of the total non-void volume, the phase distribution is not random. Self-agglomeration is strongly favored, particularly in the Ni phase. This agrees with the observations from Section 4.2.

The second defining characteristic for particles with radii in the range of 85–169 nm, was the strong tendency of these particles to be connected only to particles of the same diameter. 98% of 85 nm particles are connected to other 85 nm particles. For 127 and 169 nm particles the percentages of particles connected to particles of the same size are 85% and 64%, respectively. This occurs because these particles form mainly sheetlike structures. These structures have a characteristic thickness defined by the diameter of the particle, and consequently they are formed from many particles of the same diameter. By comparing Figure 4.19, which consists of only 28 nm Ni phase particles, with Figure 4.15, which consists of all Ni particles, one can see that in many cases these sheets are not free standing structures, but rather serve as the boundaries of larger structures.

Particles in the range from 211 nm to 338 nm have a significantly different connection profile, as shown in Figure 4.21. Despite the difference in particle size, the connection profiles for particles from sizes 254 nm to 338 nm are virtually identical. These particles are most often connected to particles of 169 and 211 nm with coordination numbers around 2.8 and 4, respectively. From there, the coordination numbers for larger size particles falls off to nearly zero for particles with a radius of of 380 nm. Particles of 211 nm show a moderate deviation from this pattern. For completeness, these coordination

numbers are presented in graphical form in Figure 4.22.

There are very few particles of size 380 nm or larger in the reconstruction, only 17 out of 26022, including only one particle of radius 465 nm. There are few features within the cermet section larger than that size, and the distribution of coordination numbers is of limited value. These largest particles are mostly connected to particles within the 254–338 nm range, but no pattern is discernible.

The data associated with the reconstruction strongly indicates that there is degree of directional structure within the cermet which cannot be duplicated by random placement of particles. This is incompatible with the assumption that the structure is essentially random. This is important because the assumption of an essentially random distribution of phases within the cermet is the underlying assumption of the particle-based models previously presented in Chapters 2 and 3. One strong indication of this structure can be found in the nature of the connections between the reconstruction particles. For both types of particles used in the reconstruction, across all the size ranges used in the reconstruction, the Z_{i-i}/Z_i is greater than 70%. In a disordered system, the expectation would be that the relationship between Z_{i-i} and Z_i would be strongly related to the relative abundance of that type of particle. In this particular case, Z_{i-i}/Z_i would be close to 0.7 for the YSZ phase and closer to 0.3 for the Ni phase. The explanation for the lack of this behavior is that both phases have a tendency towards agglomeration. The Ni phase in particular has a very strong tendency to self-agglomeration. The Ni phase is almost entirely connected, despite its very low fraction of the total volume. This corroborates strongly with the fact that 94% the TPB of the original cermet was one continuous section [51]. This is also consistent with the behavior of the Ni in the PLD experiments demonstrated in Section 4.2.

4.4   Conclusions

In Section 3.6 we examined particle-based models of composite anodes using models based on the random packing of particles. For ensembles with monodispersed and simple polydispersed particle size distributions, these models were able to recover some of the qualitative behavior exhibited in experimental measurements. In particular, the sudden onset of percolation and the general behavior of the conductivity curve can be recovered. However, extending these models by introducing distributions of particle sizes based on experimental observations produced behavior that did not match those observed properties. One of the main assumptions of the particle-based models that have been presented in this work is that the geometric distribution of particles within the model should be essentially random. This follows directly from the manufacturing process, where precursor materials for the composite anode are typically thoroughly mixed. These models explicitly assumed that the compaction process does not produce a rearrangement of the particles that negates the assumption of an essentially random distribution. However, in Section 4.2 we have shown that at temperatures of 460–500°C the Ni phase is mobile. These temperatures are well below the temperatures experienced during the manufacture of a SOFC composite anode. More importantly, the movement of the Ni is not random, bringing into question the assumption that the manufacturing process would produce essentially random structure. From this we expressed three conjectures of how the mobility of the Ni phase would impact the overall percolation and conductive property of the composite anode:

1. The minimum Ni phase fraction required to achieve percolation and conductivity should be lower than expected.

2. The TPB density, in terms of length per unit volume, should be higher.

3. The TPB should be more connected.

In Section 4.3 we analyzed the structure of an actual SOFC composite anode. This analysis determined that the structure was indeed not random, and that the connectivity of the phases, particularly the Ni phase, is far greater than can be expected given the assumption of an essentially random structure. From this we conjecture that the expected percolation threshold of a composite anode should be lower than predicted from the types of models examined in Chapters 2 and 3. This conjecture cannot be proven, however without further experimental data.

In the experimental data presented in Chapters 2 and 3, the percolation threshold was greater than 20% Ni phase fraction (at least 21% under various manufacturing conditions for Huebner's data, and at least 25% for Dees'). In the case of the FIB-SEM reconstruction, percolation is achieved at 21% Ni phase fraction. Without more data focused on percolation when the Ni phase is between 20–25% it is not possible to make a strong conclusion that the onset of Ni percolation in real composite anodes occurs at a lower levels. Understanding the minimum required Ni phase fraction required for Ni percolation is important because, as shown by Sunde, optimum performance occurs when the minimum Ni phase fraction required for electronic conductivity from the anode–electrolyte interface is present in the system. This is because the conductivity of the Ni phase is 6 orders of magnitude higher than that of the oxide phase. This results in the Ni potential in a Ni-YSZ anode being constant with respect to the potential of the YSZ phase. In this situation, improving the conductivity of the Ni phase by increasing the Ni phase fractions does not result in any significant gains in electrochemical performance.
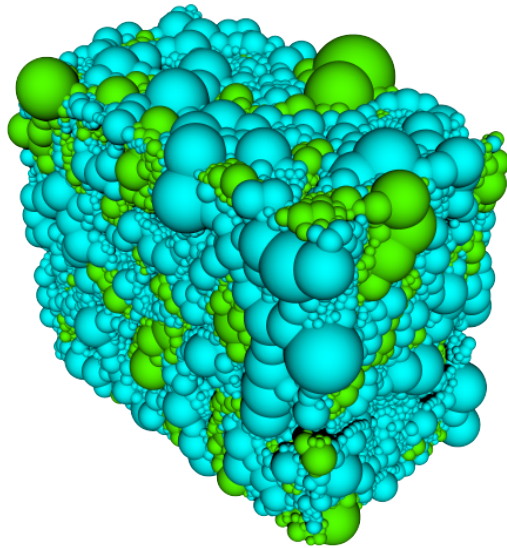
Figure 4.12: Particle-based reconstruction of cermet section from FIB data (Ni: Green, YSZ: Blue)
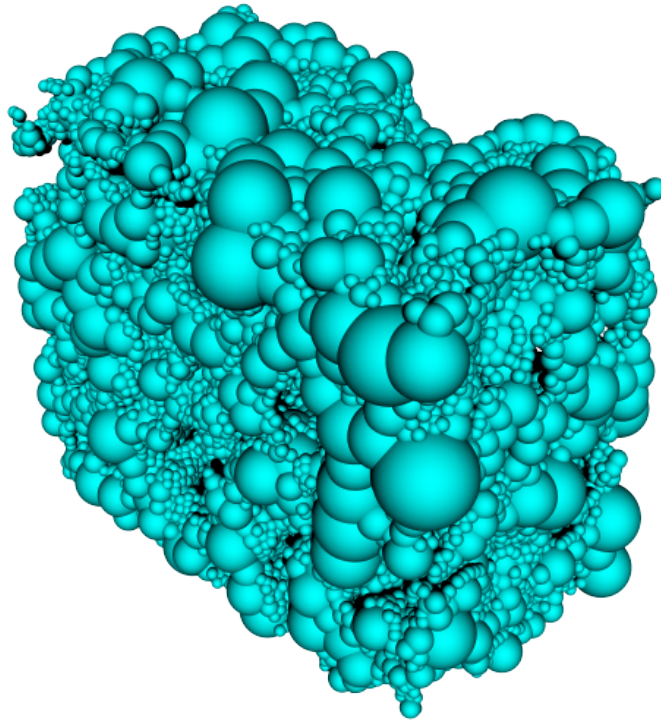
Figure 4.13: YSZ section of particle-based reconstruction of cermet section from FIB data
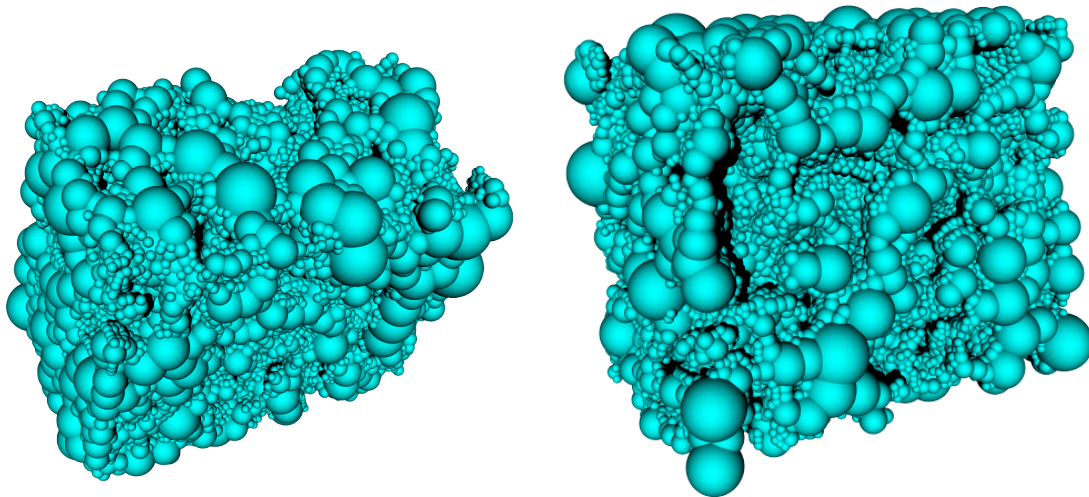
Figure 4.14: Multiple views of the YSZ section of particle-based reconstruction of cermet section from FIB data
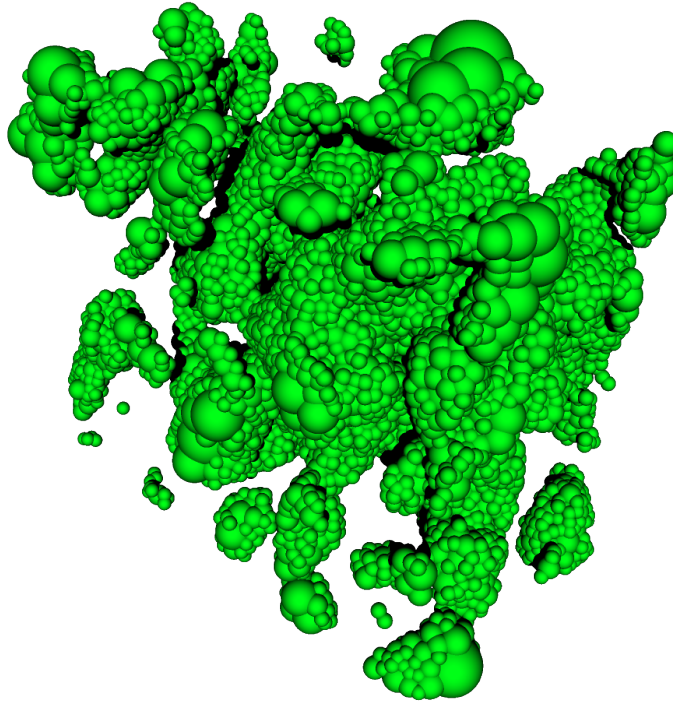
Figure 4.15: Ni section of particle-based reconstruction of cermet section from FIB data
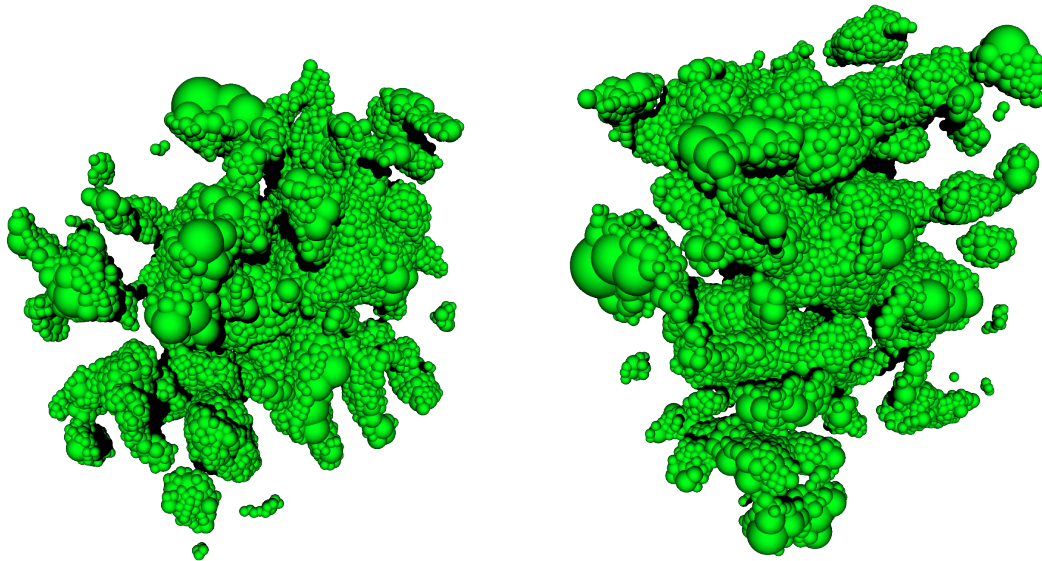
Figure 4.16: Multiple views of the Ni section of particle-based reconstruction of cermet section from FIB data
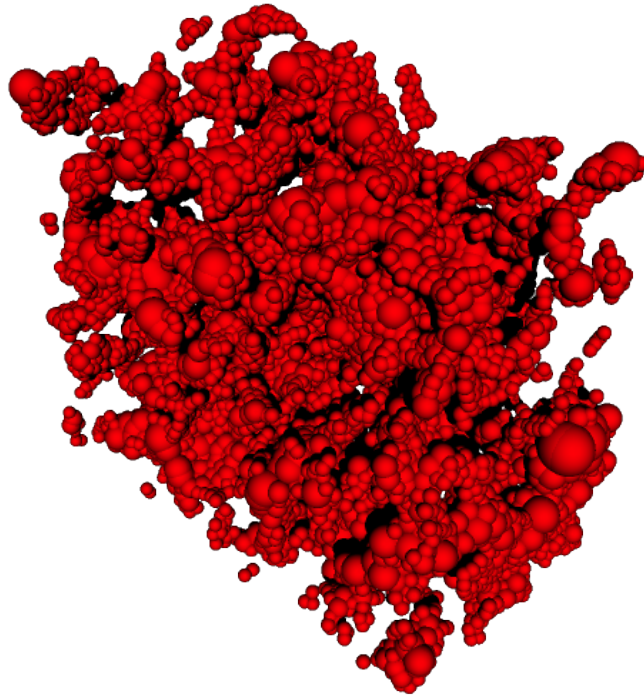
Figure 4.17: Particle reconstruction of the pore phase of particle-based reconstruction of cermet section from FIB data
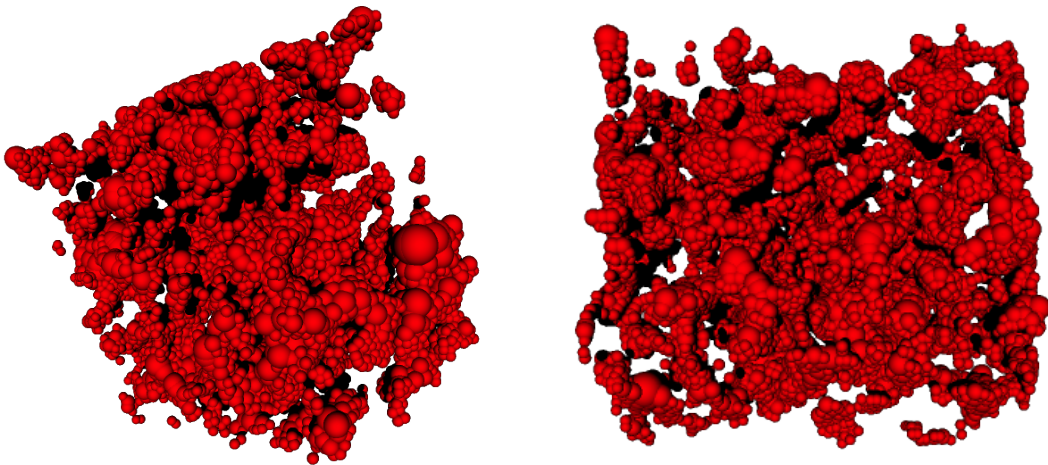
Figure 4.18: Multiple views of the particle reconstruction of the pore phase of particle-based reconstruction of cermet section from FIB data
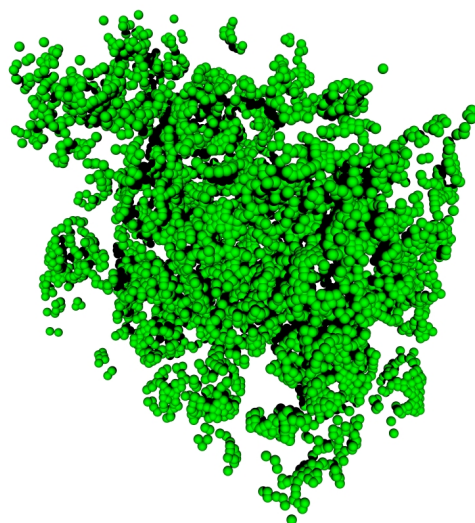
Figure 4.19: Nickel particles of size 85 nm through 169 nm
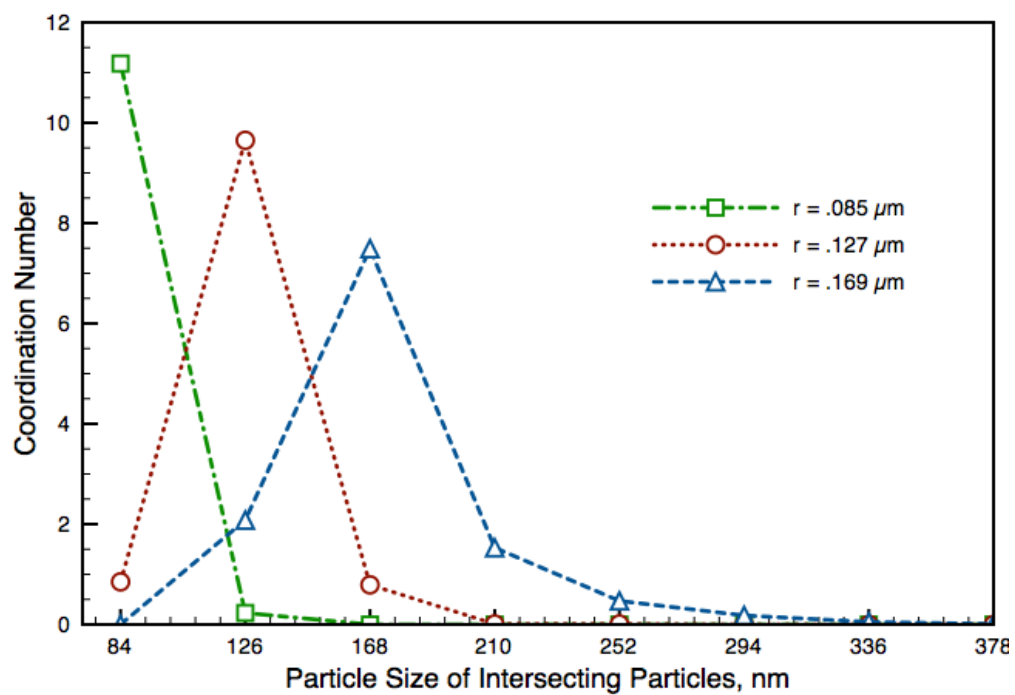
Figure 4.20: Coordination numbers for particles of size 85 nm through 169 nm
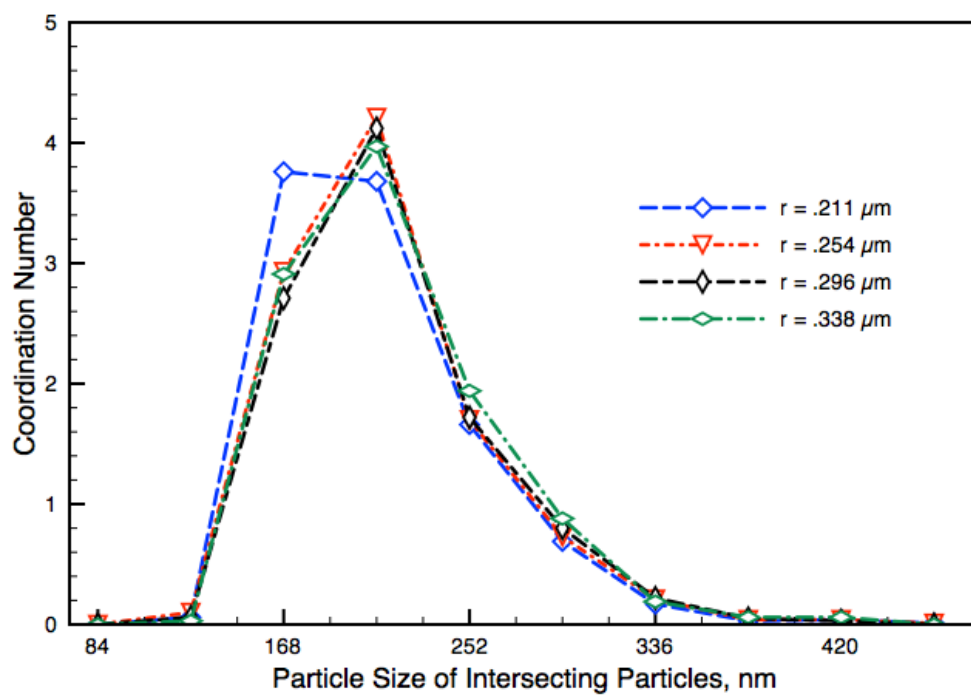
Figure 4.21: Coordination numbers for particles of size 211 nm through 338 nm
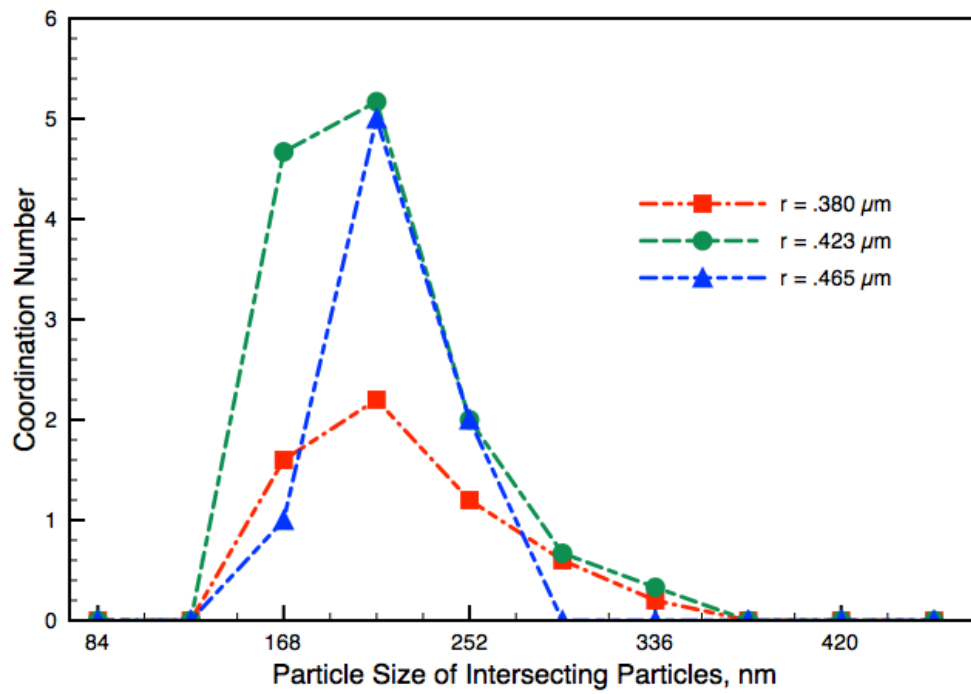
Figure 4.22: Coordination numbers for particles of size 380 nm through 465 nm

Table 4.2: Connection data for cermet reconstruction for 85 nm particles

r nm	Z	Z_{YSZ}	Z_{Ni}	$Z_{\text{Ni}-\text{Ni}}$	$Z_{\text{YSZ}-\text{YSZ}}$
85	11.18	10.83	11.91	9.17	9.52
127	0.23	0.24	0.22	0.16	0.21

Table 4.3: Connection data for cermet reconstruction for 127 nm particles

r nm	Z	Z_{YSZ}	Z_{Ni}	$Z_{\text{Ni}-\text{Ni}}$	$Z_{\text{YSZ}-\text{YSZ}}$
85	0.85	0.89	0.75	0.54	0.78
127	9.65	9.42	10.10	7.66	8.17
169	0.79	0.80	0.76	0.62	0.68
211	0.01	0.01	0.01	0.01	0.00
254	0.01	0.00	0.01	0.01	0.00

Table 4.4: Connection data for cermet reconstruction for 169 nm particles

r nm	Z	Z_{YSZ}	Z_{Ni}	$Z_{\text{Ni}-\text{Ni}}$	$Z_{\text{YSZ}-\text{YSZ}}$
127	2.08	2.06	2.13	1.54	1.86
169	7.49	7.33	7.77	5.87	6.26
211	1.53	1.48	1.62	1.26	1.14
254	0.47	0.46	0.49	0.42	0.40
296	0.18	0.22	0.12	0.07	0.20
338	0.05	0.05	0.04	0.04	0.04
380	0.01	0.01	0.01	0.01	0.01
423	0.01	0.02	0.00	0.00	0.02

Table 4.5: Connection data for cermet reconstruction for 211 nm particles

r nm	Z	Z_{YSZ}	Z_{Ni}	$Z_{\text{Ni}-\text{Ni}}$	$Z_{\text{YSZ}-\text{YSZ}}$
127	0.06	0.04	0.08	0.06	0.04
169	3.76	3.78	3.73	2.53	3.20
211	3.68	3.45	3.97	2.82	2.54
254	1.66	1.54	1.81	1.29	1.27
296	0.69	0.81	0.54	0.34	0.71
338	0.17	0.16	0.18	0.11	0.13
380	0.03	0.03	0.03	0.02	0.03
423	0.04	0.05	0.03	0.02	0.04
465	0.01	0.01	0.00	0.00	0.01

Table 4.6: Connection data for cermet reconstruction for 254 nm particles

r nm	Z	Z_{YSZ}	Z_{Ni}	Z_{Ni-Ni}	$Z_{YSZ-YSZ}$
127	0.10	0.03	0.19	0.19	0.03
169	2.93	2.91	2.96	2.39	2.64
211	4.21	3.92	4.65	3.66	2.96
254	1.70	1.64	1.79	1.36	1.36
296	0.73	0.82	0.58	0.41	0.71
338	0.21	0.16	0.28	0.25	0.13
380	0.04	0.04	0.03	0.03	0.04
423	0.04	0.05	0.02	0.02	0.04
465	0.01	0.01	0.01	0.00	0.01

Table 4.7: Connection data for cermet reconstruction for 296 nm particles

r nm	Z	Z_{YSZ}	Z_{Ni}	Z_{Ni-Ni}	$Z_{YSZ-YSZ}$
127	0.06	0.07	0.06	0.06	0.07
169	2.71	2.97	2.03	1.43	2.60
211	4.12	3.99	4.46	3.26	3.27
254	1.72	1.63	1.97	1.37	1.40
296	0.80	0.88	0.60	0.23	0.74
338	0.22	0.23	0.20	0.17	0.21
380	0.05	0.05	0.03	0.03	0.05
423	0.03	0.03	0.03	0.03	0.03
465	0.00	0.00	0.00	0.00	0.00

Table 4.8: Connection data for cermet reconstruction for 338 nm particles

r nm	Z	Z_{YSZ}	Z_{Ni}	Z_{Ni-Ni}	$Z_{YSZ-YSZ}$
127	0.03	0.06	0.00	0.00	0.06
169	2.91	2.61	3.29	1.86	2.39
211	3.97	4.17	3.71	2.71	3.00
254	1.94	1.44	2.57	2.14	1.28
296	0.88	1.11	0.57	0.43	1.06
338	0.19	0.17	0.21	0.14	0.11
380	0.06	0.06	0.07	0.07	0.00
423	0.06	0.11	0.00	0.00	0.06
465	0.00	0.00	0.00	0.00	0.00

Table 4.9: Connection data for cermet reconstruction for 380 nm particles

r nm	Z	Z_{YSZ}	Z_{Ni}	Z_{Ni-Ni}	$Z_{YSZ-YSZ}$
169	1.6	1.2	0.4	1.33	1.57
211	2.2	1.4	0.8	2.67	1.86
254	1.2	0.7	0.5	1.33	1
296	0.6	0.5	0.1	0.33	0.71
338	0.2	0	0.2	0.33	0

Table 4.10: Connection data for cermet reconstruction for 423 nm particles

r nm	Z	Z_{YSZ}	Z_{Ni}	Z_{Ni-Ni}	$Z_{YSZ-YSZ}$
169	4.67	8.00	1.33	0.67	7.67
211	5.17	6.00	4.33	2.67	5.67
254	2.00	2.67	1.33	0.67	2.67
296	0.67	1.00	0.33	0.33	1.00
338	0.33	0.33	0.33	0.00	0.33

Table 4.11: Connection data for cermet reconstruction for 465 nm particles

r nm	Z	Z_{YSZ}	Z_{Ni}	Z_{Ni-Ni}	$Z_{YSZ-YSZ}$
169	1.00	1.00	0.00	0.00	1.00
211	5.00	5.00	0.00	0.00	4.00
254	2.00	2.00	0.00	0.00	1.00

Chapter 5

Particle-Based Modeling with a Detailed Chemistry Model

Calculating SOFC performance using the models presented in Chapters 2, 3, and 4 does not account for the overpotential due to resistance to mass transfer within the porous electrode. Models accounting for these effects have been published by Zhu et al. [53] and Yong [24]. These models consider the mass transport through an 'averaged' porous medium. In these models it is assumed that all charge transfer reactions occur at the electrode–electrolyte boundary, neglecting any overpotential due to current. In this chapter we present a particle-based model which can account for mass transfer, heterogeneous chemistry, surface chemistry, and electrochemistry within a porous electrode.

5.1 Model Details

The model consists two two linked sub-models:

1. A network conduction model which accounts for the electronic and ionic currents in the solid matrix of the cermet.

2. A species model which solves the gas and surface phase species concentrations in the void phase and on the surface phases of the cermet, respectively.

The assumptions used are:

1. Occurance of charge transfer reactions at the TPB between dissimilar particles.

2. Negligible contact resistance between the porous electrode and the interconnect.

3. Negligible in-plane variation in gas phase species and surface coverages.

4. Negligible homogeneous gas phase chemistry.

5.1.1 Network Model

The flow of electrons and ions through the solid matrix is modeled with a network model which treats each particle within the system as a node in a network. Intersecting particles of the same type are treated as nodes connected by a resistor, where the resistance between particles is calculated using geometry and material properties. Intersections between particles of differing types are treated as nodes connected by a current source, where the current is determined by the local triple-phase boundary electrochemistry. The governing equations of the system are presented in Section 2.2.2.3 and the details of these calculations are presented in Section 2.4. For these calculations several modifications are necessary. In Chapters 2 and 3, the potential within a conducting phase is calculated using equation 2.28,

$$\nabla^2 \Phi = 0 \ . \tag{5.1}$$

An additional element of this model with respect to the earlier explanation of the network model is the addition of the Faradaic current, i_F, as a heterogeneous term. The boundary conditions for each phase are also different. The potential for each conducting phase is periodic in the x and y dimensions. At the electrode-electrolyte boundary,

$z = 0$, there is a von Neumann boundary condition for the electronically conducting phase, $\frac{\partial \Phi_e}{\partial z} = 0$, and a Dirichlet boundary for the ionically conducting phase, $\Phi_i = \Phi_0$. At the electrode-current collector boundary, $z = L_z$, there is a Dirichlet boundary condition for the electronic conducting phase, $\Phi_e = \Phi_1$, and a von Neumann boundary condition for the ionically conducting phase, $\frac{\partial \Phi_e}{\partial z} = 0$. With these boundary conditions the potential for the electronically conducting and ionically conducting phases is described by

$$
\begin{cases}
\nabla^2 \Phi_e = 0 \\
\frac{\Phi_e}{z}(x, y, z = 0) = 0 \\
\Phi_e(x, y, z = L_z) = \Phi_1 \\
\Phi_e(x = 0, y, z) = \Phi_e(x = L_x, y, z) \\
\Phi_e(x, y = 0, z) = \Phi_e(x, y = L_y, z) \\
\nabla^2 \Phi_i = 0 \\
\Phi_i(x, y, z = 0) = \Phi_0 \\
\frac{\Phi_i}{z}(x, y, z = 0) = \Phi_0 \\
\Phi_i(x = 0, y, z) = \Phi_i(x = L_x, y, z) \\
\Phi_i(x, y = 0, z) = \Phi_i(x, y = L_y, z) \ .
\end{cases}
\tag{5.2}
$$

The calculations for solving $\nabla^2 \Phi = 0$ within the context of a network model as illustrated in Figure 5.1 are detailed in Section 2.4.

Sunde and Schneider [47, 48, 42] have used simplified expressions or the Butler-Volmer [4] relation to determine the Faradaic current between heterogenous particles. The implicit assumption in using these types of relations is that the variation in both gas phase species and surface coverages is negligible in the electrochemically active region. In this model the Faradaic current between heterogeneous particles is calculated via an electrochemical reaction between the Ni and YSZ surface phases at each TPB. While any model is capable of using any model of detailed, elemental electrochemistry, for the
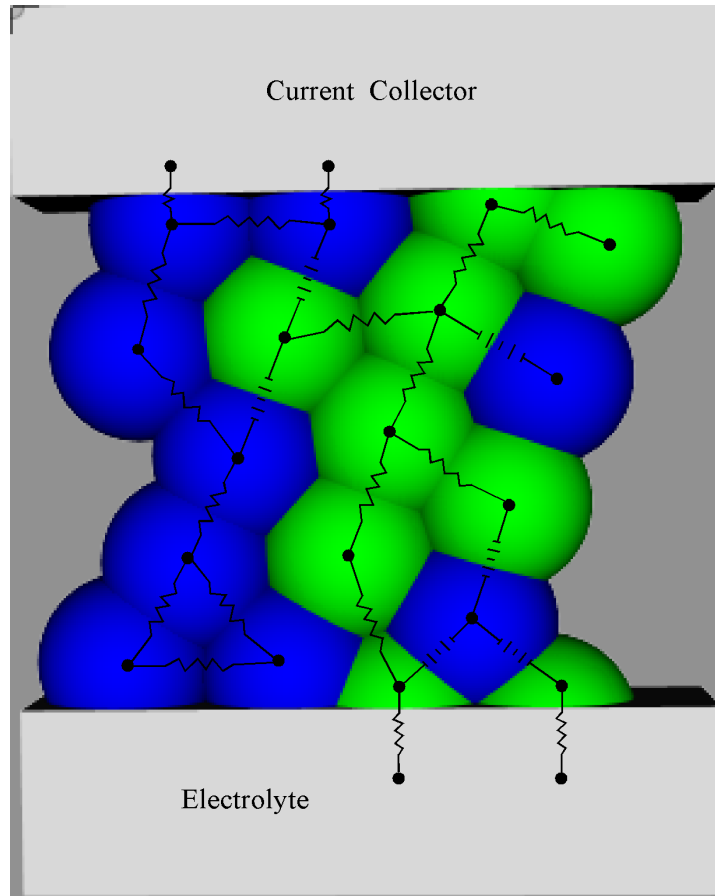
Figure 5.1: Illustration of the relationship between the resistor network model and the geometry of the composite cermet

cases presented here the mechanism is assumed to be:

$$H_{Ni} + O_{YSZ} \Longleftrightarrow Ni_{Ni} + OH_{YSZ} + e^-_{Ni} \tag{5.3}$$

$$H_{Ni} + OH_{YSZ} \Longleftrightarrow Ni_{Ni} + H_2O_{YSZ} + e^-_{Ni} \ . \tag{5.4}$$
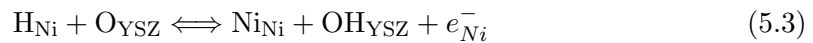
The activation energy (1 eV) and pre-exponential terms were fitted to match the data produced by Bieberle and Glaucker [7]. In this case the Faradaic current can be calculated directly from the net production rate of electrons. By using this approach it is possible to avoid the simplifying assumptions of uniform gas phase concentrations and surface coverages. The Faradaic current for a given phase is the sum of the production

rates of the charged species scaled by the charge number of the species, n and Faraday's constant, F:

$$i_{\mathrm{F}} = \sum_{i=1}^{\mathrm{N_{sp}}} \dot{\omega}_i \cdot n\mathrm{F} \ . \tag{5.5}$$

For the specific electrochemistry given in equations 5.3 and 5.4, the contribution to the Faradaic current for ionically conducting and electronically conducting particles is, respectively,

$$i_{\mathrm{F}_i} = \sum_{k}^{N_{\mathrm{TPB}}} [(\dot{\omega}_{\mathrm{O_{YSZ}}} \cdot -2F + \dot{\omega}_{\mathrm{OH_{YSZ}}} \cdot -F) \cdot l_{TPB}] \tag{5.6}$$

$$i_{\mathrm{F}_e} = \sum_{k}^{N_{\mathrm{TPB}}} \dot{\omega}_{\mathrm{e^-}} \cdot -F \cdot l_{TPB} \ . \tag{5.7}$$

5.1.2 Porous Transport Model

The species model is a one-dimensional model of the three phases active within the porous volume of the cermet:

1. The gas phase in the cermet void fraction.

2. The surface phase of the electron conductor.

3. The surface phase of the oxygen ion conductor.

The solution method for the one-dimensional porous transport model follows the approach introduced by Zhu et al. [53]. Within this model the steady state fluxes of the

gas phase species, J_k, satisfy

$$
\begin{cases}
\nabla \cdot J_k = A^s \cdot \dot{s}_k, \ k = 1, \ \ldots, \ N_{sp} \\
\qquad\qquad J_k(z = 0) = 0 \\
\qquad\quad Y_k(z = L_z) = Y_k^\infty \ .
\end{cases}
\tag{5.8}
$$

The active surface area, A^s for each surface phase is calculated directly by summing the surface area of the individual particles of each phase comprising the relevant section of the porous media. The details of these calculations are given in Section 2.3.3.5. The molar fluxes are calculated by Cantera based on the implicit relation

$$
\sum_{j \neq k} \frac{X_j J_k - X_k J_j}{D_{kj}^e} + \frac{J_k}{\mathcal{D}_{k,\mathrm{Kn}}^e} = -\nabla C_k - \frac{C_k}{\mathcal{D}_{k,\mathrm{Kn}}^e} \cdot \frac{b}{\mu} \nabla p \ .
\tag{5.9}
$$

The molar production rates from heterogenous chemistry between the gas phase and the surface phases are calculated with Cantera using the mechanism published by Zhu et al. [53] (Table 5.1). The net activation energies of reactions 12, 2, 21, and 23 depend on the CO(s) coverage, $\theta_{\mathrm{CO(s)}}$, in the form

$$
k = A T^n \exp\left(-\frac{E}{RT}\right) \exp\left(-\frac{\epsilon_{\mathrm{CO(s)}} \theta_{\mathrm{CO(s)}}}{RT}\right) \ .
\tag{5.10}
$$

The effective knudsen diffusion coefficients, which take into account the effects of collisions of the gas-phase molecules with the wall is calculated as

$$
\mathcal{D}_{k,\mathrm{Kn}}^e = \frac{2}{3} \frac{r_{pore} \ \phi}{\tau} \left(\frac{8 R_u T}{\pi W_k}\right)^{1/2} , \ \ R_u = 8.314 \ \mathrm{J \cdot mol^{-1} \cdot K^{-1}} \ .
\tag{5.11}
$$

The permeability, b, and the molar fluxes depend on the physical properties of the porous media: mean pore radius, tortuosity, mean particle diameter. These parameters are estimated via a TPMC method as detailed by Hanna [23]. TPMC is used to compute the motion of representative molecules in the gas flow through a porous structure. Details of the TPMC method are given in detail in Section 2.3.3.6. Using these calculations the permeability, b, is calculated via the Kozeny-Carman [5] relation as

$$b = \frac{\phi r^2}{18\tau(1-\phi)^2} \tag{5.12}$$

For each of the surface phases the coverage of the k-th surface phase species satisfy

$$\frac{\partial \theta_k}{\partial t} = \frac{\dot{\omega}_k}{S_0} \cdot n_k^s . \tag{5.13}$$

The steady state surface coverages then satisfy

$$0 = \frac{\dot{\omega}_k}{S_0} \cdot n_k^s . \tag{5.14}$$

Electrochemical reactions at the TPB contribute to the net production rates, ω. For each finite volume within the one-dimensional porous media model the production rates from each TPB are calculated separately using the potential difference between each heterogenous particle pair. These production rates are then scaled by the length of the appropriate TPB segment, summed, and then the sum rescaled by the surface area of the surface phase

$$\dot{\omega}_{k,\text{TPB}} = \frac{\left(\sum_{i=1}^{N_{\text{TPB}}} \dot{\omega}_i \cdot l_{TPB}\right)}{A^s} . \tag{5.15}$$

5.1.3   Results

We consider the case of a thin electrode (25 μm thick electrode operating at 800∘C with a 1 atmosphere boundary gas flow mixture with $X_{\text{H}_2} = 0.98$ and $X_{\text{H}_2O} = 0.02$. In Table 5.2 and Figure 5.2, the spatial distribution of the Faradaic current, i_F is shown. Within this solution the both the distance from the gas phase boundary, 25 μm, and the tortuosity of porous structure, 2.2, are low. Consequently, the gas phase concentrations are nearly constant throughout the geometry. From this we expect the Faradaic current to be dominated by the potential differences at the triple phase boundaries, as opposed to the local chemistry. In order gradients in the gas phase concentration play a greater role, cases with a significantly longer z dimension and/or greater tortuosity would have to be examined. Unfortunately, we are unable to present such cases in this work. The Faradaic currents are calculated for each heterogenous particle pair. Because the TPBs are not continuously distributed, i_F is not calculated as a continuous function of z. For Table 5.2 and Figure 5.2 the faradaic currents generated within a given z region of the electrode are summed. The spatial distribution of the Faradaic currents obey a power law relationship of the form

$$i_\text{F}(z) \propto e^{-2.40} \tag{5.16}$$

For this case the R^2 value is .976.

Table 5.2: Faradaic Current Density by geometric region

z μm	Faradaic Current A $\cdot$ cm^{-3}	Fraction	Cumulative Fraction
0.0-0.76	10125	0.479	0.479
0.76-1.18	6012	0.284	0.763
1.18-1.64	3300	0.156	0.919
1.64-2.33	1023	0.0484	0.967
2.33-2.92	629	0.0297	0.997
2.92-5.00	65	0.00308	1.000
5.00-25.00	4	0.000191	1.000

In the simple case where it is assumed that all TPB electrochemistry occurs at the
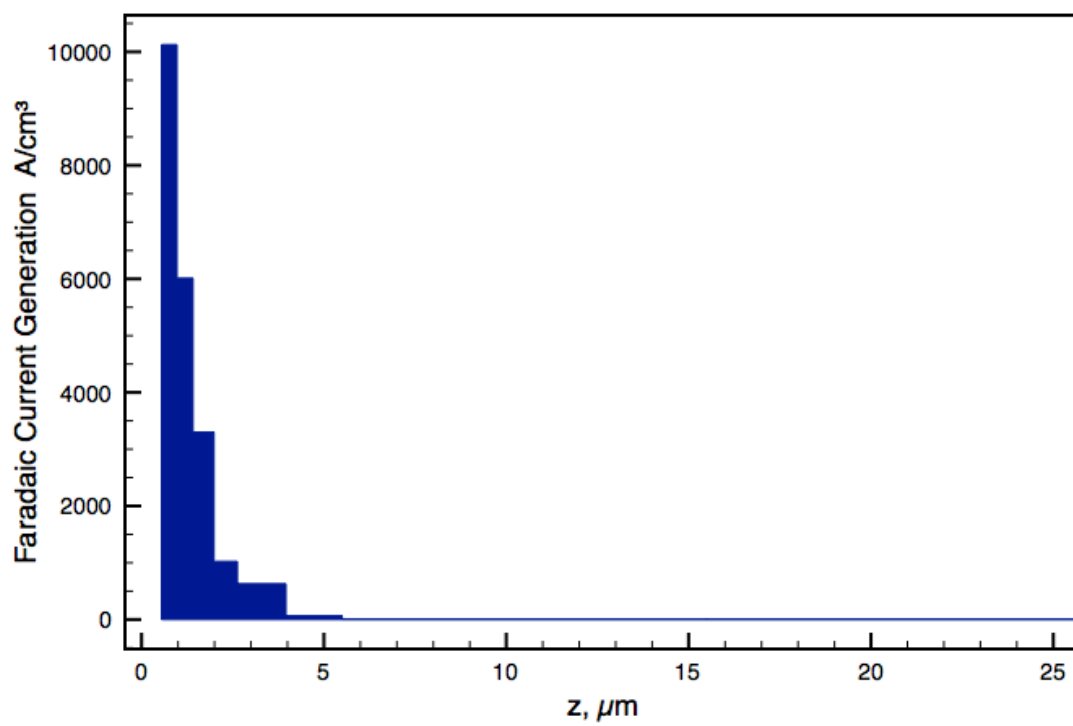
Figure 5.2: Histogram of Faradaic Current Generation as a Function of Distance from the Electrode-Electrolyte Boundary

electrolyte interface, there is an ionic current through the electrolyte which is equal in magnitude and direction to the electronic current through the anode. In this model, where TPB chemistry can occur throughout the electrode, the results are different. This is illustrated in Figure 5.3. The ionic current at the electrode-electrolyte boundary is equivalent to the ionic current in through the electrolyte. In the anode the ionic current decreases to nil at the anode-current collector boundary. From the electrode-electrolyte boundary to the electrode-current collector boundary the electronic current increases from zero at the electrode-electrolyte boundary to a value equal to to the ionic current through the electrolyte. The magnitude of the rate of change in both the the electronic and ionic currents in the are equal to the Faradaic current at the point within the anode. In fact the electronic current density can and should be view as the cumulative sum of the Faradaic current in the z direction.
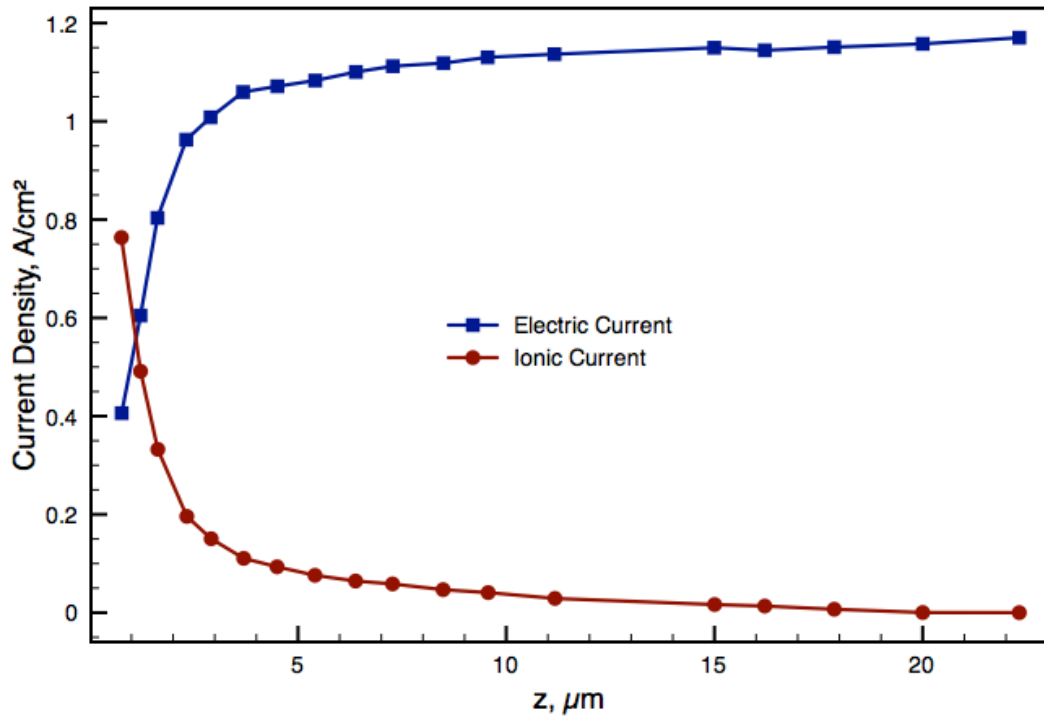
Figure 5.3: Electronic and Ionic Current Density as a Function of Distance from the Electrode-Electrolyte Boundary

These results also visualized in Figure 5.4. Figure 5.4 the electrolyte interface is to the left of the images and the gas phase boundary and current collector or electrode interface are at the right. In the top image the cermet particles are distinguished by type: blue for YSZ particles and gold for Ni particles. In the third picture the particles are colored by potential. Because the resistivity of the Ni phase is several orders of magnitude lower than that of the YSZ phase, the Ni phase particles have no visible differentiation in potential. The YSZ particles show considerable variation from the electrolyte potential (blue) to a potential differing from the electrode potential by the local half-cell open circuit potential. The second image clarifies this by removing the Ni particles. It is also easier to discern the groups of isolated YSZ particles as they show up as green in the image. These represent particles not connected to the larger ionic conduction paths to the electrolyte. This effect occurs because there can be no net Faradaic current without a both an electronically conducting pathway to transport the electrons to the current collector (electrode) and an ionically conducting pathway to transport the oxygen ions to the electrolyte surface. As can be seen in both the second image and the Faradaic current in the graph at bottom, the most intense volume of electrochemical activity is within 5 μm of the electrolyte interface. This extent of this volume can vary with the partial pressures of hydrogen and water, the relative abundance of Ni and YSZ particles, and the applied bias, but for the preliminary cases considered so far, the electrochemically active region remains within 15 μm of the electrolyte surface. This result has implications for anode design, as it directly implies that the design of the anode beyond this depth should be optimized to maximize fuel availability to the electrochemically active region, whether by reducing diffusion resistance for hydrogen fuel feeds or maximizing hydrogen production for hydrocarbon feeds.

We have been limited to showing only a single set of results from this model. The results for this case do show the significance and the value of calculating the distribution of the TPB electrochemistry even in a case where the variation in gas and surface species
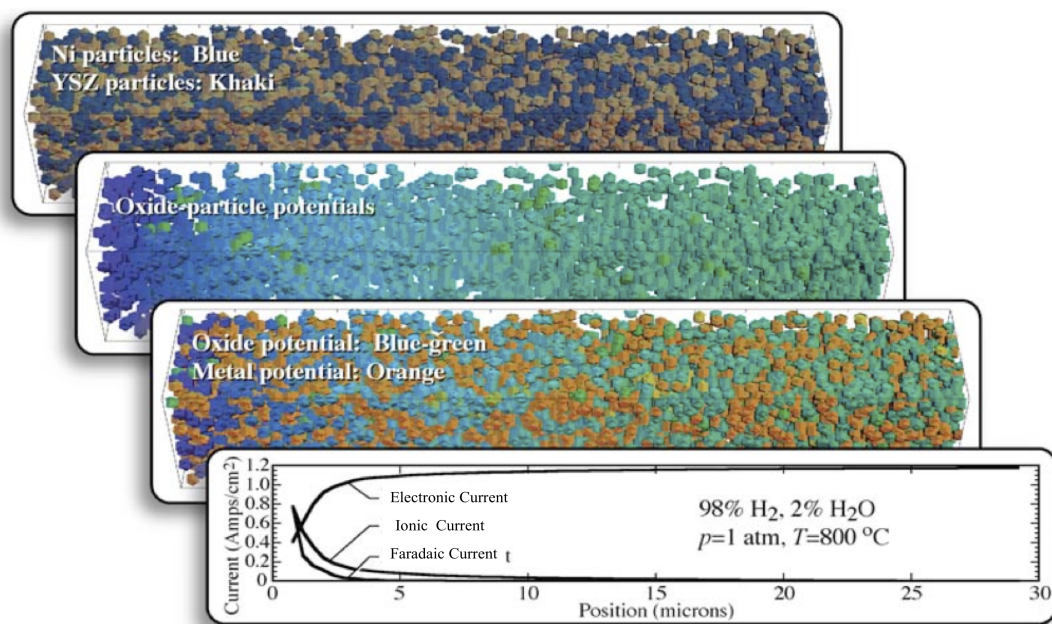
Figure 5.4: Structure, potentials, and current densities of particle-based cermet system with detailed chemistry

concentrations are minimal. It would be far more useful to generate full sets a data across a range of operating conditions and geometrical configurations. In particular cases, with higher tortuosity and a longer electrolyte to current collector distance measured across the full range of operating potentials would allow for the calculation of the impact of mass transport limitations on electrode performance.

Conclusion

There have been a number of efforts to model the behavior of fuel cells. Of particular interest here are those models of the Ni-YSZ system based on the random packing of particles within the cermet [1, 42, 43, 47]. These models have shown good agreement with experimental results in terms of cermet conductivity and polarization resistance [48]. Using these models it is possible to explore the overpotential associated with the porous anodes' resistance to both electronic and ionic current. These models, however, do not account for the overpotential due to resistance to mass transfer within the porous electrode. Models accounting for these effects have been published by Kee et al. [53] and Yong [24]. These models consider the mass transport through an 'averaged' porous medium. In these models it is assumed that all charge transfer reactions occur at the electrode–electrolyte boundary, neglecting any overpotential due to current.

In this work we examined the fundamental assumptions underlying these composite anode models. In doing so we discovered that the existing models understated the complexity of the composite electrodes in ways that strongly impacted the ability of such models to produce useful results across a wide range of geometrical configurations. In Chapter 3 we showed that a more realistic and necessarily more complex approach to the physical arrangement of phases within the composite electrodes is required in order to capture key information relating to the electronic and ionic conductivity of various phases.

The initial model, presented in Chapter 2, was based on an essentially random collection

of particles using both a monodispersed particle size distribution and a simple polydispersed particle size distribution based on using differing particle sizes for the Ni and YSZ phases based on phenomenological arguments. Single phase conductivity through these particle structures was calculated based on the geometry of inter-particle connections. This approach was validated by showing that the potential distribution across the particle structure using this approach is close to the potential distribution obtained by using FEM calculation with a finer resolution. In addition we showed that the electronic conductivity and other qualitative features of actual Ni-YSZ composites, such as percolation threshold, were reproduced. The TPB boundaries are calculated, and we showed that the proportion of the TPB available for electrochemical reactions depends strongly on the relative phase fractions. However, the utility of these idealized particle size distributions is limited. In particular, the percolation thresholds are not identical to those of actual Ni-YSZ composites, and the relationship between the percolation threshold and Ni:YSZ particle size ratio is the opposite of the observed relationship in actual Ni-YSZ composites.

The actual structure of Ni-YSZ composite cermets is not accurately reproduced by either monodispersed or simple polydispersed particle distributions. This is true whether we consider the size distributions of precursor particles or in situ measurements of particle agglomerates in sintered cermets. We developed Ni-YSZ particle systems based on experimentally measured size distributions of precursor particles continuing to use an essentially random spatial distribution of the resulting particles.

Given the shortcomings in the predictive performance of particle-based models, in Chapter 4 we explored how the structure within a composite Ni-YSZ anode precludes the assumption that the distribution of particles is essentially random. First we experimentally examined the behavior of Ni in contact with YSZ at elevated temperatures. Ni was applied via pulsed laser deposition to a heated YSZ substrate (460–500°C). SEM images showed that the Ni phase demonstrated both high mobility and a high surface

tension which resulted in self-aggregation of the Ni on the surface of the YSZ. This clearly demonstrated that the assumption that the Ni phase can be modeled as spherical particles which are only slightly deformed from the initial precursor state does not reflect the actual morphology of the Ni phase in a sintered Ni-YSZ cermet.

We also gained an understanding of the complexities of the Ni-YSZ composite system by examining the experimentally determined structure of a composite anode section in Section 4.3. This was accomplished using a sequence of images which show the internal structure of a representative SOFC anode. To create these images, a thin layer of the electrode is milled via a dual-beam focused ion beam between each image. This pioneering work was published by Wilson et al. [51], and the original image files were shared for this project. Using this data we developed a particle-based representation of the reconstruction, and compared the physical characteristics of the particle-based system to the original system. While the physical structure can be approximated by a sphere collection, the size distribution of the particles does not have a strong relationship to known characteristics of precursor particles. More importantly, the structure of the cermet, in terms of the spatial distribution of particles, cannot be considered random. Further, the geometric distribution and connectedness of the TPB in the reconstruction were not reproduced to any significant degree of accuracy.

Calculating SOFC performance using the models presented in Chapters 2, 3, and 4 does not account for the overpotential due to resistance to mass transfer within the porous electrode. Models accounting for these effects have been published by Zhu et al. [53] and Yong [24]. These models consider the mass transport through an 'averaged' porous medium and assume that all charge transfer reactions occur at the electrode–electrolyte boundary. In Chapter 5 we presented a particle-based model which does account for mass transfer, heterogeneous chemistry, and electrochemistry within a porous electrode. In particular, it is possible to directly calculate the physical properties impacting the gaseous transport, such as the tortuosity and mean particle diameter, for the particular

ensemble, rather than using estimates. As explored in Chapter 5, this model utilizes a monodispersed particle size distribution, physical property calculations developed by [23], the DGM [35], and a heterogenous chemistry model by Zhu et al. [53]. In addition, electrochemistry is calculated using a detailed model based on spatially local surface coverages and gas phase concentrations near the TPB. Preliminary results for this model are presented.

In order to improve the validity and usefulness of the types of models presented in this work, a number of challenges must be overcome. A better understanding of the physical structure of Ni-YSZ composites must be developed in order to develop a methodology which can generate mathematical structures which are reasonable analogous to the physical systems. The physical processes involved the manufacture of composite anodes lead to a high degree of phase separation. It is important to develop modeling frameworks which correctly emulate this behavior. In addition, better methods of approximating the correct TPB characteristics are needed. It may not be practically possible for a particle-based method to approximate physically realistic TPB geometry without using high levels of resolution which could produce computationally impractical systems. In that case it would be necessary to develop reasonable empirical approximations for TPB characteristics.

Appendix A

Data from Composite Anode Models

A.1 Monodispersed Systems (Type A)

Table A.1: Ni phase fraction and particle count for type A systems as a function of system size, L/r

L/r	λ	Mean Nickel Phase Fraction	Standard Deviation	σ/μ	Mean Number of Nickel Particles	Standard Deviation	σ/μ
12	0.965	0.383	0.0110	2.88%	507	15.0	2.96%
16	0.965	0.385	0.00412	1.07%	1201	14.1	1.18%
20	0.965	0.382	0.00689	1.81%	2327	33.5	1.44%
24	0.965	0.381	0.00599	1.57%	3992	60.8	1.52%
28	0.965	0.384	0.00757	1.97%	6391	79.2	1.24%
32	0.965	0.383	0.00713	1.86%	9535	53.9	0.57%
12	0.97	0.379	0.00967	2.55%	499	13.7	2.74%
16	0.97	0.382	0.00811	2.12%	1190	20.1	1.69%
20	0.97	0.378	0.00941	2.49%	2291	40.6	1.77%
24	0.97	0.378	0.00520	1.37%	3960	30.7	0.78%
28	0.97	0.377	0.00432	1.14%	6277	42.7	0.68%
32	0.97	0.377	0.00630	1.67%	9358	74.7	0.80%

Table A.2: Ni phase fraction and particle count for type A systems as a function of system size, L/r (continued)

L/r	λ	Mean Nickel Phase Fraction	Standard Deviation	σ/μ	Mean Number of Nickel Particles	Standard Deviation	σ/μ
12	0.975	0.376	0.0105	2.80%	492	13.0	2.64%
16	0.975	0.372	0.00670	1.80%	1152	17.9	1.55%
20	0.975	0.375	0.00725	1.93%	2268	30.2	1.33%
24	0.975	0.373	0.00632	1.69%	3894	46.7	1.20%
28	0.975	0.377	0.00569	1.51%	6181	51.6	0.84%
32	0.975	0.375	0.00671	1.79%	9221	70.0	0.76%
12	0.98	0.371	0.00995	2.68%	486	12.9	2.65%
16	0.98	0.371	0.00680	1.84%	1137	20.0	1.76%
20	0.98	0.374	0.00830	2.22%	2231	29.1	1.30%
24	0.98	0.373	0.00513	1.38%	3833	53.8	1.40%
28	0.98	0.372	0.00472	1.27%	6107	41.6	0.68%
32	0.98	0.365	0.00434	1.19%	9057	59.6	0.66%
12	0.985	0.371	0.0138	3.71%	483	17.7	3.67%
16	0.985	0.368	0.00928	2.52%	1131	30.6	2.71%
20	0.985	0.369	0.00855	2.32%	2190	22.7	1.04%
24	0.985	0.370	0.00586	1.58%	3781	34.1	0.90%
28	0.985	0.365	0.00480	1.32%	6008	59.6	0.99%
32	0.985	0.368	0.00588	1.60%	8970	68.2	0.76%
12	0.99	0.355	0.0130	3.67%	462	12.1	2.63%
16	0.99	0.360	0.0119	3.31%	1105	34.9	3.16%
20	0.99	0.365	0.00681	1.87%	2170	34.8	1.60%
24	0.99	0.363	0.00585	1.61%	3725	61.8	1.66%
28	0.99	0.363	0.00495	1.36%	5897	52.4	0.89%
32	0.99	0.363	0.00546	1.50%	8823	62.5	0.71%
12	0.995	0.365	0.0124	3.41%	471	13.7	2.91%
16	0.995	0.361	0.00987	2.74%	1100	22.3	2.03%
20	0.995	0.360	0.00673	1.87%	2136	18.8	0.88%
24	0.995	0.360	0.00554	1.54%	3689	32.2	0.87%
28	0.995	0.357	0.00508	1.42%	5805	30.2	0.52%
32	0.995	0.357	0.00460	1.29%	8633	46.2	0.54%

Table A.3: YSZ phase fraction and particle count for type A systems as a function of system size, L/r

L/r	λ	Mean YSZ Phase Fraction	Standard Deviation	σ/μ	Mean Number of YSZ Particles	Standard Deviation	σ/μ
12	0.965	0.383	0.0119	3.11%	510	16.7	3.27%
16	0.965	0.383	0.00629	1.64%	1197	14.0	1.17%
20	0.965	0.386	0.00593	1.54%	2352	33.6	1.43%
24	0.965	0.386	0.00449	1.16%	4069	61.3	1.51%
28	0.965	0.383	0.00694	1.81%	6391	76.6	1.20%
32	0.965	0.385	0.00646	1.68%	9526	58.6	0.62%
12	0.97	0.380	0.0102	2.69%	502	11.7	2.34%
16	0.97	0.376	0.00460	1.22%	1173	18.6	1.59%
20	0.97	0.383	0.00928	2.42%	2308	39.9	1.73%
24	0.97	0.380	0.00523	1.38%	3976	33.2	0.84%
28	0.97	0.380	0.00384	1.01%	6305	47.9	0.76%
32	0.97	0.380	0.00383	1.01%	9393	75.6	0.80%
12	0.975	0.374	0.0107	2.86%	494	13.9	2.81%
16	0.975	0.379	0.00750	1.98%	1176	17.8	1.52%
20	0.975	0.376	0.00635	1.69%	2261	29.3	1.30%
24	0.975	0.378	0.00768	2.03%	3919	50.1	1.28%
28	0.975	0.375	0.00677	1.81%	6199	53.9	0.87%
32	0.975	0.376	0.00537	1.43%	9238	69.0	0.75%
12	0.98	0.371	0.0116	3.14%	485	12.9	2.65%
16	0.98	0.372	0.00652	1.76%	1152	20.1	1.74%
20	0.98	0.371	0.00708	1.91%	2227	21.8	0.98%
24	0.98	0.374	0.00722	1.93%	3853	52.0	1.35%
28	0.98	0.371	0.00348	0.94%	6085	37.3	0.61%
32	0.98	0.375	0.00550	1.47%	9122	58.5	0.64%

Table A.4: YSZ phase fraction and particle count for type A systems as a function of system size, L/r (continued)

L/r	λ	Mean YSZ Phase Fraction	Standard Deviation	σ/μ	Mean Number of YSZ Particles	Standard Deviation	σ/μ
12	0.985	0.363	0.0162	4.46%	473	19.5	4.14%
16	0.985	0.368	0.0110	3.00%	1125	30.4	2.70%
20	0.985	0.366	0.00662	1.81%	2198	20.3	0.92%
24	0.985	0.366	0.00593	1.62%	3790	38.4	1.01%
28	0.985	0.368	0.00421	1.15%	6000	55.3	0.92%
32	0.985	0.367	0.00533	1.46%	8927	67.2	0.75%
12	0.99	0.368	0.0121	3.28%	479	12.3	2.57%
16	0.99	0.365	0.0126	3.44%	1114	35.0	3.14%
20	0.99	0.361	0.00657	1.82%	2153	35.6	1.65%
24	0.99	0.363	0.00616	1.70%	3725	65.1	1.75%
28	0.99	0.364	0.00412	1.13%	5923	46.6	0.79%
32	0.99	0.362	0.00472	1.30%	8806	69.2	0.79%
12	0.995	0.350	0.0114	3.25%	455	14.2	3.11%
16	0.995	0.358	0.00858	2.40%	1088	23.5	2.16%
20	0.995	0.360	0.00778	2.16%	2120	20.0	0.94%
24	0.995	0.359	0.00757	2.11%	3655	38.0	1.04%
28	0.995	0.361	0.00531	1.47%	5831	30.0	0.51%
32	0.995	0.360	0.00358	0.99%	8730	50.8	0.58%

Table A.5: Void phase fraction and total particle count for type A systems as a function of system size, L/r

L/r	λ	Mean Void Phase Fraction	Standard Deviation	σ/μ	Mean Number of Particles	Standard Deviation	σ/μ
12	0.965	0.234	0.00608	2.60%	1017	4.74	0.466%
16	0.965	0.233	0.00549	2.36%	2398	5.40	0.225%
20	0.965	0.233	0.00358	1.54%	4679	8.94	0.191%
24	0.965	0.232	0.00477	2.05%	8061	9.64	0.120%
28	0.965	0.233	0.00347	1.49%	12782	23.2	0.181%
32	0.965	0.232	0.00462	1.99%	19062	12.3	0.0643%
12	0.97	0.241	0.00356	1.48%	1001	5.77	0.576%
16	0.97	0.242	0.00684	2.83%	2362	5.69	0.241%
20	0.97	0.239	0.00374	1.57%	4599	9.08	0.197%
24	0.97	0.242	0.00429	1.77%	7937	6.76	0.085%
28	0.97	0.242	0.00307	1.27%	12582	9.18	0.0729%
32	0.97	0.243	0.00364	1.50%	18750	18.9	0.101%
12	0.975	0.250	0.00345	1.38%	986	3.52	0.357%
16	0.975	0.248	0.00355	1.43%	2327	4.68	0.201%
20	0.975	0.249	0.00477	1.91%	4529	7.16	0.158%
24	0.975	0.249	0.00538	2.16%	7813	7.36	0.0943%
28	0.975	0.249	0.00239	0.96%	12380	12.4	0.100%
32	0.975	0.250	0.00364	1.46%	18459	16.5	0.0895%
12	0.98	0.259	0.00413	1.60%	971	2.49	0.257%
16	0.98	0.258	0.00452	1.75%	2288	5.22	0.228%
20	0.98	0.255	0.00341	1.33%	4459	8.59	0.193%
24	0.98	0.253	0.00522	2.06%	7686	5.32	0.0692%
28	0.98	0.257	0.00319	1.24%	12192	11.0	0.0902%
32	0.98	0.260	0.00319	1.23%	18179	15.8	0.087%

Table A.6: Void phase fraction and total particle count for type A systems as a function of system size, L/r (continued)

L/r	λ	Mean Void Phase Fraction	Standard Deviation	σ/μ	Mean Number of Particles	Standard Deviation	σ/μ
12	0.985	0.266	0.00556	2.09%	955	4.73	0.495%
16	0.985	0.264	0.00527	1.99%	2256	4.98	0.221%
20	0.985	0.265	0.00342	1.29%	4388	5.02	0.114%
24	0.985	0.263	0.00523	1.99%	7571	8.80	0.116%
28	0.985	0.268	0.00461	1.72%	12009	6.22	0.0518%
32	0.985	0.266	0.00560	2.11%	17898	18.0	0.100%
12	0.99	0.277	0.00190	0.69%	941	3.50	0.372%
16	0.99	0.275	0.00331	1.20%	2219	3.40	0.153%
20	0.99	0.274	0.00251	0.91%	4323	6.35	0.147%
24	0.99	0.275	0.00316	1.15%	7450	9.60	0.129%
28	0.99	0.273	0.00549	2.01%	11820	10.9	0.0925%
32	0.99	0.274	0.00289	1.05%	17629	19.5	0.111%
12	0.995	0.285	0.00679	2.38%	926	4.84	0.523%
16	0.995	0.282	0.00411	1.46%	2188	3.75	0.172%
20	0.995	0.281	0.00503	1.79%	4255	7.69	0.181%
24	0.995	0.282	0.00532	1.89%	7344	10.0	0.137%
28	0.995	0.283	0.00385	1.36%	11636	11.0	0.0944%
32	0.995	0.283	0.00236	0.834%	17363	12.4	0.0712%

Table A.7: Z and Z_{Ni} for type A systems as a function of system size, L/r

L/r	λ	Z	σ_Z	σ/μ	Z_{Ni}	$\sigma_{Z_{\mathrm{Ni}}}$	σ/μ
12	0.965	8.12	0.0724	0.89%	8.11	0.0571	0.70%
16	0.965	8.15	0.0391	0.48%	8.15	0.0466	0.57%
20	0.965	8.18	0.0232	0.28%	8.19	0.0215	0.26%
24	0.965	8.19	0.023	0.28%	8.17	0.0272	0.33%
28	0.965	8.2	0.0199	0.24%	8.2	0.0184	0.22%
32	0.965	8.21	0.0138	0.17%	8.21	0.0158	0.19%
12	0.97	8.01	0.0494	0.62%	8.03	0.0671	0.84%
16	0.97	8.05	0.0331	0.41%	8.05	0.0352	0.44%
20	0.97	8.08	0.0267	0.33%	8.08	0.0294	0.36%
24	0.97	8.09	0.0145	0.18%	8.1	0.0222	0.27%
28	0.97	8.11	0.0128	0.16%	8.11	0.0191	0.24%
32	0.97	8.11	0.014	0.17%	8.1	0.0123	0.15%
12	0.975	7.92	0.0542	0.68%	7.93	0.0716	0.90%
16	0.975	7.96	0.0262	0.33%	7.96	0.0399	0.50%
20	0.975	7.99	0.0225	0.28%	7.98	0.0221	0.28%
24	0.975	8	0.0199	0.25%	7.99	0.0267	0.33%
28	0.975	8	0.0198	0.25%	8	0.0233	0.29%
32	0.975	8.02	0.0114	0.14%	8.02	0.0138	0.17%
12	0.98	7.8	0.0585	0.75%	7.8	0.0575	0.74%
16	0.98	7.85	0.0381	0.49%	7.85	0.0328	0.42%
20	0.98	7.89	0.024	0.31%	7.88	0.0375	0.48%
24	0.98	7.89	0.0132	0.17%	7.9	0.0165	0.21%
28	0.98	7.91	0.0113	0.14%	7.91	0.0148	0.19%
32	0.98	7.91	0.0124	0.16%	7.91	0.0114	0.14%

Table A.8: Z and Z_{Ni} for type A systems as a function of system size, L/r (continued)

L/r	λ	Z	σ_Z	σ/μ	Z_{Ni}	$\sigma_{Z_{\mathrm{Ni}}}$	σ/μ
12	0.985	7.69	0.0375	0.49%	7.67	0.0356	0.46%
16	0.985	7.75	0.029	0.37%	7.75	0.0337	0.43%
20	0.985	7.78	0.0225	0.29%	7.78	0.0278	0.36%
24	0.985	7.8	0.0135	0.17%	7.8	0.0236	0.30%
28	0.985	7.82	0.0108	0.14%	7.81	0.014	0.18%
32	0.985	7.81	0.0163	0.21%	7.81	0.0192	0.25%
12	0.99	7.6	0.0334	0.44%	7.6	0.0414	0.55%
16	0.99	7.64	0.0312	0.41%	7.65	0.0308	0.40%
20	0.99	7.68	0.0198	0.26%	7.68	0.0256	0.33%
24	0.99	7.68	0.0179	0.23%	7.68	0.0217	0.28%
28	0.99	7.7	0.0194	0.25%	7.7	0.0217	0.28%
32	0.99	7.71	0.016	0.21%	7.71	0.0204	0.27%
12	0.995	7.49	0.0594	0.79%	7.47	0.0734	0.98%
16	0.995	7.54	0.0316	0.42%	7.53	0.0345	0.46%
20	0.995	7.56	0.0174	0.23%	7.55	0.0262	0.35%
24	0.995	7.58	0.024	0.32%	7.57	0.0293	0.39%
28	0.995	7.59	0.0147	0.19%	7.59	0.0179	0.24%
32	0.995	7.6	0.0101	0.13%	7.6	0.0146	0.19%

Table A.9: $Z_{\text{YSZ}-\text{YSZ}}$ and $Z_{\text{Ni}-\text{Ni}}$ for type A systems as a function of system size, L/r

L/r	λ	$Z_{\text{YSZ}-\text{YSZ}}$	$\sigma_{Z_{\text{YSZ}-\text{YSZ}}}$	σ/μ	$Z_{\text{Ni}-\text{Ni}}$	$\sigma_{Z_{\text{Ni}-\text{Ni}}}$	σ/μ
12	0.965	4.07	0.149	3.66%	4.04	0.121	3.00%
16	0.965	4.06	0.0962	2.37%	4.07	0.0707	1.74%
20	0.965	4.11	0.0766	1.86%	4.07	0.0576	1.42%
24	0.965	4.15	0.0645	1.55%	4.04	0.0768	1.90%
28	0.965	4.11	0.048	1.17%	4.1	0.0564	1.38%
32	0.965	4.1	0.027	0.66%	4.1	0.026	0.64%
12	0.97	4.01	0.0911	2.27%	4.01	0.127	3.17%
16	0.97	4.01	0.0638	1.59%	4.06	0.0958	2.36%
20	0.97	4.05	0.0753	1.86%	4.03	0.0715	1.78%
24	0.97	4.05	0.0575	1.42%	4.04	0.043	1.06%
28	0.97	4.06	0.0472	1.16%	4.05	0.033	0.82%
32	0.97	4.07	0.0409	1.01%	4.04	0.0283	0.70%
12	0.975	3.97	0.155	3.91%	3.97	0.0866	2.18%
16	0.975	4.05	0.0859	2.12%	3.97	0.0585	1.48%
20	0.975	3.98	0.0561	1.41%	3.98	0.0655	1.64%
24	0.975	4.01	0.0576	1.44%	3.98	0.061	1.54%
28	0.975	4.01	0.055	1.37%	3.99	0.0306	0.77%
32	0.975	4.02	0.0309	0.77%	4.01	0.0393	0.98%
12	0.98	3.87	0.142	3.66%	3.89	0.106	2.71%
16	0.98	3.93	0.0724	1.84%	3.88	0.0756	1.95%
20	0.98	3.96	0.0439	1.11%	3.95	0.078	1.97%
24	0.98	3.97	0.0493	1.24%	3.95	0.0654	1.66%
28	0.98	3.95	0.0238	0.60%	3.97	0.0297	0.75%
32	0.98	3.97	0.0226	0.57%	3.94	0.035	0.89%

Table A.10: $Z_{\text{YSZ}-\text{YSZ}}$ and $Z_{\text{Ni}-\text{Ni}}$ for type A systems as a function of system size, L/r (continued)

L/r	λ	$Z_{\text{YSZ}-\text{YSZ}}$	$\sigma_{Z_{\text{YSZ}-\text{YSZ}}}$	σ/μ	$Z_{\text{Ni}-\text{Ni}}$	$\sigma_{Z_{\text{Ni}-\text{Ni}}}$	σ/μ
12	0.985	3.83	0.158	4.11%	3.86	0.172	4.46%
16	0.985	3.87	0.119	3.07%	3.88	0.0977	2.52%
20	0.985	3.91	0.0464	1.18%	3.9	0.0487	1.25%
24	0.985	3.9	0.0364	0.93%	3.9	0.04	1.03%
28	0.985	3.92	0.0338	0.86%	3.91	0.043	1.10%
32	0.985	3.9	0.0325	0.83%	3.92	0.0286	0.73%
12	0.99	3.86	0.124	3.21%	3.72	0.146	3.92%
16	0.99	3.79	0.136	3.60%	3.78	0.128	3.38%
20	0.99	3.81	0.0556	1.46%	3.84	0.096	2.50%
24	0.99	3.83	0.0686	1.79%	3.83	0.0762	1.99%
28	0.99	3.85	0.0264	0.69%	3.84	0.0471	1.23%
32	0.99	3.86	0.0405	1.05%	3.86	0.0308	0.80%
12	0.995	3.69	0.11	2.99%	3.79	0.126	3.32%
16	0.995	3.74	0.109	2.92%	3.77	0.0677	1.80%
20	0.995	3.75	0.0501	1.33%	3.77	0.0426	1.13%
24	0.995	3.77	0.0488	1.30%	3.79	0.0248	0.66%
28	0.995	3.8	0.0308	0.81%	3.79	0.0278	0.73%
32	0.995	3.82	0.0394	1.03%	3.78	0.0276	0.73%

Table A.11: Conductivity for type A systems as a function of system size, L/r

L/r	λ	Reduced Conductivity of Ni Phase	σ	σ/μ	Reduced Conductivity of YSZ Phase	σ	σ/μ
12	0.965	0.0293	0.00472	16.1%	0.0323	0.00699	21.7%
16	0.965	0.0345	0.00335	9.70%	0.0324	0.00360	11.1%
20	0.965	0.0338	0.00173	5.12%	0.0357	0.00314	8.81%
24	0.965	0.0340	0.00286	8.41%	0.0374	0.00241	6.45%
28	0.965	0.0353	0.00215	6.08%	0.0357	0.00215	6.01%
32	0.965	0.0357	0.00116	3.25%	0.0360	0.00126	3.50%
12	0.97	0.0263	0.00826	31.3%	0.0294	0.00426	14.5%
16	0.97	0.0310	0.00320	10.3%	0.0299	0.00354	11.8%
20	0.97	0.0310	0.00291	9.39%	0.0327	0.00214	6.53%
24	0.97	0.0324	0.00150	4.65%	0.0319	0.00221	6.94%
28	0.97	0.0326	0.00098	3.01%	0.0335	0.00132	3.95%
32	0.97	0.0328	0.00081	2.47%	0.0335	0.00103	3.09%
12	0.975	0.0260	0.00430	16.5%	0.0281	0.00437	15.5%
16	0.975	0.0274	0.00328	12.0%	0.0291	0.00242	8.34%
20	0.975	0.0290	0.00233	8.03%	0.0286	0.00239	8.38%
24	0.975	0.0281	0.00199	7.08%	0.0295	0.00251	8.51%
28	0.975	0.0298	0.00115	3.85%	0.0303	0.00162	5.34%
32	0.975	0.0299	0.00104	3.48%	0.0307	0.00112	3.64%
12	0.98	0.0223	0.00383	17.1%	0.0248	0.00289	11.6%
16	0.98	0.0235	0.00313	13.3%	0.0264	0.00254	9.60%
20	0.98	0.0265	0.00119	4.49%	0.0267	0.00090	3.36%
24	0.98	0.0266	0.00224	8.42%	0.0269	0.00142	5.28%
28	0.98	0.0275	0.00131	4.76%	0.0262	0.00089	3.38%
32	0.98	0.0273	0.00071	2.61%	0.0275	0.00102	3.70%

Table A.12: Conductivity for type A systems as a function of system size, L/r (continued)

L/r	λ	Reduced Conductivity of Ni Phase	σ	σ/μ	Reduced Conductivity of YSZ Phase	σ	σ/μ
12	0.985	0.0228	0.00319	14.0%	0.0201	0.00393	19.5%
16	0.985	0.0233	0.00347	14.9%	0.0228	0.00307	13.4%
20	0.985	0.0236	0.00200	8.46%	0.0233	0.00178	7.61%
24	0.985	0.0246	0.00133	5.39%	0.0240	0.00138	5.74%
28	0.985	0.0250	0.00111	4.46%	0.0245	0.00097	3.96%
32	0.985	0.0249	0.00093	3.72%	0.0244	0.00111	4.54%
12	0.99	0.0181	0.00491	27.2%	0.0220	0.00334	15.1%
16	0.99	0.0202	0.00401	19.9%	0.0209	0.00373	17.8%
20	0.99	0.0216	0.00293	13.5%	0.0202	0.00212	10.5%
24	0.99	0.0212	0.00205	9.68%	0.0217	0.00156	7.19%
28	0.99	0.0215	0.00134	6.26%	0.0219	0.00112	5.11%
32	0.99	0.0218	0.00103	4.71%	0.0224	0.00116	5.18%
12	0.995	0.0184	0.00481	26.1%	0.0156	0.00282	18.1%
16	0.995	0.0188	0.00195	10.4%	0.0179	0.00194	10.8%
20	0.995	0.0187	0.00194	10.3%	0.0184	0.00122	6.65%
24	0.995	0.0190	0.00108	5.68%	0.0188	0.00093	4.91%
28	0.995	0.0191	0.00087	4.59%	0.0196	0.00114	5.82%
32	0.995	0.0188	0.00103	5.46%	0.0198	0.00089	4.48%

A.2   System with a Fixed Ratio Between Ni and YSZ Particles (Type B)

Table A.13: Ni phase fraction and particle count for type B systems as a function of system size, L/r

L/r	λ	Mean Nickel Phase Fraction	Standard Deviation	σ/μ	Mean Number of Nickel Particles	Standard Deviation	σ/μ
12	0.965	0.245	0.00737	1.88%	683	13.8	1.88%
16	0.965	0.246	0.00633	1.82%	1605	41.0	1.82%
20	0.965	0.246	0.00628	1.21%	3142	47.1	1.21%
24	0.965	0.244	0.00510	1.08%	5392	67.9	1.08%
28	0.965	0.245	0.00554	1.15%	8532	73.3	1.15%
32	0.965	0.245	0.00467	1.11%	12820	126	1.11%
12	0.97	0.246	0.0106	2.34%	683	19.6	2.34%
16	0.97	0.246	0.00624	1.47%	1594	44.1	1.47%
20	0.97	0.243	0.00799	1.62%	3087	57.0	1.62%
24	0.97	0.244	0.00643	0.950%	5340	76.7	0.95%
28	0.97	0.242	0.00354	0.930%	8455	70.1	0.93%
32	0.97	0.243	0.00452	0.820%	12574	88.6	0.82%
12	0.975	0.238	0.00725	1.77%	663	14.6	1.77%
16	0.975	0.240	0.00362	0.930%	1559	13.9	0.93%
20	0.975	0.242	0.00694	1.11%	3060	32.8	1.11%
24	0.975	0.240	0.00439	0.76%	5269	56.3	0.76%
28	0.975	0.240	0.00455	1.11%	8334	69.5	1.11%
32	0.975	0.239	0.00410	1.03%	12429	92.4	1.03%

Table A.14: Ni phase fraction and particle count for type B systems as a function of system size, L/r (continued)

L/r	λ	Mean Nickel Phase Fraction	Standard Deviation	σ/μ	Mean Number of Nickel Particles	Standard Deviation	σ/μ
12	0.98	0.247	0.00561	0.980%	672	9.73	0.98%
16	0.98	0.238	0.00560	1.39%	1541	25.7	1.39%
20	0.98	0.241	0.00319	1.02%	3017	39.5	1.02%
24	0.98	0.237	0.00577	1.57%	5186	55.2	1.57%
28	0.98	0.237	0.00406	1.13%	8205	69.7	1.13%
32	0.98	0.237	0.00518	1.12%	12288	77.8	1.12%
12	0.985	0.238	0.0101	1.77%	653	20.0	1.77%
16	0.985	0.237	0.00764	1.56%	1522	37.7	1.56%
20	0.985	0.237	0.00726	1.29%	2980	59.9	1.29%
24	0.985	0.236	0.00477	0.85%	5127	47.7	0.85%
28	0.985	0.233	0.00417	0.87%	8083	101.5	0.87%
32	0.985	0.237	0.00412	0.96%	12078	79.7	0.96%
12	0.99	0.235	0.0115	2.72%	643	31.7	2.72%
16	0.99	0.233	0.00528	1.07%	1487	19.8	1.07%
20	0.99	0.234	0.00737	1.68%	2915	74.7	1.68%
24	0.99	0.232	0.00493	1.46%	5037	53.5	1.46%
28	0.99	0.236	0.00472	0.990%	8021	78.7	0.99%
32	0.99	0.233	0.00558	1.84%	11992	105	1.84%
12	0.995	0.234	0.0116	3.24%	638	24.5	3.24%
16	0.995	0.231	0.00616	1.00%	1494	28.3	1.00%
20	0.995	0.231	0.00519	1.24%	2906	36.5	1.24%
24	0.995	0.232	0.00420	1.26%	5001	58.2	1.26%
28	0.995	0.232	0.00588	1.03%	7922	81.6	1.03%
32	0.995	0.232	0.00414	1.08%	11805	87.7	1.08%

Table A.15: YSZ phase fraction and particle count for type B systems as a function of system size, L/r

L/r	λ	Mean YSZ Phase Fraction	Standard Deviation	σ/μ	Mean Number of YSZ Particles	Standard Deviation	σ/μ
12	0.965	0.515	0.00966	1.88%	676	8.13	1.20%
16	0.965	0.517	0.00941	1.82%	1599	19.9	1.25%
20	0.965	0.514	0.00620	1.21%	3108	21.5	0.692%
24	0.965	0.518	0.00561	1.08%	5375	29.6	0.550%
28	0.965	0.517	0.00592	1.15%	8543	32.1	0.375%
32	0.965	0.517	0.00576	1.11%	12693	59.4	0.468%
12	0.97	0.506	0.01185	2.34%	663	10.3	1.55%
16	0.97	0.510	0.00749	1.47%	1575	22.4	1.43%
20	0.97	0.509	0.00825	1.62%	3077	30.8	1.00%
24	0.97	0.512	0.00486	0.95%	5295	34.9	0.659%
28	0.97	0.510	0.00473	0.93%	8408	31.0	0.369%
32	0.97	0.513	0.00422	0.82%	12564	40.7	0.324%
12	0.975	0.510	0.00903	1.77%	662	7.09	1.07%
16	0.975	0.506	0.00472	0.93%	1561	8.25	0.529%
20	0.975	0.505	0.00562	1.11%	3031	15.1	0.497%
24	0.975	0.509	0.00384	0.76%	5234	26.8	0.512%
28	0.975	0.506	0.00559	1.11%	8302	34.6	0.417%
32	0.975	0.509	0.00524	1.03%	12392	44.6	0.360%
12	0.98	0.495	0.00485	0.98%	644	4.55	0.706%
16	0.98	0.503	0.00699	1.39%	1541	11.9	0.770%
20	0.98	0.498	0.00510	1.02%	2991	16.5	0.553%
24	0.98	0.501	0.00787	1.57%	5172	25.5	0.493%
28	0.98	0.502	0.00565	1.13%	8214	42.5	0.517%
32	0.98	0.503	0.00563	1.12%	12210	31.3	0.256%

Table A.16: YSZ phase fraction and particle count for type B systems as a function of system size, L/r (continued)

L/r	λ	Mean YSZ Phase Fraction	Standard Deviation	σ/μ	Mean Number of YSZ Particles	Standard Deviation	σ/μ
12	0.985	0.496	0.00879	1.77%	640	9.49	1.48%
16	0.985	0.495	0.00770	1.56%	1517	17.1	1.13%
20	0.985	0.496	0.00638	1.29%	2955	31.5	1.07%
24	0.985	0.500	0.00423	0.85%	5103	21.0	0.412%
28	0.985	0.499	0.00433	0.87%	8107	48.9	0.604%
32	0.985	0.496	0.00478	0.96%	12088	46.0	0.380%
12	0.99	0.492	0.0134	2.72%	632	16.2	2.56%
16	0.99	0.495	0.00529	1.07%	1505	10.2	0.68%
20	0.99	0.491	0.00824	1.68%	2930	35.1	1.20%
24	0.99	0.496	0.00725	1.46%	5052	31.5	0.623%
28	0.99	0.490	0.00487	0.99%	7993	34.2	0.428%
32	0.99	0.493	0.00909	1.84%	11894	53.0	0.446%
12	0.995	0.482	0.0156	3.24%	623	11.2	1.79%
16	0.995	0.488	0.00488	1.00%	1479	15.8	1.07%
20	0.995	0.487	0.00604	1.24%	2881	19.9	0.691%
24	0.995	0.488	0.00617	1.26%	4971	28.3	0.568%
28	0.995	0.488	0.00501	1.03%	7883	39.3	0.499%
32	0.995	0.489	0.00530	1.08%	11767	41.4	0.352%

Table A.17: Void phase fraction and total particle count for type B systems as a function of system size, L/r

L/r	λ	Mean Void Phase Fraction	Standard Deviation	σ/μ	Mean Number of Particles	Standard Deviation	σ/μ
LoR	Overlap	Void Fraction			Num Particles		
12	0.965	0.240	0.00420	1.75%	1359	7.13	0.525%
16	0.965	0.237	0.00593	2.50%	3204	21.7	0.677%
20	0.965	0.241	0.00576	2.39%	6250	26.8	0.429%
24	0.965	0.237	0.00451	1.90%	10767	40.1	0.372%
28	0.965	0.239	0.00367	1.54%	17076	42.9	0.251%
32	0.965	0.238	0.00276	1.16%	25513	69.6	0.273%
12	0.97	0.248	0.00233	0.94%	1345	9.65	0.717%
16	0.97	0.245	0.00355	1.45%	3168	22.0	0.695%
20	0.97	0.248	0.00254	1.02%	6163	27.9	0.452%
24	0.97	0.244	0.00472	1.94%	10635	42.5	0.399%
28	0.97	0.247	0.00447	1.81%	16863	42.2	0.250%
32	0.97	0.244	0.00270	1.10%	25138	50.9	0.203%
12	0.975	0.252	0.00502	1.99%	1324	8.78	0.663%
16	0.975	0.253	0.00478	1.89%	3120	11.2	0.360%
20	0.975	0.254	0.00538	2.12%	6091	20.6	0.338%
24	0.975	0.252	0.00251	1.00%	10503	32.6	0.311%
28	0.975	0.254	0.00321	1.26%	16636	39.3	0.236%
32	0.975	0.252	0.00469	1.86%	24822	50.3	0.203%
12	0.98	0.259	0.00397	1.53%	1316	6.84	0.520%
16	0.98	0.259	0.00368	1.42%	3082	14.8	0.481%
20	0.98	0.261	0.00410	1.57%	6008	23.8	0.396%
24	0.98	0.261	0.00335	1.28%	10357	31.5	0.304%
28	0.98	0.262	0.00452	1.73%	16418	29.3	0.178%
32	0.98	0.259	0.00340	1.31%	24498	49.0	0.200%

Table A.18: Void phase fraction and total particle count for type B systems as a function of system size, L/r (continued)

L/r	λ	Mean Void Phase Fraction	Standard Deviation	σ/μ	Mean Number of Particles	Standard Deviation	σ/μ
LoR	Overlap	Void Fraction			Num Particles		
12	0.985	0.266	0.00652	2.45%	1293	12.3	0.953%
16	0.985	0.268	0.00386	1.44%	3039	21.2	0.697%
20	0.985	0.267	0.00443	1.66%	5935	30.8	0.519%
24	0.985	0.265	0.00339	1.28%	10229	28.7	0.281%
28	0.985	0.268	0.00411	1.53%	16190	53.5	0.330%
32	0.985	0.267	0.00505	1.89%	24166	37.4	0.155%
12	0.99	0.273	0.00420	1.54%	1275	16.0	1.26%
16	0.99	0.272	0.00388	1.42%	2992	11.8	0.393%
20	0.99	0.275	0.00541	1.96%	5845	40.0	0.685%
24	0.99	0.272	0.00494	1.81%	10089	24.1	0.239%
28	0.99	0.274	0.00300	1.09%	16014	47.0	0.294%
32	0.99	0.274	0.00560	2.04%	23886	55.2	0.231%
12	0.995	0.284	0.00799	2.81%	1260	13.9	1.10%
16	0.995	0.281	0.00368	1.31%	2973	17.6	0.591%
20	0.995	0.282	0.00506	1.79%	5787	18.7	0.323%
24	0.995	0.281	0.00500	1.78%	9972	31.5	0.316%
28	0.995	0.280	0.00387	1.38%	15805	46.0	0.291%
32	0.995	0.280	0.00557	1.99%	23571	50.1	0.212%

Table A.19: Z, $Z_{\text{YSZ}-\text{YSZ}}$, and $Z_{\text{Ni}-\text{Ni}}$ for type B systems as a function of system size, L/r

L/r	λ	Z	σ_Z	σ/μ	$Z_{\text{YSZ}-\text{YSZ}}$	$\sigma_{Z_{\text{YSZ}-\text{YSZ}}}$	σ/μ	$Z_{\text{Ni}-\text{Ni}}$	$\sigma_{Z_{\text{Ni}-\text{Ni}}}$	σ/μ
12	0.965	7.97	0.0617	0.77%	5.12	0.0916	1.79%	3.04	0.0679	2.23%
16	0.965	8.02	0.018	0.23%	5.18	0.0847	1.63%	3.1	0.0585	1.89%
20	0.965	8.05	0.0134	0.17%	5.18	0.0529	1.02%	3.11	0.0597	1.92%
24	0.965	8.06	0.0165	0.21%	5.21	0.0385	0.74%	3.09	0.0429	1.39%
28	0.965	8.08	0.0102	0.13%	5.23	0.029	0.56%	3.09	0.0267	0.86%
32	0.965	8.08	0.0154	0.19%	5.22	0.0261	0.50%	3.12	0.036	1.15%
12	0.97	7.89	0.0368	0.47%	5.06	0.0955	1.89%	3.13	0.0725	2.32%
16	0.97	7.94	0.0246	0.31%	5.13	0.0742	1.45%	3.07	0.1137	3.71%
20	0.97	7.97	0.0242	0.30%	5.13	0.0536	1.04%	3.04	0.0549	1.81%
24	0.97	7.98	0.0134	0.17%	5.13	0.0222	0.43%	3.08	0.0576	1.87%
28	0.97	7.99	0.0151	0.19%	5.16	0.0213	0.41%	3.08	0.0302	0.98%
32	0.97	8.01	0.0062	0.08%	5.17	0.0216	0.42%	3.06	0.0214	0.70%
12	0.975	7.82	0.0475	0.61%	5.04	0.0866	1.72%	2.99	0.0679	2.27%
16	0.975	7.87	0.0353	0.45%	5.05	0.0551	1.09%	3.01	0.0657	2.18%
20	0.975	7.89	0.025	0.32%	5.06	0.0454	0.90%	3.01	0.0572	1.90%
24	0.975	7.91	0.0213	0.27%	5.09	0.0282	0.55%	3.04	0.035	1.15%
28	0.975	7.91	0.0157	0.20%	5.09	0.0301	0.59%	3.03	0.0226	0.75%
32	0.975	7.92	0.0072	0.09%	5.1	0.0277	0.54%	3.03	0.0208	0.69%
12	0.98	7.75	0.0453	0.59%	4.9	0.0735	1.50%	3.01	0.0827	2.75%
16	0.98	7.8	0.0283	0.36%	5.02	0.0537	1.07%	2.96	0.0629	2.12%
20	0.98	7.81	0.0188	0.24%	5	0.0383	0.77%	2.98	0.0486	1.63%
24	0.98	7.82	0.0139	0.18%	5.02	0.0252	0.50%	2.99	0.0496	1.66%
28	0.98	7.84	0.0146	0.19%	5.04	0.0291	0.58%	2.98	0.0353	1.18%
32	0.98	7.83	0.0111	0.14%	5.03	0.0137	0.27%	3	0.0187	0.62%

Table A.20: Z, $Z_{\text{YSZ}-\text{YSZ}}$, and $Z_{\text{Ni}-\text{Ni}}$ for type B systems as a function of system size, L/r (continued)

L/r	λ	Z	σ_Z	σ/μ	$Z_{\text{YSZ}-\text{YSZ}}$	$\sigma_{Z_{\text{YSZ}-\text{YSZ}}}$	σ/μ	$Z_{\text{Ni}-\text{Ni}}$	$\sigma_{Z_{\text{Ni}-\text{Ni}}}$	σ/μ
12	0.985	7.65	0.0483	0.63%	4.85	0.0825	1.70%	2.91	0.0858	2.95%
16	0.985	7.69	0.0354	0.46%	4.92	0.0598	1.21%	2.93	0.0883	3.01%
20	0.985	7.73	0.0243	0.31%	4.95	0.0507	1.02%	2.96	0.0739	2.50%
24	0.985	7.74	0.0124	0.16%	4.94	0.0415	0.84%	2.93	0.0258	0.88%
28	0.985	7.74	0.0096	0.12%	4.97	0.0309	0.62%	2.94	0.0396	1.35%
32	0.985	7.75	0.0095	0.12%	4.97	0.0153	0.31%	2.94	0.03	1.02%
12	0.99	7.59	0.0584	0.77%	4.81	0.158	3.28%	2.92	0.133	4.56%
16	0.99	7.61	0.0205	0.27%	4.89	0.0596	1.22%	2.85	0.0503	1.77%
20	0.99	7.64	0.0116	0.15%	4.88	0.0656	1.34%	2.86	0.0884	3.09%
24	0.99	7.66	0.0185	0.24%	4.89	0.0519	1.06%	2.88	0.0309	1.07%
28	0.99	7.66	0.0146	0.19%	4.88	0.0246	0.51%	2.9	0.0256	0.88%
32	0.99	7.66	0.0133	0.17%	4.88	0.0256	0.53%	2.92	0.0258	0.88%
12	0.995	7.48	0.0331	0.44%	4.71	0.115	2.43%	2.83	0.0959	3.38%
16	0.995	7.53	0.0337	0.45%	4.8	0.0845	1.76%	2.87	0.0687	2.39%
20	0.995	7.55	0.0237	0.31%	4.78	0.0401	0.84%	2.87	0.0489	1.71%
24	0.995	7.56	0.0097	0.13%	4.81	0.0405	0.84%	2.87	0.0307	1.07%
28	0.995	7.56	0.0103	0.14%	4.81	0.0281	0.58%	2.88	0.0324	1.12%
32	0.995	7.57	0.0088	0.12%	4.81	0.0209	0.44%	2.86	0.0235	0.82%

Table A.21: Conductivity for type B systems as a function of system size, L/r

L/r	λ	Reduced Conductivity of Ni Phase	σ	σ/μ	Reduced Conductivity of YSZ Phase	σ	σ/μ
12	0.965	0.00130	0.000446	34.2%	0.0110	0.001376	12.5%
16	0.965	0.000945	0.000375	39.6%	0.0109	0.000737	6.74%
20	0.965	0.00110	0.000293	26.7%	0.0106	0.000631	5.96%
24	0.965	0.000869	0.000176	20.3%	0.0103	0.000395	3.85%
28	0.965	0.000902	0.000117	13.0%	0.00989	0.000339	3.43%
32	0.965	0.000925	0.0000956	10.3%	0.00997	0.000159	1.59%
36	0.965	0.000861	0.0000873	10.1%	0.00993	0.000180	1.81%
40	0.965	0.000822	0.0000823	10.0%	0.00993	0.000166	1.67%
12	0.97	0.000981	0.000556	56.7%	0.00976	0.001154	11.8%
16	0.97	0.000827	0.000262	31.7%	0.00998	0.000783	7.85%
20	0.97	0.00109	0.000207	18.9%	0.00935	0.000561	6.00%
24	0.97	0.000866	0.000167	19.2%	0.00931	0.000371	3.99%
28	0.97	0.000822	0.000116	14.1%	0.00925	0.000316	3.41%
32	0.97	0.000770	0.000126	16.3%	0.00918	0.000155	1.69%
36	0.97	0.000735	0.0000570	7.75%	0.00929	0.000166	1.79%
40	0.97	0.000782	0.0000662	8.47%	0.00911	0.000200	2.20%
12	0.975	0.00110	0.000448	40.7%	0.00951	0.001290	13.6%
16	0.975	0.000935	0.000184	19.7%	0.00912	0.000561	6.15%
20	0.975	0.000773	0.000227	29.4%	0.00908	0.000390	4.30%
24	0.975	0.000677	0.000096	14.2%	0.00868	0.000323	3.72%
28	0.975	0.000680	0.000139	20.5%	0.00865	0.000289	3.34%
32	0.975	0.000729	0.000113	15.5%	0.00852	0.000249	2.92%
36	0.975	0.000708	0.0000727	10.3%	0.00843	0.000208	2.47%
40	0.975	0.000641	0.0000599	9.34%	0.00830	0.000151	1.82%
12	0.98	0.000658	0.000335	51.0%	0.00819	0.000539	6.58%
16	0.98	0.000841	0.000266	31.7%	0.00796	0.000616	7.73%
20	0.98	0.000768	0.000129	16.7%	0.00793	0.000529	6.68%
24	0.98	0.000638	0.000148	23.1%	0.00808	0.000426	5.27%
28	0.98	0.000645	0.000141	21.9%	0.00788	0.000470	5.97%
32	0.98	0.000630	0.000103	16.4%	0.00773	0.000230	2.98%
36	0.98	0.000600	0.0000803	13.4%	0.00770	0.000181	2.35%
40	0.98	0.000625	0.0000779	12.5%	0.00762	0.000124	1.63%

Table A.22: Conductivity for type B systems as a function of system size, L/r (continued)

L/r	λ	Reduced Conductivity of Ni Phase	σ	σ/μ	Reduced Conductivity of YSZ Phase	σ	σ/μ
12	0.985	0.000592	0.000434	73.3%	0.00841	0.000536	6.37%
16	0.985	0.000775	0.000258	33.3%	0.00754	0.000645	8.55%
20	0.985	0.000667	0.000181	27.1%	0.00730	0.000450	6.16%
24	0.985	0.000651	0.000200	30.7%	0.00716	0.000469	6.54%
28	0.985	0.000541	0.000083	15.4%	0.00702	0.000224	3.20%
32	0.985	0.000558	0.000121	21.7%	0.00706	0.000222	3.15%
36	0.985	0.000547	0.0000449	8.20%	0.00707	0.000158	2.23%
40	0.985	0.000513	0.0000596	11.6%	0.00690	0.000093	1.35%
12	0.99	0.000884	0.000470	53.1%	0.00732	0.001347	18.4%
16	0.99	0.000741	0.000339	45.7%	0.00661	0.000925	14.0%
20	0.99	0.000595	0.000199	33.5%	0.00636	0.000370	5.82%
24	0.99	0.000537	0.000135	25.2%	0.00645	0.000145	2.24%
28	0.99	0.000472	0.0000749	15.9%	0.00653	0.000256	3.92%
32	0.99	0.000478	0.0000515	10.8%	0.00632	0.000229	3.62%
36	0.99	0.000454	0.0000832	18.3%	0.00636	0.000166	2.60%
40	0.99	0.000475	0.0000602	12.7%	0.00622	0.000159	2.56%
12	0.995	0.000551	0.000234	42.4%	0.00694	0.000863	12.4%
16	0.995	0.000528	0.000148	28.0%	0.00602	0.000655	10.9%
20	0.995	0.000520	0.000133	25.6%	0.00588	0.000236	4.02%
24	0.995	0.000472	0.000163	34.5%	0.00570	0.000438	7.69%
28	0.995	0.000428	0.0000527	12.3%	0.00576	0.000227	3.93%
32	0.995	0.000444	0.0000693	15.6%	0.00560	0.000164	2.93%
36	0.995	0.000394	0.0000629	16.0%	0.00562	0.000178	3.18%
40	0.995	0.000420	0.0000586	13.9%	0.00553	0.000151	2.73%

Bibliography

[1] J. Abel, A. A. Kornyshev, and W. Lehnert. Correlated resistor network study of porous fuel cell anodes. *Journal of the Electrochemical Society*, 144:4253, 1997. 8, 152

[2] A. J. Appleby and F. R. Foulkes. *Fuel Cell Handbook*. Krieger Publishing Company, Malabar, Florida, second edition, 1993. 2

[3] C. Argento and D. Bouvard. Modeling the effective thermal conductivity of random packing of spheres through densification. *International Journal of Heat and Mass Transfer*, 39:1343–1350, May 1996. 42

[4] A. J. Bard and L. R. Faulkner. *Electrochemical Methods: Fundamentals and Applications*. John Wiley and Sons, New York, New York, second edition, 2001. 141

[5] Jacob Bear. *Dynamics of Fluids in Prous media*. American Elsevier, New York, New York, 1972. 146

[6] C. H. Bennett. Serially deposited amorphous aggregates of hard spheres. *Journal of Applied Physics*, 43:2727–2741, 1972. 13, 27

[7] A. Bieberle and L. J. Glaucker. Reaction mechanism of Ni pattern anodes for solid oxide fuel cells. *Solid State Ionics*, 135:337–345, 2000. 142

[8] D. Bouvard and F. F. Lange. Relations between percolation and particle coordination in the binary powder mixtures. *Acta Metallurgy and Materials*, 49:3083–3090, 1991. 13, 87

[9] P. N. Brown, G. D. Byrne, and A. C. Hindmarsh. Vode, a variable-coefficient ode solver. *The SIAM Journal on Scientific and Statistical Computing*, 10:1038–1051, 1989. 51

[10] S. H. Chan, X. J. Chen, and K. A. Khor. Cathode micromodel of solid oxide fuel cell. *Journal of the Electrochemical Society*, 151:A164–A172, 2004. 15

[11] H. J. Cho and G. M. Choi. Effect of milling methods on performance of Ni-Y_2O_3-stabilized ZrO_2 anode for solid oxide fuel cell. *Journal of Power Sources*, 185:961–966, 2008. v, vii, viii, 32, 33, 97, 98, 99, 100, 101, 102, 103

[12] D. B. Chrisey and G. K. Hubler, editors. *Pulsed Laser Deposition of Thin Films*. John Wiley and Sons, New York, New York, second edition, 1994. 110

[13] P. Costamanga, P. Costa, and V. Antonucci. Micro-modelling of solid oxide fuel cell electrodes. *Electrochimica Acta*, 43:375–394, 1997. 14

[14] D. W. Dees, T. D. Claar, T. E. Easier, D. C. Fee, and F. C. Vlrazek. Conductivity of porous Ni/ZrO_2-Y_2O_3 cermets. *Journal of the Electrochemical Society*, 134:2141–2146, 1987. v, vii, 12, 15, 89, 90

[15] J. L. Devore. *Probability and Statistics for Engineering and the Sciences*. Brooks/Cole, Boston, Massachusetts, eighth edition, 2009. 55, 79

[16] G. Dotelli, I. Natali Sora, C. Schmid, and C. M. Mari. Composite materials as electrolytes for solid oxide fuel cells: simulation of microstructure and electrical properties. *Solid State Ionics*, 152/153:509–515, 2002. 14

[17] S. Feng, B. I. Halperin, and P. N. Sen. Transport properties of continuum systems near the percolation threshold. *Physics Review B*, 35:197, 1987. 42

[18] J. P. Fitzpatrick, R. B. Malt, and F. Spaepen. Percolation theory and the conductivity of random close packed mixtures of hard spheres. *Physics Letters*, 47A:207–8, 1974. 85

[19] J. Greenwood. The correct and incorrect generation of a cosine distribution of scattered particles for Monte-Carlo modelling of vacuum systems. *Vacuum*, 67:217–222, 2002. 49

[20] G. Grimmet. *Percolation.* Spring Publishing, New York, New York, 1999. v, 12, 16, 17

[21] W. R. Grove. On voltaic series and the combination of gases by platinum. *Philosophical Magazine and Journal of Science*, 14:127–130, 1839. 2

[22] J. M. Hammersley. Percolation processes: Lower bounds for the critical probability. *Annals of Mathematical Statistics*, 1957. 16

[23] J. Hanna. *Solid-Oxide Fuel Cell Electrode Microstructures: Making Sense of the Internal Framework Affecting Gas Transport.* Ph. D. dissertation, California Institute of Technology, 2010. 10, 47, 103, 146, 155

[24] Y. Hao and D. G. Goodwin. Numerical modeling of single-chamber SOFCs with hydrocarbon fuels. *Journal of the Electrochemical Society*, 154:B207–B217, 2007. 8, 10, 139, 152, 154

[25] W. K. Hastings. Monte Carlo sampling methods using Markov chains and their applications. *Biometrika*, 57:97–109, 1970. 33

[26] R. L. Hirsch. The inevitable peaking of world oil production. *Bulletin of the Atlantic Council of the United States*, 16:1–10, October 2005. 1

[27] M. K. Hubbert. *Nuclear Energy and Fossil Fuels.* Presented before the Spring Meeting of the Southern District, American Petroleum Institute, Plaza Hotel, San Antonio, Texas, March 1956. 1

[28] W. Huebner, H. U. Anderson, D. M. Reed, S. R. Sehlin, and X. Deng. Microstructure↔property relationships of Ni:ZrO$_2$ anodes. *Electrochemical Society SOFC-V Conference Proceedings*, 35:159–166, 1995. vii, 89, 91, 92, 116

[29] W. Kautek, B. Roas, and L. Schultz. Formation of Y-Ba-Cu-Oxide thin-films by Pulsed Laser Deposition—a Comparative Study in the UV, Visible and IR Range. *Thin Solid Films*, 191:317–334, 1990. 113

[30] T. Kawashima and M. Hishinuma. Analysis of electrical conduction paths in Ni/YSZ particulate composites using percolation theory. *Materials Transactions, JIM*, 37:1397–1403, 1996. v, 15

[31] C. M. Mari and G. Dotelli. A random resistor model to forecast the electrical properties of crystalline ionic conductor composites. *Solid State Ionics*, 136/137:1315–1319, 2000. 14

[32] C. M. Mari and G. Dotelli. How to forcast the electrical behaviour of ionic conductor composites? *Journal of Materials Science*, 36:1141–1147, 2001. 14

[33] C. L. Martin, D. Bouvard, and S. Shima. Study of particle rearrangement during powder compaction by the discrete element method. *Journal of the Mechanics and Physics of Solids*, 51:667–693, 2002. 15

[34] C. L. Martin, L. C. R. Schneider, L. Olmos, and D. Bouvard. Discrete element modeling of metallic powder sintering. *Scripta Materialia*, 55:425–428, 2006. 15, 109

[35] E. A. Mason and A. P. Malinauskas. *Gas Transport in Porous Media: the Dusty-Gas Model*. American Elsevier, New York, New York, 1983. 155

[36] N. Metropolis, A. W. Rosenbluth, M. N. Rosenbluth, A. H. Teller, and E. Teller. Equations of state calculations by fast computing machines. *Journal of Chemical Physics*, 21:1087–1092, 1953. 33

[37] L. Oger, J. P. Troadec, and D. Bideau. Properties of disordered sphere packings: I. geometric structure: Statistical model, numerical simulations and experimental results. *Powder Technology*, 46:121–131, 1986. 13, 85

[38] M. J. Powell. Site percolation in randomly packed spheres. *Physics Review B*, 20:4194–4198, 1979. 85

[39] W. H. Press, S. A. Teukolsky, W. T. Vetterling, and B. P. Flannery. *Numerical Recipes in C++*. Cambridge University Press, New York, New York, second edition, 2002. 37

[40] S. M. Ross. *Introduction to Modern Statistical Mechanics*. Academic Press (An Imprint of Elsevier Press), San Diego, California, eighth edition, 2003. 79

[41] J. Sandal. Finite element model of current flow in a random particle ensemble using ANSYS. Results Communicated to Vaughan Thomas in the Mechanical Engineering Division of the California Institute of Technology, September 2007. vi, 43, 44, 45

[42] L. C. R. Schneider, C. L. Martin, Y. Bultel, D. Bouvard, and E. Siebert. Discrete modelling of the electrochemical performance of SOFC electrodes. *Electrochimica Acta*, 52:314–324, 2006. 8, 15, 42, 94, 141, 152

[43] L. C. R. Schneider, C. L. Martin, Y. Bultel, L. Dessemond, and D. Bouvard. Percolation effects in functionally graded SOFC electrodes. *Electrochimica Acta*,

52:3190–3198, 2006. 8, 15, 109, 152

[44] H. M. Smith and A. F. Turner. Vacuum deposited thin films using a ruby laser. *Applied Optics*, 4:147–148, 1965. 110

[45] S. Sunde. Calculation of conductivity and polarization resistance of composite SOFC electrodes from random resistor networks. *Journal of the Electrochemical Society*, 142:L50–L52, 1995. 13

[46] S. Sunde. Monte Carlo simulations of conductivity of composite electrodes for solid oxide fuel cell. *Journal of the Electrochemical Society*, 143:1123–1132, 1996. v, vii, 13, 14, 91, 93

[47] S. Sunde. Monte Carlo simulations of polarization resistance of composite electrodes for solid oxide fuel cell. *Journal of the Electrochemical Society*, 143:1930–1939, 1996. 8, 13, 18, 141, 152

[48] S. Sunde. Simulations of composite electrodes in fuel cells. *Journal of Electroceramics*, 5:153–182, 1999. 8, 13, 91, 141, 152

[49] M. Suzuki and T. Oshima. Estimation of the co-ordination number in a three-component random mixture of spheres. *Powder Technology*, 35:159–166, 1982. 13

[50] M. Suzuki and T. Oshima. Comparison between the computer-simulated results and the model for estimating the co-ordination number in a three-component random mixture of spheres. *Powder Technology*, 43:19–25, 1985. 13, 16

[51] J. R. Wilson, W. Kobsiriphat, R. Mendoza, H. Chen, J. M. Hiller, D. J. Miller, K. Thornton, P. W. Voorhees, S. B. Adler, and S. A. Barnett. Three-dimensional reconstruction of a solid-oxide fuel-cell anode. *Nature: Materials*, 5:541–544, 2006. 24, 102, 117, 126, 154

[52] R. Zallen. *The Physics of Amorphous Solids.* John Wiley and Sons, New York, New York, Wiley Classics Library edition, 1983. 85

[53] H. Zhu, R. J. Kee, V. M. Janardhanan, O. Deutschmann, and D. G. Goodwin. Modeling elementary heterogeneous chemistry and electrochemistry in solid-oxide fuel cells. *Journal of the Electrochemical Society*, 152:2427–2440, 2005. 8, 139, 143, 144, 152, 154, 155